Flow fields of air-liquid droplet two-phase mixture and collision dynamics of a droplet on a surface

Hitoshi Fujimoto

1995

Contents

Chapter 1

Introduction

There are many industrial situations in which a fine liquid spray contacts and cools a surface which is at a temperature in excess of the liquid saturation temperature. This process is commonly called the spray or mist cooling. In iron- and steel-making industries, the spray cooling method is applied to the secondary cooling zone in a continuous casting process. Also, hot strips passing through the last finishing roll are cooled on a runout table from the austenitic finishing temperature to the coiling temperature. In this case, the upper surface of the strip is cooled by the laminar flow cooling method, while the lower surface is cooled by the water spray. Therefore, many studies on the mist or spray cooling were performed mainly from an experimental point of view [1]~ [9]. In these studies, effects of flow properties such as water mass flow density, droplet size, impinging velocity of droplet and etc. on heat transfer between a hot metal surface above Leidenfrost temperature and mist/spray jet were investigated in order to understand systematically cooling phenomena. However, the useful predictable model of the heat transfer in mist/spray cooling has not been constructed yet, because there are many parameters affecting cooling heat transfer and the effects of these parameters are very complicated. It seems to be necessary, first, to clarify the mist/spray flow structure from a hydrodynamical point of view. Without knowledge concerning the flow structure of the gas-water droplet two-phase jet in actual cooling systems as well as the deformation process of individual water droplets impinging on a hot solid surface above the Leidenfrost temperature, it is impossible to discuss the interaction effect of flow parameters on the cooling intensity. However, there seems to be a conspicuous lack of information about the mist/spray flow field. From this standpoint, the author started this study concerning the flow field of gas-particle two-phase mixtures as well as the deformation process of a water droplet impinging on a surface from numerical and experimental points of view.

Here, the author has attempted to construct mathematical models to analyse the gas-water droplet two-phase mixture flow. First, the flow fields of gas-water droplet mixtures in a nozzle are treated as a steady quasi-one dimensional system. The numerical approach of quasi-one-dimensional two-phase flow in a nozzle was performed by some researchers [10]- [12] who studied the flow of a gas containing suspended condensed metal oxide particles such as Al_2O_3 in the propulsive nozzle of a rocket motor. This approach needs not to consider the two/three dimensional complicated phenomena such as the

collision of particles with the nozzle wall. Kliegel [10] studied the variations of the particle velocity along the nozzle axis on the assumption that the ratio of the particle velocity to the gas velocity is constant in a nozzle. Rudinger [11] investigated the flow field for high loading ratio, defined as the mass flow rate ratio of the particle-phase to the gas-phase and estimated numerically the influence of various parameters on the flow structure. Gokhale and Bose [12] included the chemical reaction effect into a numerical model and studied the unsteady solid-particle mixture flow in a convergent-divergent nozzle. Zucrow and Hoffman [13] described the system of equations governing the one-dimensional gas-particle mixture flow in a nozzle. These above-mentioned models are limited to the case where all particles are single size.

In the actual flow of gas-particle mixture in a nozzle applied to the mist cooling, particle size is not single. Rather, it is far more common to consider that the liquid particles have a continuous distribution of size. Then, the author extends the governing equations described by Zucrow and Hoffman to give an applicability to the case where particles have a continuous distribution of size and gas-water droplet flow field in a nozzle is numerically analysed using modified model on the various conditions [14]~ [18].

Next, the flow field of the gas-droplets two-phase free jets and the flow structures of the two-phase jet impinging on a flat plate normal to the flow, corresponding to the collision of the mist/spray flows with a hot metal surface, are analysed numerically as a perturbation from the numerical results of nozzle flow [19]~ [23]. Also, two-phase free jets are investigated from an experimental viewpoint.

The flow fields in a free jet region were studied extensively by many researchers because of the importance from an industrial point of view. Experimental studies on gas-particle two-phase free jet were performed vigorously through the development of LDA(laser doppler anemometer) system [24]- [30]. Also, through the development of computer system, the numerical analyses of gas-only flow [31]- [37] were studied in a free jet region. However, for the case of the gas-particle two-phase mixtures, there are too many particles in the flow field to pursue individual particle trajectories, even by using the supercomputer from the viewpoints of CPU time and memory. In order to avoid this difficulty, some mathematical models which can numerically analyse the two-phase flow, were proposed [38]- [48]. These models can be basically divided in three types, that is, the two fluid model, the particle trajectory method and the Monte Carlo approach. Using these mathematical models, various gas-particle flows were analysed, such as the supersonic two-phase flow [48]~ [53], the combustible two-phase flow [54, 55], the behavior of fine particles in clean room [56], the two-phase flow induced by an explosion of high-pressure dusty gas in underground space [57].

In the present numerical model, thermal coupling through heat transfer from gas-phase to droplet-phase, as well as momentum coupling through aerodynamic drag responsible for droplet motion, is taken into account. The axisymmetric Navier-Stokes equations for a gas-phase interacting with particle-phase are solved by the discrete particle cloud model proposed by Ishii et al. [48].

To evaluate heat transfer between a heated surface and spray/mist consisting of water droplets and air, it is indispensable to understand the collision dynamics of liquid droplets on a hot rigid surface systematically as mentioned above. The deformation process of impacting droplet on a hot surface above the Leidenfrost temperature were investigated experimentally by many researchers [58]- [74]. From these studies, it was found that the droplet rebounds from the surface for small Weber numbers, while the droplet shatters on the surface for large Weber numbers [58, 61, 66]. Also, experimental formulae predicting the maximum spreading diameter of the drop on the surface were proposed in the form of the function of the Weber number only [61, 65]. Many experimental studies placed emphasis not upon the collision dynamics, but upon the heat transfer between the droplet and the surface. Therefore, the detailed deformation mechanism of the droplet impinging on the surface has not yet analysed. Also, it is impossible to experimentally measure the inner flow field of a droplet during and subsequent to the collision with a surface. Additionally, there seems to be no numerical analysis of the deformation and rebounding processes of droplet impinging against the hot surface. Some numerical studies were analysed the spreading process of the droplet impinging on a surface at room temperature [75]- [77].

Therefore, first, the time history of droplet deformation and rebounding processes is observed experimentally [78]. Next, the numerical simulations of the deformation behavior of a liquid droplet impinging on a flat solid surface at room temperature, as well as the flow field inside the droplet are performed for the first approach to the more realistic situation of industrial interest where the droplet impinges on a hot surface [79]. Finally, the deformation and rebounding processes of a water droplet impinging on a flat solid surface above the Leidenfrost temperature as well as the flow field inside the droplet are investigated from numerical and experimental points of view [80].

The present studies are composed of eight chapters.

In chapter 2, the gas-particle two-phase flows in a nozzle are analysed from a numerical point of view. For the subsonic nozzle flow, all of the flow properties calculate on the basis of a given nozzle geometry with a parallel region. Next, for the supersonic nozzle flow, the so-called specified pressure method is applied to the evaluation of flow properties of the gas-particle mixture in the flow field, as well as to the design of the converging-diverging nozzle configuration according to a given pressure profile. The effect of the ratio of the particle mass flow rate to the gas mass flow rate on the flow field are investigated numerically.

In chapter 3, the numerical simulation of the dilute gas-particle free jet exhausted from a round nozzle is performed. The jet flow structures of mixture composed of air and water-droplets with $1\mu m$, $5\mu m$ and $30\mu m$ in diameter, respectively, are calculated for the case where all the particles have a single size. Some of significant characteristics for the two-phase subsonic free jets are pointed out, in particular, focusing upon the effect of particle size on the flow structure. Also, the numerical results are compared with the experimental and discussed from the point of view of the validity of the present numerical model.

In chapter 4, the gas-droplet two-phase mixture jets impinging on a solid surface are investigated numerically on the assumption that the particles are perfectly elastically reflected from a surface. This is because the coefficient of restitution between the droplet

and the solid plate remains unclarified. Next, the case is analysed where a low velocity annular gas-only flow surrounding a round nozzle co-axially is present so that rebounded particles from the plate may be pushed back to the surface again. This is considered to result in an improvement of the mist cooling efficiency.

In chapter 5, the collision dynamics of a water droplet impinging on a hot surface are studied from an experimental point of view. Emphasis is placed upon the collision of relatively small droplets in the range from 300 μm to 600 μm with the surface. The surface temperature is fixed at 500 °C. The first purpose is to examine whether or not the prior empirical rules obtained by using droplets of 1 mm to 3 mm give an applicability to the case where the droplet size is much smaller. The second is to clarify the relation between the Weber number and the coefficient of restitution, when the droplet rebounds from the hot surface without disintegrating into a number of particles.

In chapter 6, the deformation process of a droplet impinging on a solid surface at room temperature is discussed. The simulations are performed using the MAC-type solution method [81, 82] to solve a finite-differencing approximation of the Navier-Stokes equations governing an axisymmetric and incompressible fluid flow and the numerical model is built up by considering the effect of viscous stresses and surface tension. The spreading and recoiling processes of droplet on the surface are investigated from numerical as well as experimental points of view. The numerical results are compared with the experimental ones for the validity of the present mathematical model. Also, the effects of the viscous stresses and the surface tension on the deformation process of the droplets, are estimated and discussed from a practical standpoint.

In chapter 7, the deformation and rebounding processes of a droplet impinging on a hot surface above the Leidenfrost temperature are numerically analysed. At the same time, the whole dynamic process of a droplet from the moment of collision with a hot surface up to the rebounding from it is observed by using a video camera equipped with a macro lens. The numerical results obtained by the model are compared with the experimental data and discussed from a practical point of view.

Chapter 8 is concluding remarks of this study.

Reference

[1] Muller, H. and Jeschar, R., Arch. Eisenhüttenwes, 44(1973), p.589.

[2] Hoogendoorn, C. J. and den Hond, R., Proc. 5th Int. Heat Transfer Conf., B3.12, 4(1974), p.135.

[3] Grissom, W. M. and Wierum. F. A., Int. J. Heat Mass Transfer, 24(1981), p.261.

[4] Mitsutsuka, M. and Fukuda, K., Tetsu-to-Hagane, 65(1979), p.608.

[5] Mitsutsuka, M. and Fukuda, K., Tetsu-to-Hagane, 69(1983), p.262.

[6] Köhler, C., Jeschar, R. Scholz, R. Slowik, J. and Borcardt, G., Steel Research, 61-7(1990), p.295.

[7] Slowik, J., Borcardt, G., Köhler, C., Scholz, R., Jeschar, R. and , Steel Research, 61-7(1990), p.302.

[8] Okubo, H. and Nishio, S., Tetsu-to-Hagame, 79-4(1993), p.497.

[9] Mitsutsuka, M., Tetsu-to-Hagane, 79(1993), p. N422.

[10] Kliegel, J. R., Proc. of the 9th Int. Sympo. on Combustion, London, (1962), p.811.

[11] Rudinger, G., AIAA Journal, 8-7,(1970), p.1288.

[12] Gokhale, S. S. and Bose, T. K., Int. J. Multiphase Flow, 15-2(1989), p.269.

[13] Zucrow and Hoffman, Gas Dynamics II, John Wily & Sons, New York,(1977), p.53.

[14] Hatta, N., Ishii, R., Takuda, H., Ueda, K. and Kokado, J., Trans. ISIJ., (1988), p.930.

[15] Hatta, N., Takuda, H. Ishii, R. and Fujimoto, H., ISIJ Int., 29(1988), p.605.

[16] Hatta, N., Fujimoto, H., Ishii, R., Umeda, Y. and Kokado, J., ISIJ Int., (1989), p.911.

[17] Hatta, N., Kokado, J., Ishii, R. and Fujimoto, H., Mem. Fac. Engg. Kyoto Univ., 51-2(1989), p.73.

[18] Hatta, N. and Nakamura, M., ISIJ Int., 29-11(1989), p.919.

[19] Hatta, N., Fujimoto, H. Ishii, R. and Kokado, J., Mem. Fac. Engg. Kyoto Univ., 52-3(1990), p.115.

[20] Hatta, N., Fujimoto, H. and Ishii, R., ISIJ Int., 31-1(1991), p.53.

[21] Hatta, N., Ishii, R. and Fujimoto, H., ISIJ Int., 31-4(1991), p.342.

[22] Hatta, N., Ishii, R. and Fujimoto, H., Trans. ASME J. Fluids Engg., 114(1992), p.420.

[23] Hatta, N., Fujimoto, H. and Takuda, H., Applied Scientific Research, 50(1993), p.129.

[24] Lee, S. L. and Srinivasan, J., Int. J. Multiphase Flow, 8-1(1982), p.47.

[25] Modarres, D., Tan, H. and Elighobashi, S., AIAA J., 22-5(1984), p.624.

[26] Wu, K. J., Santavicca, D. A., Bracco F. V., and Coghe, A., AIAA J., 22-9(1984), p.1263.

[27] Yoshida, H., Suenaga, K. and Echigo, R., Int. J. Heat Mass transfer, 33(1990), p.859.

[28] Maeda, M., ASME FED-Vol.121, (1991), p.89.

[29] Hussein, H. J., ASME FED-Vol.121, (1991), p.221.

[30] Hishida, K., Ando, A. and Maeda, K., Int. J. Multiphase Flow, 18-2(1992), p.181.

[31] Hwang, C. J. and Liu, J. L., AIAA J., 27-7(1989), p.841.

[32] Chuang, S. H., Int. J. Numerical Methods in Fluids, 9(1989), p.1413.

[33] Eklund, D. R. and Drummond J. P., AIAA J., 28-9(1990), p.1633.

[34] Iwamoto, J., Trans. ASME J. Fluids Engg., 112(1990), p.179.

[35] Abeloff, P. A., van Dalsem, W. R. and Dougherty, F. C., AIAA paper 90-3010, (1990).

[36] Kokoshima, Y., Shimizu, A. and Murao, T., FLUCOME '91 ASME, (1991), p.205.

[37] Fujimoto, H., Takahashi, O., Takuda, H., Maki, H. and Hatta, N., Proc. 5th Int. Sympo. Compu. Fluid Dynamics, 1(1993), p.211.

[38] Crowe, C. T., Sharma, M. P. and Stock, D. E., Trans. ASME J. Fluids Engg., (1977), p.325.

[39] Crowe, C. T., Trans. ASME J. Fluids Engg., 104(1982), p.297.

[40] Sharma, M. P. and Crowe, C. T., Trans. ASME J. Fluids. Engg., 111(1989), p.184.

[41] Dukowicz, J. K., J. Compu. Phys., 35(1980), p.229.

[42] Chung, J. N. and Troutt, T. R., J. Fluid Mech., 186(1988), p.199.

[43] Harlow, F. H. and Amsden, A. A., J. Compu. Phys., 17(1975), p.19.

[44] Travis, J. R., Harlow, F. H. and Amsden, A. A., Nuc. Sci. and Engg., 61(1976), p.1.

[45] Gosman, A. D., and Ioannides, E., AIAA Paper 81-0323.

[46] Kitron, A., Elperin, A. and Tamir, A., J. Thermophysics, 3-2(1989), p.112.

[47] Zhou, Q. and Leschziner, M. A., ASME FED Vol.121, (1991), p.255.

[48] Ishii, R., Umeda, Y. and Yuhi, M., J. Fluid Mech., 203(1989), p.475.

[49] Ishii, R. Hatta, N., Umeda, Y. and Yuhi, M., J. Fluid Mech., 221(1990), p.453.

[50] Chang, I. S., AIAA J.,18-12(1980), p.1455.

[51] Ishimaru, S. and Nishida, M., JSME-B, 55(1989), p.2277.

[52] Sommerfeld, M., ASME FED Vol.121, (1991), p.213.

[53] Ishizaka, K., Ikohagi, T. and Daiguji, H., Proc. 5th Int. on Compu. Fluid Dynamics, 1(1993), p.352.

[54] Mostafa, A. A., Mongia, H. C., McDonell, V. G. and Samuelsen, G. S., Int. J. Heat and Fluid Flow, 11-2(1990), p.90.

[55] Fuyuto, T. and Hayashi, K., Proc. 5th Int. Symp. on Compu. Fluid Dynamics, 1(1993), p.241.

[56] Kajitsuka, S., Morioka, K. and Saitoh, M., ASME FED-Vol. 121, (1991), p.77.

[57] Fujimoto, H., Saito, T. and Hatta, N., Shigen-to-Sozai, 109(1993),p.165.

[58] Wachters, L. H. J., Bonne, H. and van Nouhuis, H. J., Chem. Engg. Sci., 21(1966), p.923.

[59] Wachters, L. H. J. and Westerling, N. A., Chem. Engg. Sci., 21(1966), p.1047.

[60] Wachters, L. H. J. Smulders, L. Vermeulen, J. R. and Kleiweg, H. C., Chem. Engg. Sci., 21(1966), p.1231.

[61] Ueda, T., Enomoto, T. and Kanetsuki, M., Bull. of JSME, 22(1979), p.724.

[62] Pedersen, C. O., Int. Heat Mass Transfer, 13(1970), p.369.

[63] Nishio, S. and Hirata, T., JSME-B, (1977), p.3856.

[64] Nishio, S. and Hirata, T., JSME-B, (1978), p.1335.

[65] Akao, F., Araki, K., Mori, S. and Moriyama, A.,Transaction of ISIJ, 20(1980),p.737.

[66] Shoji, M., Wakunaga, T. and Kodama, K., JEME-B, 50(1984), p.716.

[67] Poddubenko, V. V. and Yablonik, R. M., Fluid Mechanics-Soviet Research, 19-3(1990), p.111.

[68] Xiong, T. Y. and Yuen, M. C.,Int. J. Heat and Mass Transfer, 34(1991), p.1881.

[69] Chandra, S. and Avedisian, C. T., Proc. R. Soc. Lond. A, 432,(1991), p.13.

[70] Chandra, S. and Avedisian, C. T.,Int. J. Heat Mass Transfer, 35-10(1992), p.2377.

[71] Min, J., Sako, M. and Kikuchi, Y., JSME-B, 57(1991), p.157.

[72] Min, J. and Kikuchi, Y., JSME-B, 58(1992), p.166.

[73] Jeffrey, D. N. and Patrik, V. F.,SAE technical paper, 930919(1993).

[74] Rymkiewicz, J. and Zapalowicz, Z., Int. Comm. Heta Mass Transfer, 20(1993), p.687.

[75] Harlow, F. H. and Shannon, J. P., J. Applied Phys., 38(1967), p.3855.

[76] Turutani, K., Yao, M., Senda, J. and Fujimoto, H., JSME-B, 55(1989), p.814.

[77] Nishikawa, N., Amazu, S. and Suzuki, T., J. Soc. Simul. Tech., 7-3(1989), p.27.

[78] Hatta, N., Fujimoto, H., Takuda, H., Takahashi, O. and Kinoshita, K., To be published in ISIJ Int..

[79] Hatta, N., Fujimoto, H. and Takuda, H., To be published in Trans. ASME J. Fluids Engg..

[80] Fujimoto, H. and Hatta, N., To be submitted for Trans. ASME J. Fluids Engg..

[81] Harlow, F. H. and Welch, J. E.,1965, Physics of Fluids, 8(1965), p.2182.

[82] Miyata, H., J. Compu. Phys., 65(1986) p.179.

Chapter 2

Theoretical model of two-phase flow in a nozzle and its application to numerical experiments

[10]

2.1 Introduction

A number of processes in iron- and steelmaking industries positively introduce the utilization of two-phase or multiphase flows. For example, the mist cooling method, which is commonly applied to the secondary cooling zone of continuously cast slabs, is different from other kinds of cooling methods in a few points. First, the mist consists of two-phase, that is, gas-particle mixtures. Second, the flow pattern in a nozzle varies with the loading ratio, that is, the particle-to-gas mass flow rate ratio. Third, the change in the loading ratio has an appreciable effect on the cooling intensity for the solidified shell. Fourth, the difference in particle size brings on a change in the slip ratio, that is, the ratio of particle velocity to gas velocity, when a continuous distribution of particle size is present.

From such a point of view, the analysis of a two-phase flow in a nozzle is of importance for designing the nozzle to control the mist cooling intensity. However, we suppose that this investigation is not fresh from a historical point of view. This would originate from the development of the propulsive nozzle of the rocket motor[1-3].

Zucrow and Hoffman[4] have described the system of equations governing the steady quasi-one-dimensional flow of a gas-particle mixture. It consists of a particle continuity equation, a particle momentum equation, a particle energy equation, a particle equation of state, a gas continuity equation, a gas momentum equation, a gas energy equation and a gas equation of state. Then, we have rearranged the above system of equations so that the system gives a fit to the case where particles have a continuous distribution of particle size[5]. This is because it is far more common to consider that particles in a two-phase do not have a single size, but take a continuous distribution of size. Again, the nozzle flow of mist consisting of gas and liquid particles has been analyzed from a numerical point of view. By so doing, the situation has been premised where a gas

containing suspended liquid-particles is initially stored in a relatively large reservoir, and the gas-particle mixture directly flows through a nozzle. However, the reservoir pressure is not allowed to be so high that the gas velocity is beyond the sonic region, because the system of equations described in Ref.(5) is singular in the transonic region.

Thereafter, we have extended the governing equations so that they cover the whole gas velocity regions from the subsonic to the supersonic velocities through the throat of a converging-diverging nozzle[6]. In reality, only the equation to determine the gas velocity has been modified in the form. That is, the equation has been rewritten into the form including the term of pressure profile, instead of the term of the variational nozzle cross-sectional area along the whole nozzle length.

In the present chapter, we wish to review the system of equations governing the nozzle flow of gas-particle mixture to evaluate all the flow properties in the flow field. Next, we examine the numerical treatment of the system of governing equations for the situation where the equation for the determination of gas-phase velocity is singular in the transonic region. Again, we wish to consider the problem concerning the perturbation procedure between the equilibrium and non-equilibrium flows from a point of view of computational physics. Then, the theoretical model is applied to the case where a gas-particle mixture is composed of air and water-particles in relation to the mist nozzle flow adopted to the secondary cooling zone of continuously cast slab. The results so obtained are examined and discussed from a numerical point of view.

2.2 Governing equations

According to Zucrow and Hoffman[4], the theoretical flow model for a gas carrying suspended condensed particles will be constructed on the following assumptions:

(1) The flow is steady and quasi-one-dimensional, and the mass flow rate for both gas- and particle-phases is conserved in a system.

(2) The system of gas-particle mixture flow in a nozzle is independent of the external system. So that, there is no external work, no external heat transfer through the nozzle wall friction, and no gravitational effect.

(3) All of the particles are spherical in shape, incompressible and do not interact with each other. Also, there is no internal temperature distribution in particles.

(4) The particles exert a drag force on the flowing gas, and the particles transfer the heat to the gas in the form proportional to the temperature difference between gas and particle. Again, the gas as well as the particles have a constant specific heat.

(5) The particles occupy negligible volume; that is, the ratio of the gas density to the material density of particles is negligibly small.

The governing equations are expressed nondimensionally in terms of the following dimensionless variables:

$$x = \bar{x}/\bar{L}_*, \quad A = \bar{A}/\bar{A}_*, \quad \rho = \bar{\rho}/\bar{\rho}_0, \quad p = \bar{p}/\bar{p}_0, \quad V = \bar{V}/\bar{a}_0,$$
$$V_p = \bar{V}_p/\bar{a}_0, \quad T = \bar{T}/\bar{T}_0, \quad T_p = \bar{T}_p/\bar{T}_0, \quad r_p = \bar{r}_p/\bar{l}_p, \quad \phi = \bar{l}_p \bar{\phi}(\bar{x}, \bar{r}_p) \tag{2.1}$$

in which, x, A, ρ, p, V, T, r_p and ϕ denote the coordinate along nozzle axis, the sectional area of nozzle, the gas density, the pressure, the gas velocity, the gas temperature, the particle radius and the continuous distribution function of particle size, respectively. And $\bar{L}_*, \bar{l}_p$ and $\bar{a}_0$ are the radius of nozzle at throat, the mean particle radius of particles and the speed of sound at a reservoir. The subscripts $0, *$ and p denote the reservoir condition, the nozzle throat condition and the particle-phase, respectively. Also, overbars give the dimensioned quantities.

The governing equations for the nozzle flow of the gas-particle mixture are given by

$$V_p(r_p)\frac{d}{dx}V_p(r_p) = A_{p0}f_pT^\delta\frac{V-V_p(r_p)}{r_p^2} \tag{2.2}$$

$$V_p(r_p)\frac{d}{dx}T_p(r_p) = \lambda A_{p0}g_pT^\delta\frac{T-T_p(r_p)}{r_p^2} \tag{2.3}$$

$$\dot{m}_p(r_p) = \rho_p(r_p)AV_p(r_p), \quad \dot{M}_p = \int \dot{m}_p(r_p)dr_p \tag{2.4}$$

$$\rho V\frac{dV}{dx} + \nu_0\int\rho_p(r_p)V_p(r_p)\frac{dV_p(r_p)}{dx}dr_p + \frac{1}{\gamma}\frac{dp}{dx} = 0 \tag{2.5}$$

$$T = 1 + \nu\theta - \frac{1}{2}(\gamma-1)V^2 - \nu_0\int\frac{\dot{m}_p(r_p)}{\dot{M}_g}\left[\theta T_p(r_p) + \frac{1}{2}(\gamma-1)V_p^2(r_p)\right]dr_p \tag{2.6}$$

$$\rho = p/T \tag{2.7}$$

$$\dot{M}_g = \rho AV \tag{2.8}$$

where $\dot{m}_p$, $\dot{M}_p$ and $\dot{M}_g$ are dimensioless mass flow rate function of particle, dimensionless mass flow rate for particle-phase and dimensionless gas mass flow rate respectively, and γ is the gas specific heat ratio.

To complete the system of Eqs.(2.2) to (2.8), another equation should be introduced for the determination of gas velocity V.

In the case where nozzle configurations are previously prescribed the next equation,

$$\frac{dV}{dx} = -\frac{M^2}{1-M^2}\frac{1}{V}\left[\frac{T}{A}\frac{dA}{dx} - \frac{\nu_0\gamma A_{p0}T^\delta}{\rho}\int\rho_p(r_p)f_p\frac{V-V_p(r_p)}{r_p^2}dr_p\right.$$
$$\left. +\nu_0 A_{p0}T^\delta\int\frac{\dot{m}_p(r_p)}{\dot{M}_g}\frac{1}{r_p^2}\left\{\theta\lambda g_p\frac{T-T_p(r_p)}{V_p(r_p)} + (\gamma-1)f_p(V-V_p(r_p))\right\}dr_p\right] \tag{2.9}$$

is valid to the determination of V. Obviously, a singularity at $M = 1$ (M: Mach number) arises in the above equation.

In the case where pressure profiles are previously prescribed over the whole length of nozzle, the following equation,

$$\frac{dV}{dx} = -\frac{\nu_0}{\rho V}\int\rho_p(r_p)A_{p0}f_pT^\delta\frac{V-V_p(r_p)}{r_p^2}dr_p - \frac{1}{\gamma\rho V}\frac{dp}{dx} \tag{2.10}$$

is applicable to the determination of V. According to Zucrow and Hoffman, the determination method of V by Eq.(2.9) will be called the specified area method (SAM) and that by Eq.(2.10) will be termed the specified pressure method (SPM).

It should be remarked that the integration appearing in Eqs. (2.4) to (2.6) and Eqs. (2.9) and (2.10) indicates the definite one taken over all sizes in $[r_{p,min}, r_{p,max}]$ and the lower and upper limits are omitted. Here, $r_{p,min}$ and $r_{p,max}$ are the dimensionless minimum and maximum radii of the particles contained in the mixture.

Next, the description of dimensionless parameters in Eqs.(2.2) to(2.10) is as follows:

$$A_{p0} = \frac{9}{2}\frac{\bar{\mu}_0 \bar{L}_*}{\bar{\rho}_{mp}\bar{l}_{p0}^2 \bar{a}_0} \quad \text{and} \quad f_p = \frac{C_D}{C_{D,Stokes}} \tag{2.11}$$

in which, C_D is the drag coefficient based upon the Henderson correlating equation[7] and $C_{D,Stokes}(= 24/Re_p)$ shows the Stokes law of drag coefficient for spheres. Also, $\bar{\mu}_0$, $\bar{\rho}_{mp}$ and Re_p are the gas viscosity, the particle material density and particle Reynolds number, respectively.

$$Re_p = Re_{p0}\frac{r_p|V - V_p(r_p)|}{T^\delta/\rho}, \quad Re_{p0} = \frac{2\bar{l}_{p0}\bar{a}_0}{\bar{\mu}_0/\bar{\rho}}, \quad \bar{\mu} = \bar{\mu}_0 T^\delta \tag{2.12}$$

$$\lambda = \frac{2\bar{C}_{pg}}{3Pr\bar{C}_{pp}}, \quad g_p = \frac{Nu}{Nu_{Stokes}}, \quad \theta = \frac{\bar{C}_{pp}}{\bar{C}_{pg}} \tag{2.13}$$

where, Nu is the particle Nusselt number based upon the empirical expression by Carlson and Hoglund[8] and Nu_{Stokes} (=2) is the Nusselt number in the Stokes flow regime. $\bar{C}_{pg}$, $\bar{C}_{pp}$ and Pr denote the gas specific heat at constant pressure, specific heat of particle material and gas-phase Prandtl number.

Again, other remaining parameters are defined as

$$\bar{l}_p = \left[\int \bar{r}_p^3 \bar{\phi}(\bar{x}, \bar{r}_p)d\bar{r}_p\right]^{1/3} \tag{2.14}$$

$$\dot{M}_g = \frac{\bar{\dot{M}}_g}{\bar{\rho}_0 \bar{a}_0 \bar{A}_*} \quad \text{and} \quad \dot{M}_p = \frac{\bar{\dot{M}}_p}{\bar{R}_{p0}\bar{a}_0 \bar{A}_*} \tag{2.15}$$

$$\nu = \frac{\dot{M}_p}{\dot{M}_g}\nu_0 \quad \text{and} \quad \nu_0 = \frac{\bar{R}_{p0}}{\bar{\rho}_0} \tag{2.16}$$

where $\bar{R}_{p0}$ indicates the density of condensed particle per unit volume of flowing medium.

2.3 Numerical procedure

Among the equations mentioned above, Eqs.(2.2) to (2.8) comprise a set of 7 equations for determining 7 flow properties ρ, T, V, $\rho_p(r_p)$, $V_p(r_p)$, $T_p(r_p)$ and A. These equations should be combined in a form appropriate for seeking a numerical solution. However, the initialization is very tedious at the start of numerical calculation.

Let us suppose that a gas containing suspended liquid-particles is initially stored in an appreciably large reservoir, and that the gas-particle mixture directly flows through a nozzle. In this case, it is far more common to consider that the gas velocity as well as particle velocity is zero at the reservoir. Hence, the initial situation area of nozzle is infinite at its entrance. So, the problem remains how the numerical treatment should be made at the first computational step.

When $V_p(r_p) = V$ and $T_p(r_p) = T$ for all r_p, the particles are commonly said to be in velocity and thermal equilibrium with the gas. Also, such a mixture flow is called the equilibrium flow. While the flow obeying the Eqs.(2.2) to (2.8) is termed the nonequilibrium flow.

Then, it is assumed that all of the particles are in velocity and thermal equilibrium with the gas only near the reservoir so that the gas as well as all of the particles may take a non-zero velocity at the entrance of the nonequilibrium region. In short, one should be bear in mind that the initial point of nonequilibrium region, in a numerical sense, corresponds to the end point of equilibrium flow, and that the aforementioned system of equations governing the nonequilibrium flow is solved as a perturbation from an equilibrium reference flow.

Hence, we wish to describe the problem of the constant lag approximation. Let us now define the following two lag factors,

$$K_p(r_p) = \frac{V_p(r_p)}{V} \quad \text{and} \quad L_p(r_p) = \frac{1 - T_p(r_p)}{1 - T} \tag{2.17}$$

As can be understood from the numerical procedure mentioned above, it holds true in the equilibrium region that $K_p(r_p) = 1$ as well as $L_p(r_p) = 1$ for all r_p. While $K_p(r_p)$ and $L_p(r_p)$ is not constant in the nonequilibrium region, but variable along the nozzle axis x (i.e., $K_p(r_p) \equiv K_p(x, r_p)$ and $L_p(r_p) \equiv L_p(x, r_p)$). In fact, the results of an equilibrium analysis for the case where $1 - K_p = 1 - L_p = 0$ is an upper limit for an actual flow, and the frozen analysis for the case where $1 - K_p = 1 - L_p = 1$ is a lower limit. One should keep in mind that the actual values of the flow properties must lie between the values for such two limiting situations.

For the general case of constant lags including the equilibrium flow, we have

$$p\rho^{-\hat{\gamma}} = 1 \tag{2.18}$$

Here, $\hat{\gamma}$ is derived as follows:

$$\hat{\gamma} = \frac{\gamma(1 + \Gamma_1)(1 + \Gamma_3)}{\gamma(1 + \Gamma_1)(1 + \Gamma_3) - (\gamma - 1)(1 + \Gamma_2)} \tag{2.19}$$

where,

$$\Gamma_1 = \nu_0 \int \phi_0(r_p)r_p^3 K_p^2(r_p)dr_p \tag{2.20}$$

$$\Gamma_2 = \nu_0 \int \phi_0(r_p)r_p^3 K_p^3(r_p)dr_p \tag{2.21}$$

$$\Gamma_3 = \nu_0\theta \int \phi_0(r_p)r_p^3 K_p(r_p)L_p(r_p)dr_p \tag{2.22}$$

Table 2.1: Physical constants and reference conditions adopted in numerical experiments. These parameters are fixed throughout the present paper.

Physical constants	Reference conditions
$\bar{\rho}_{mp}$=1000 [kg/m^3]	T_0 =323 [K]
$\bar{C}_{pp}$=4187 [J/kg·K]	$\bar{\mu}_0 = 2.07 \times 10^{-5}$ [Pa·s] at $\bar{T}_0$
$\bar{C}_{pg}$=1004 [J/kg · K]	$\bar{L}_* = 1.0 \times 10^{-3}$ [m]

Again, in the region from the reservoir up to the end point of the equilibrium flow both the particle velocity lag and the thermal lag are here taken to be zero (i.e., $K_p(r_p) = 1$ and $L_p(r_p) = 1$ for all r_p). All of the flow properties in the equilibrium region can be calculated by

$$\rho = p^{1/\gamma} \tag{2.23}$$

$$T = p/\rho \tag{2.24}$$

$$V = \left\{ \frac{2(1-T)}{\gamma - 1} \cdot \frac{1 + \Gamma_3}{1 + \Gamma_2} \right\}^{1/2} \tag{2.25}$$

$$\dot{M}_g = \rho A V \tag{2.26}$$

2.4 Numerical experiments

2.4.1 Computational conditions

A few numerical experiments will be performed in order to demonstrate the numerical results concerning the flow properties in a nozzle. For the numerical calculation, a gas-particle mixture composed of air and water particles is treated. The physical constants as well as the reference conditions adopted in this numerical experiment are listed in Table 2.1. These parameters are fixed throughout the present paper.

It is very difficult to specify the distributing function of the radius of the spherical water-particles mixing in the mist. Then, let it be assumed that $\bar{\phi}_0(\bar{r}_p)$ is somewhat arbitrarily given by

$$\bar{\phi}_0(\bar{r}_p) = \bar{J}\bar{r}_p \exp\left(-\frac{\bar{r}_p^2}{250}\right) \tag{2.27}$$

where $\bar{J}$ is the normalizing factor. If it is assumed that the minimum and the maximum radii of the particles contained in the mixture are specified as

$$\bar{r}_{p,min} = 1.0[\mu m] \quad \text{and} \quad \bar{r}_{p,max} = 50[\mu m], \tag{2.28}$$

Table 2.2: Size number i, dimensionless particle radius and continuous distribution function.

i	$r_p(i)$	$\phi_0(r_p(i))$
1	0.0575	0.1391
2	0.3392	0.7168
3	0.6208	0.9458
4	0.9025	0.8179
5	1.1842	0.5269
6	1.4658	0.2642
7	1.7475	0.1053
8	2.0292	0.0337
9	2.3108	0.0087
10	2.5925	0.0018
11	2.8742	0.0003

we have $\bar{J} = 1/124.58[\mu m^{-2}]$. Again, the average radius $\bar{l}_{p0}$ has been found to be 17.396 $[\mu m]$, and the continuous distribution of the particle size from 1 $[\mu m]$ up to 50 $[\mu m]$ is represented by eleven discrete sizes so that the size interval may be constant. Each size is made dimensionless according to the definition by $r_p(i) = \bar{r}_p(i)/\bar{l}_{p0}$ ($i = 1 \sim 11$). Table 2.2 indicates the size number i, $r_p(i)$ and $\phi_0(r_p(i))$.

The two cases are considered in our numerical experiments, one of which corresponds to the case where the gas velocity does not reach the sonic state throughout the whole nozzle length. In this case, the specified area method is applicable to the determination of the gas velocity (see Eq.(2.9)). The other corresponds to the case where the gas velocity is beyond the sonic state, and the specified pressure method is applied for determining the gas velocity (see Eq.(2.10)). In this case, the pressure profile should be provided over the whole length of the nozzle axis. If so, the nozzle geometry can be designed in accord with the pressure profile.

2.4.2 Numerical results of subsonic nozzle flow

First, the nozzle geometry should be given. Here, the sectional area of the nozzle is assumed to consist of the two regions from the reservoir to the nozzle exit as

$$\begin{array}{ll} \text{in the region of} \quad x < 0; & A = \frac{1}{5}x^2 + 1 \\ \text{in the region of} \quad 0 \le x \le X_E; & A = 1 \end{array} \tag{2.29}$$

in which X_E=25 is adopted. Also, we set $\bar{L}_*$=1.0 [mm] throughout the present paper.

Here, the case is treated where $\bar{p}_0 = 1.8 \times 10^5$ [Pa] at the reservoir. Figures 2.1(a) to 2.1(c) give the variation of the pressure, velocity and temperature of the gas-phase along the nozzle axis x with ν as a parameter. It should be kept in mind that $\nu = 0$ corresponds to the gas-only flow. It can be seen from these figures that p and T remain almost unvaried from the reservoir up to a certain position, but they rapidly change as

x attains zero. Also, V is seen to grow very gradually from the reservoir up to a certain position, and then to increase rapidly as $x \to 0$. In the region where the sectional area of the nozzle is constant ($A = 1$), (Hereafter, this will be called the parallel region) the variational behaviors of p, V and T are observed to be relatively smooth. In particular, for the case where $\nu = 0$, p, V and T remain unvariable in the parallel region. p is at a higher state with ν, while V is at a lower state. One should bear in mind that the gas-phase pressure in the mixture flow is taken to be equal to the ambient gas pressure ($\bar{p}_e = 1.0 \times 10^5 [\mathrm{Pa}]$) at the nozzle exit (at $x = X_E$), and that $\dot{M}_g$ is determined in such a way as to satisfy the condition.

Figures 2.2(a) to 2.2(c) give the variation of the particle velocity $V_p\{r_p(i)\}$ (i; size number, see Table 2.2) along the nozzle axis x. It can be observed that $V_p\{r_p(i)\}$ is increased with x, and the particles of a smaller size tend to travel at a higher velocity. Also, when ν is decreased, $V_p\{r_p(i)\}$ increases.

Figures 2.3(a) to 2.3(c) indicate the relation between $K_p\{r_p(i)\}$ and x. The slip ratio is changeable along x, depending upon the particle size.

Figures 2.4(a) to 2.4(c) exhibit the variation of $L_p\{r_p(i)\}$ with x. The variational behavior of $L_p(r_p)$ is observed to be similar to that of $K_p(r_p)$ in the form. $L_p(r_p)$ as well as $K_p(r_p)$ takes the minimum value near $x = 0$.

2.4.3   Numerical results of supersonic nozzle flow

First, a pressure profile is given, such that p reaches unity as $x \to x_0$ and $p = 0.1$ at $X_E = 25$. Here, the following pressure profile,

$$p = -k_1 \frac{g(x)}{\sqrt{(\{g(x)\}^2 + 1)}} + (1 - k_1); \qquad g(x) = k_2 x + k_3 \tag{2.30}$$

is adopted. Here, k_1=0.451000, k_2=0.421457 and k_3=0.046614. We note that $p = 0.528$ at $x = 0$ and the position of $x = 0$ corresponds to that of the throat for the gas-only flow. Figure 2.5 indicates the variation of p with x.

For the super sonic nozzle flow, the case is considered where $\bar{p}_0 = 10.0 \times 10^5$ [Pa] at the reservoir. Figure 2.6 indicates the variation of L with x, that is, the nozzle configuration along the nozzle axis, with ν as a parameter. In this figure, it should be noted that $\nu = 0$ corresponds to the gas-only flow, and that the throat is not located at $x = 0$, except for the case of $\nu = 0$. The throat exhibits the tendency to be located at the slightly negative side of x with the increase in ν (at $x = -0.102$ for ν=1, at $x = -0.185$ for $\nu = 3$ and $x = -0.244$ for ν=5). It can be seen from this figure that L is extended in the convergent as well as divergent parts with an increase of the loading ratio ν.

Figures 2.7(a) to 2.7(c) give the variation of V, T and ρ along x, with ν as a parameter. We note that the indication of these flow properties exactly obeys the axis of the nozzle configuration shown in Figure 2.7, particularly in the case where $\nu = 0$, T_*=0.833 and ρ_*=0.634 at the throat ($A_* = 1$). The values coincide with those calculated from $T_* = 2/(\gamma+1)$ and $\rho_* = p_*^{1/\gamma}$ ($= T_*^{1/(\gamma-1)}$; $p_* = 0.528$). When $\nu = 0$, T is seen to decrease rapidly near the throat, and then only gradually decreases as x reaches X_E. This is considered to be due to the the isentropic change of gas. Therefore, in this case, V increases also rapidly near the throat, and then very gradually decreases as x attains the nozzle exit
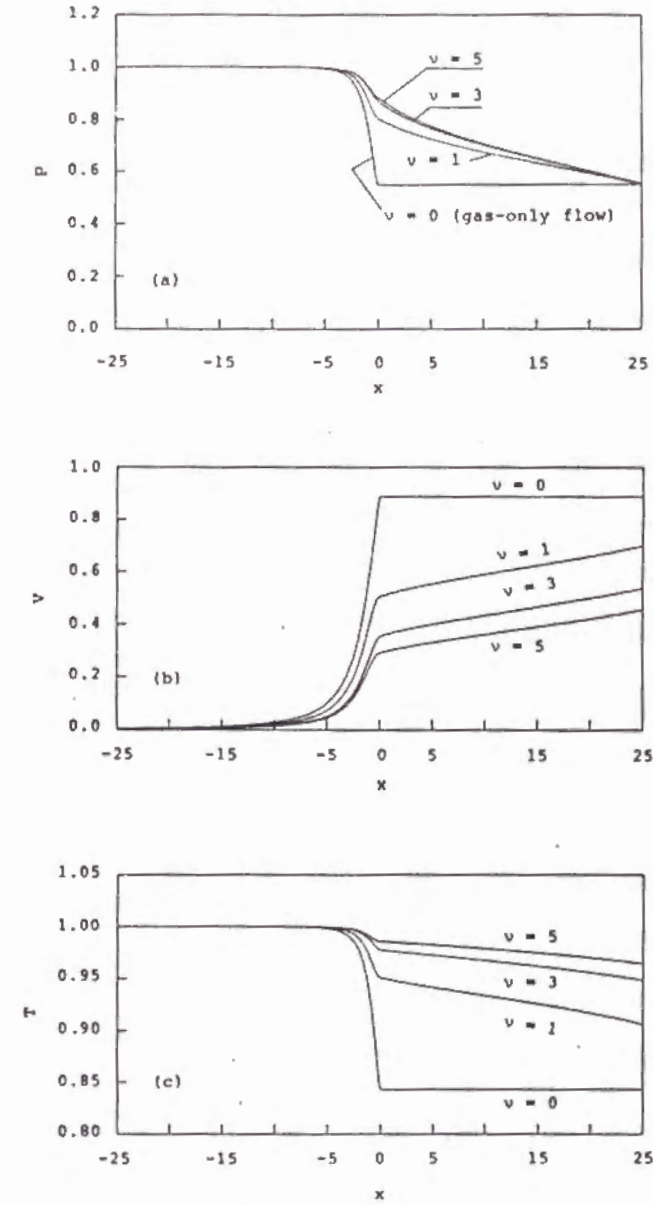

Figure 2.1: Variation of pressure (a), velocity (b) and temperature (c) of gas-phase along the nozzle axis. Note that $\bar{p}_0 = 1.0 \times 10^5$ [Pa], and that the gas-phase pressure in the mixture flow is conditioned to be equal to the ambient gas pressure ($= \bar{p}_e$) at the nozzle exit.
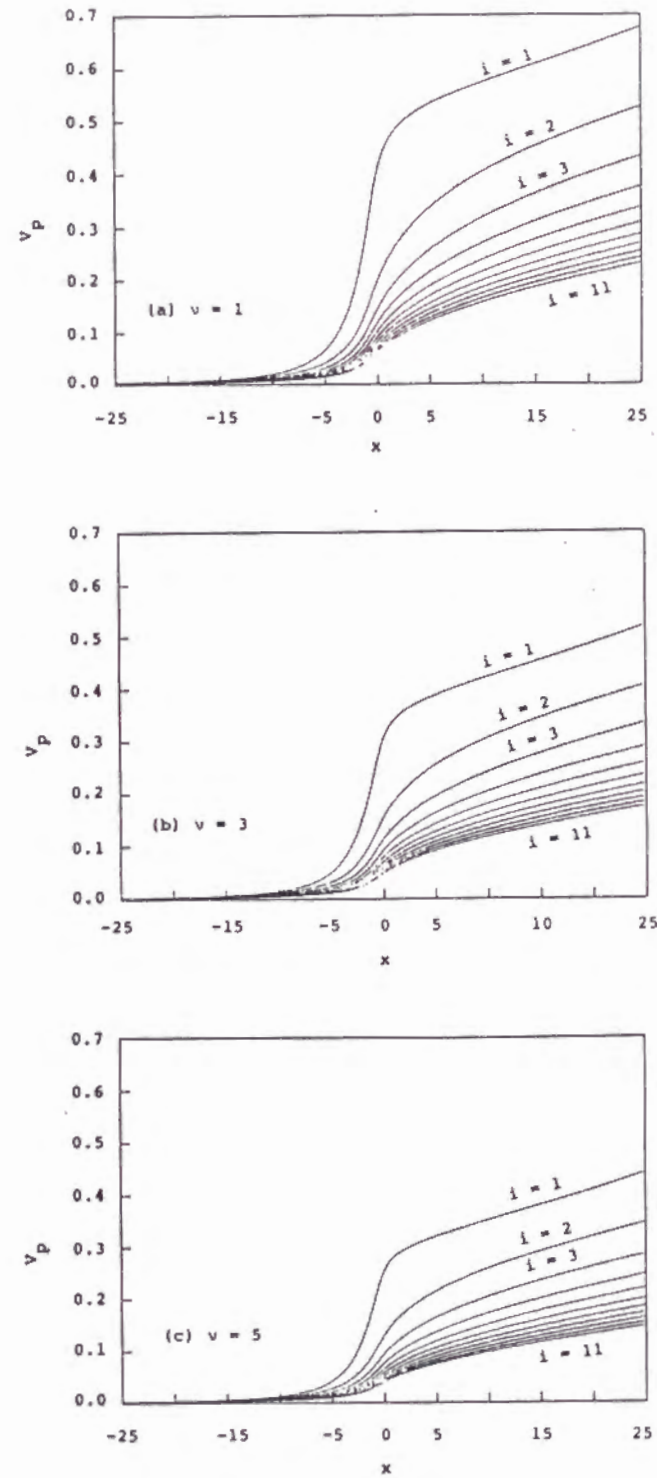
Figure 2.2: Variation of particle velocities along nozzle axis for $\nu = 1.0$ (a), $\nu = 3.0$ (b) and $\nu = 5.0$ (c). Note that i is the size number to present the particle radius.
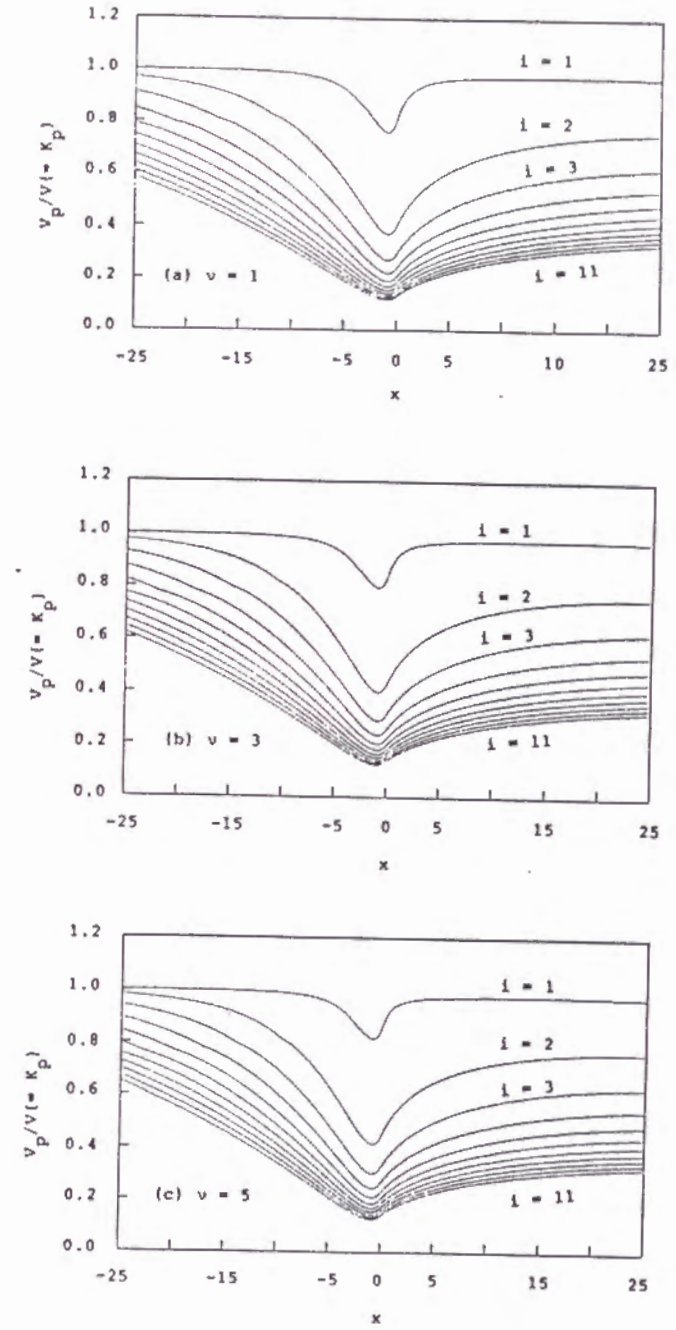

Figure 2.3: Variation of slip ratio, defined in Eq.(2.17), with nozzle axis for $\nu = 1.0$ (a), $\nu = 3.0$ (b) and $\nu = 5.0$ (c) (i:size number).

Figure 2.5: Pressure profile along nozzle axis adopted. Note that this profile was previously given as a function of x, and corresponds to Eq.(2.30)
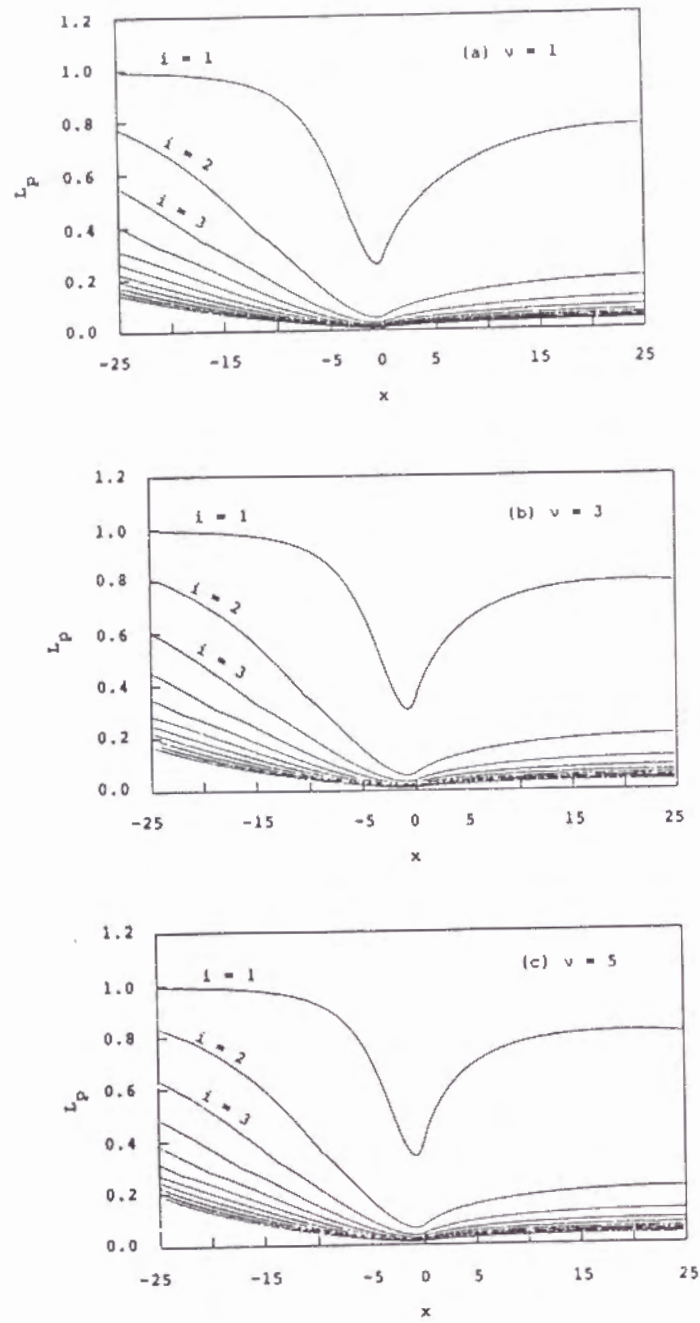

Figure 2.4: Variation of thermal lag factor $L_p(r_p)$, defined in Eq.(2.17), along nozzle axis for $\nu = 1.0$ (a), $\nu = 3.0$ (b) and $\nu = 5.0$ (c).
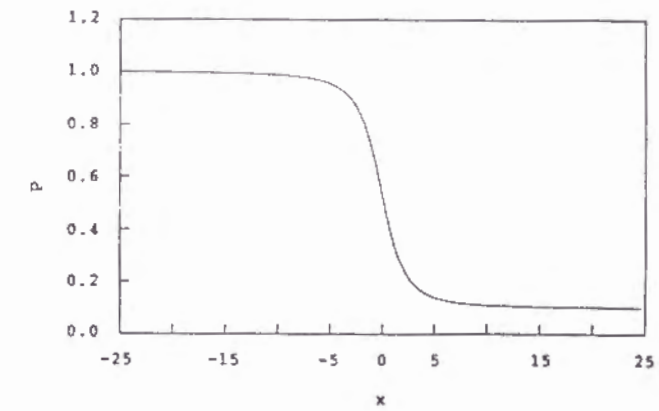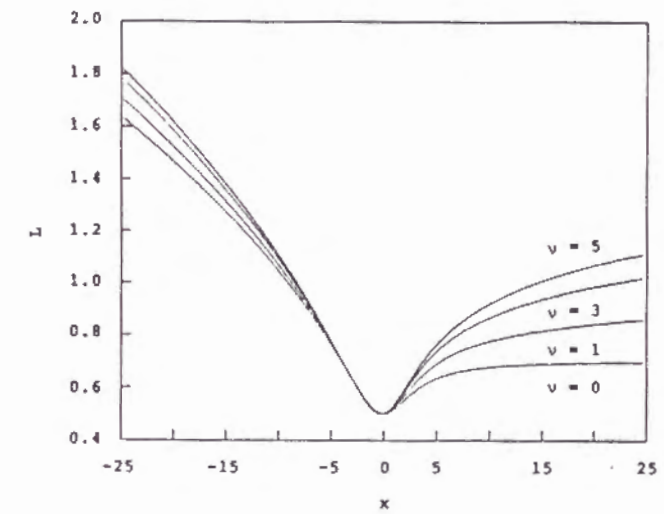

Figure 2.6: Nozzle geometry calculated according to pressure profile shown in Figure 2.5. Note that $\bar{p}_0 = 10.0 \times 10^5$ [Pa] for the supersonic nozzle flow and $\bar{p}_0 = 1.0 \times 10^5$ [Pa], and that gas-phase pressure in the mixture flow is taken to be equal to the ambient gas pressure ($p_e = 0.1$).

(see Figure 2.7(a)), although this is closely related to the pressure profile given in the form of Figure 2.6. However, it is apparent from these figures that the case where $\nu \neq 0$ is different from the case of $\nu = 0$. That is, T decreases once rapidly near the throat, and thereafter increases towards the nozzle exit to a considerable degree. Again, T is observed to be higher in the divergent part of the nozzle with the increase in ν. On the other hand, V becomes large sharply near the throat, but somewhat gradually decreases as x reaches X_E. Furthermore, ρ decreases with x in a form similar to the pressure profile. ρ in the case where $\nu \neq 0$ is small in comparison with the case of gas-only flow (see Figure 2.7(c)).

Figure 2.8 indicates the variation of $M(= V/\sqrt{T})$ against x, with ν as a parameter. For the case where $\nu \neq 0$, the x-axis of $M = 1$ is seen to be located downstream from the throat, and such a tendency presents itself in a more conspicuous manner as ν is increased. Also, M increases rapidly near the throat, and then decreases gradually towards the nozzle exit for the case where $\nu \neq 0$. The variational behavior of M against x is similar to that of V in the form.

Figures 2.9(a) to 2.9(c) give the variation of $V_p\{r_p(i)\}$ against x, with i as a parameter. It can be seen from these figures that $V_p\{r_p(i)\}$ is, as a whole, increased with x, except for the case where $i = 1$. Particles with a smaller radius tend to flow at a higher velocity. Again, the increase in ν brings about the decrease in particle velocities. In addition, it is interesting to note that only the particle velocity profile of $i = 1$ is near to the gas velocity profile corresponding to the same loading ratio.

Figures 2.10(a) to 2.10(c) show the variations of $K_p\{r_p(i)\}$ along x, with i as a parameter. It is clear from these figures that $K_p\{r_p(i)\}$ becomes higher as r_p becomes smaller. Again, $K_p(r_p)$ decreases in the region from the reservoir to the throat and the inverse occurs downstream from the throat. Furthermore, it should be stressed that the difference in ν does not give a significant change to the slip ratio.

Figures 2.11(a) to 2.11(c) exhibit the variation of $L_p(r_p)$ along x, with i as a parameter. This is similar to the case of the slip ratio. $L_p(r_p)$ also decreases upstream from the throat and the opposite occurs downstream from the throat.

2.5 Discussion

According to the theoretical procedure described in the third section, a few calculation examples have been demonstrated.

First, we discuss the numerical results for the subsonic nozzle flow. In this case, all of the flow properties have been calculated on the basis of the nozzle geometry given in Eq.(2.29). What is remarkable is that the flow properties vary even in the parallel region for the case where $\nu \neq 0$, while for $\nu = 0$, p, T and V remain unvaried in the parallel region.

Now, we wish to discuss the effect of the reservoir pressure $\bar{p}_0$. In order to do so, we treat the case where $\nu = 3$. The other computational conditions are the same as the previous case. Figure 2.12 gives the variation of the local Mach number of the gas-phase along the nozzle axis with $\bar{p}_0$ as a parameter. It can be seen from this figure that M reaches unity at $x = X_E$ with the increase in $\bar{p}_0$.

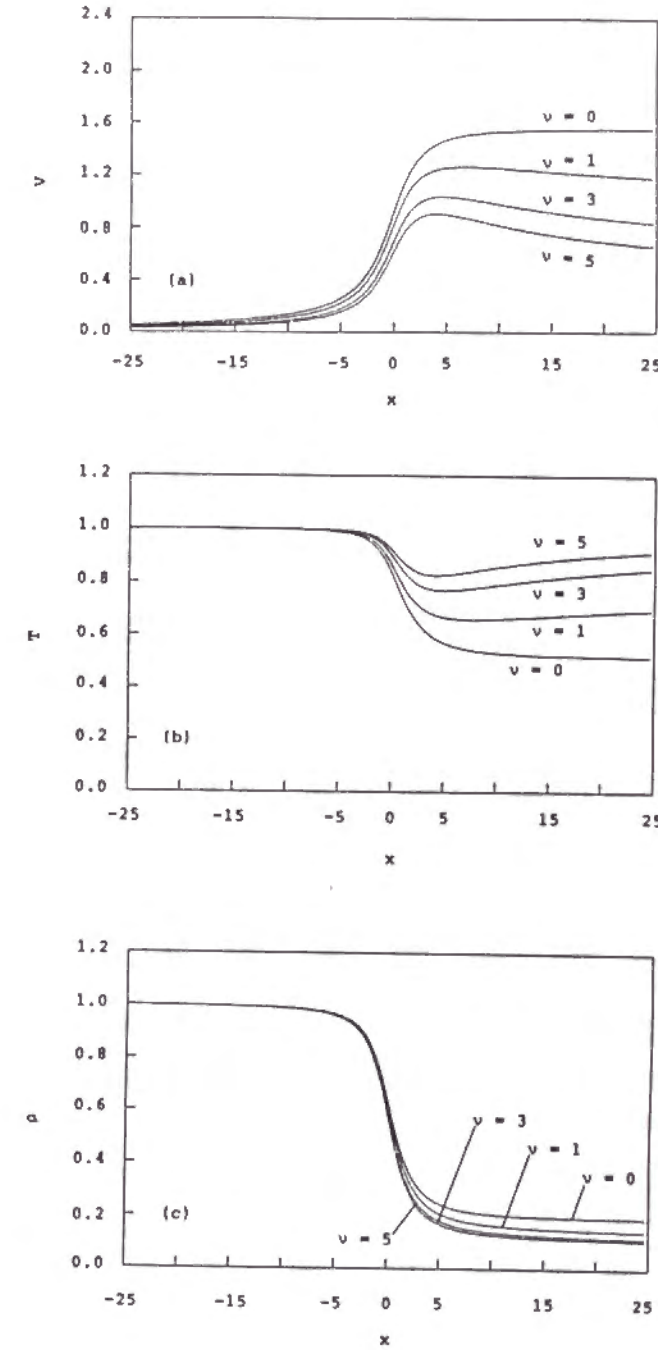As mentioned above, Eq.(2.9) is singular in the transonic region. Therefore, when the

Figure 2.7: Variation of velocity (a), temperature (b) and density (c) of gas-phase along nozzle axis.
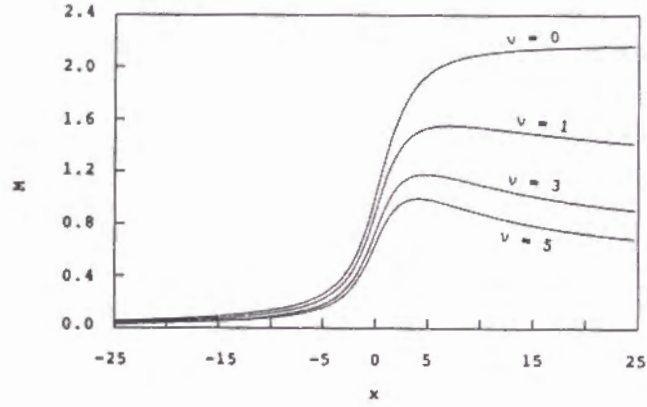
Figure 2.8: Relation between local gas-phase Mach number and nozzle axis. Note that for $\nu = 0$, the x-coordinate of $M = 1$ is seen to be located not at the throat, but downstream from the throat.

supersonic nozzle flows are treated for a given nozzle geometry, the specified area method should be employed upstream and downstream from that region. The specified pressure method should be employed in the transonic region. That is, first, at a given upstream point, the specified pressure method is adopted as a perturbation from the numerical results obtained by the specified area method. Second, at a certain downstream point, the specified area method is adopted as a perturbation from the numerical results calculated by the specified pressure method, one should keep in mind that the inconvenient gas occurs between the calculated nozzle sectional area and the previously determined area. This problem is reported in Ref.[9].

In the present case, we confine our interest to the subsonic flow regime. Again, the increase in $\bar{p}_0$ leads not only to prompting the gas-phase velocity as well as the particle-phase velocity, but also to increasing the mass flow rates of the two phases regardless of the magnitude of ν[5].

Again, it should be emphasized that the aforementioned system of equations governing the non-equilibrium flow has been solved as a perturbation from an equilibrium reference flow. The position where V is given by $0.001\sqrt{2/(1+\gamma)}$ is regarded as the end point of the equilibrium region.

Next, we discuss the numerical results for the supersonic nozzle flow. Using the pressure profile given by Eq.(2.30), it has been shown that the nozzle geometry can be designed in obedience to the desired pressure profile. At the same time, it has been demonstrated that all of the flow properties in the whole region from the subsonic flow to the supersonic flow can be obtained according to the pressure profile given by previously along the nozzle axis.

Here, let us prove that $\dot{M}_p = \dot{M}_g$ in the dimensionless space. It holds true that

$$\bar{\dot{M}}_g = \bar{\rho}\bar{V}\bar{A} \quad \text{and} \quad \bar{\dot{M}}_p = \bar{R}_p\bar{V}\bar{A} \tag{2.31}$$

on the condition that $\bar{V}_p(r_p) = \bar{V}$ in the equilibrium region. Hence,
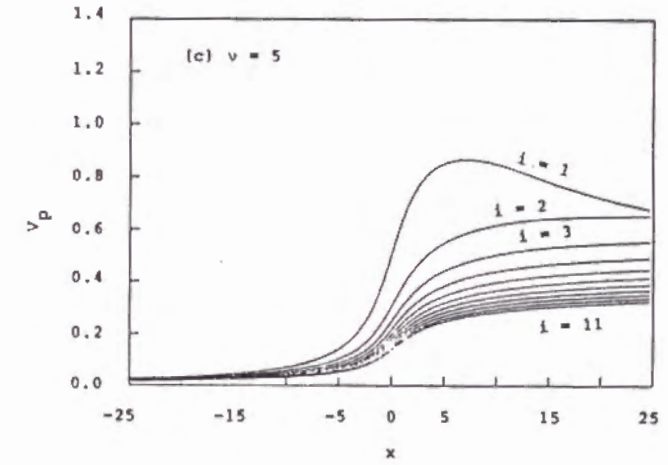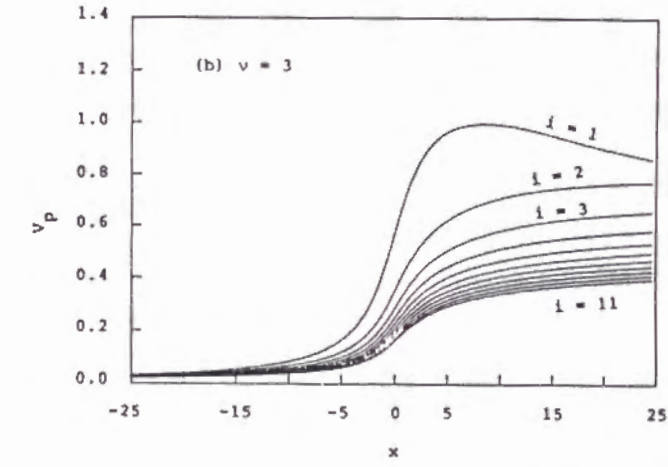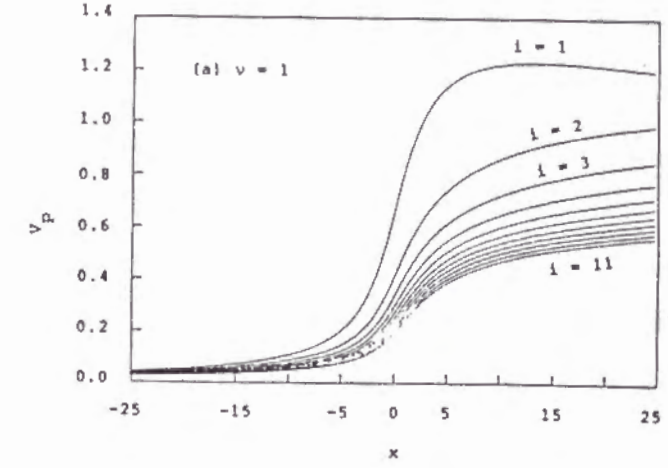
Figure 2.9: Variation of particle velocities along nozzle axis (i: size number) for $\nu = 1.0$ (a), $\nu = 3.0$ (b) and $\nu = 5.0$ (c).

26

27

Figure 2.10: Variation of $K_p(r_p)$, defined in Eq.(2.17), along nozzle axis for $\nu = 1.0$ (a), $\nu = 3.0$ (b) and $\nu = 5.0$ (c) (i:size number).
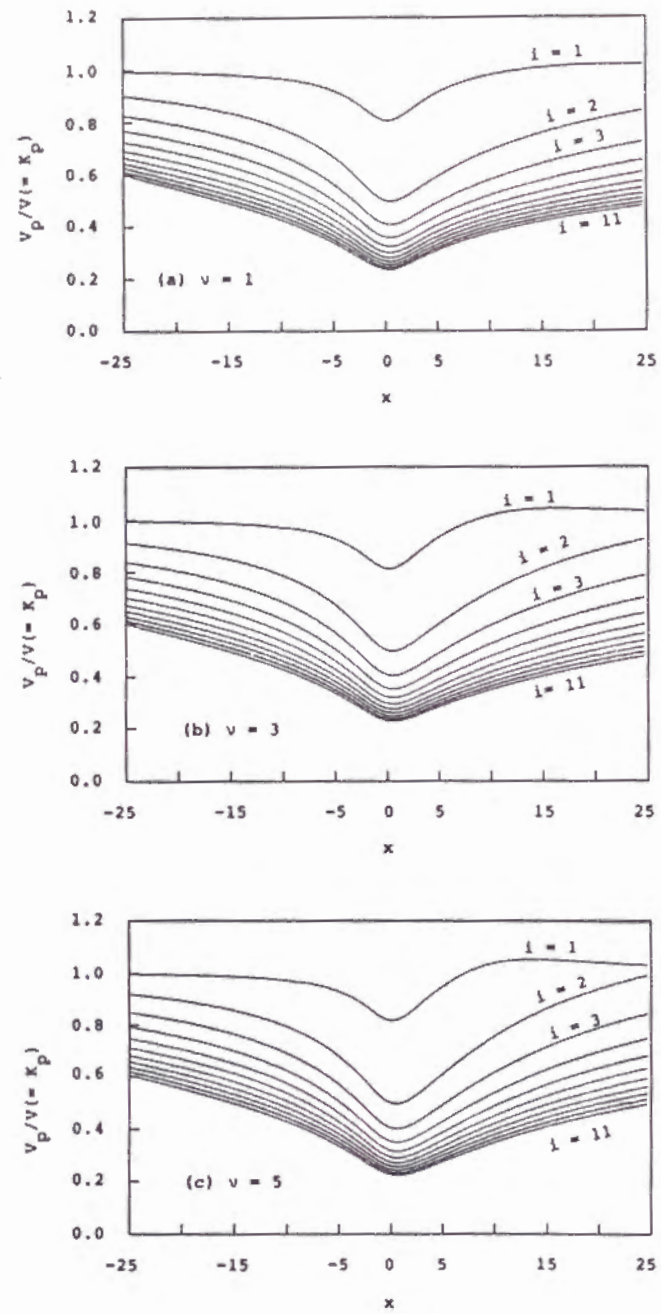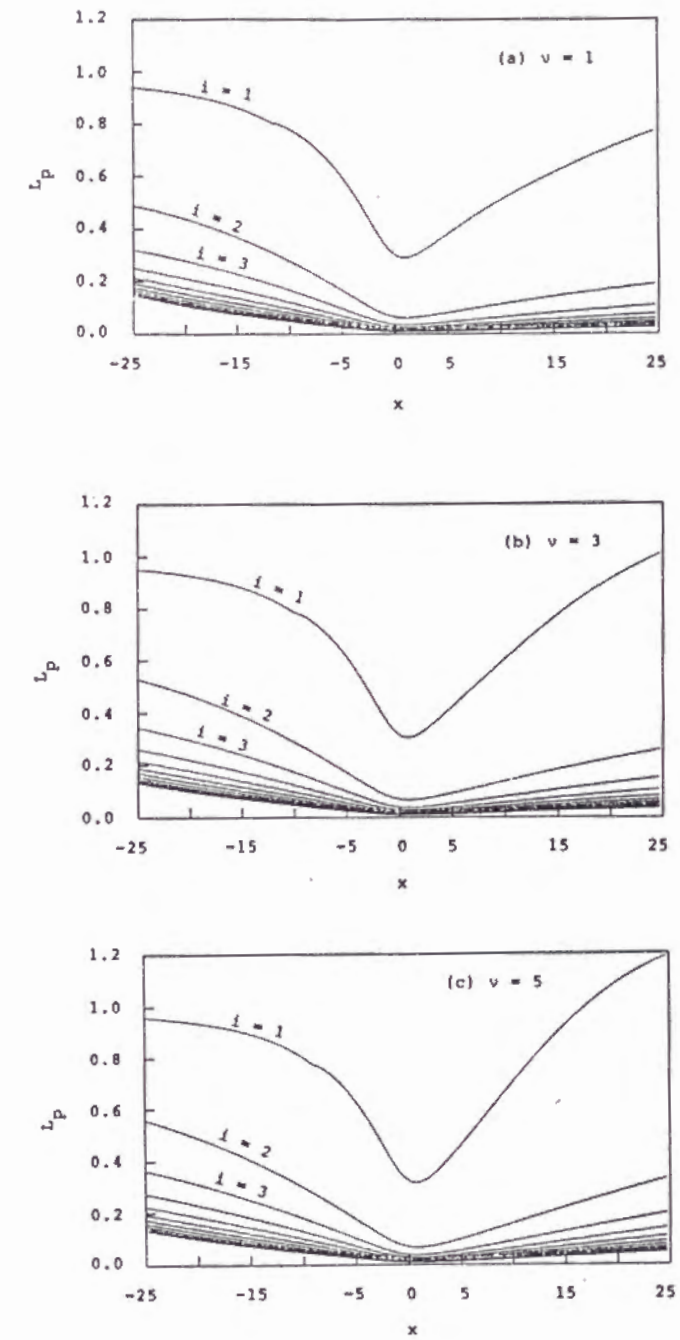

Figure 2.11: Variation of $L_p(r_p)$, defined in Eq.(2.17), along nozzle axis for $\nu = 1.0$ (a), $\nu = 3.0$ (b) and $\nu = 5.0$ (c) (i:size number).
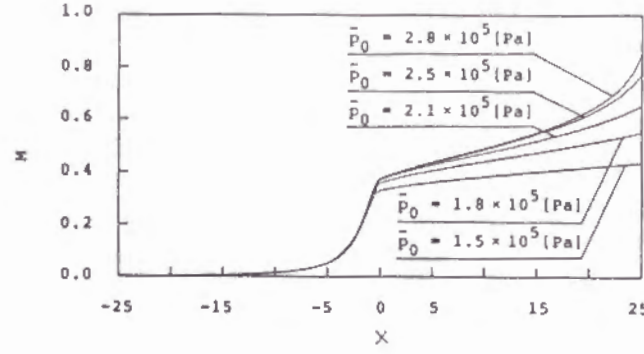
Figure 2.12: Variation of local gas-phase Mach number along nozzle axis with p_0 as a parameter ($\bar{p}_e = 1.0 \times 10^5$ [Pa] and $\nu = 3$). Note that the nozzle geometry given by Eq.(2.30) is adopted in this calculation

$$\nu = \frac{\dot{\bar{M}}_p}{\dot{\bar{M}}_g} = \frac{\bar{R}_p}{\bar{\rho}} = \frac{\bar{R}_{p0}}{\bar{\rho}_0} = \nu_0 \tag{2.32}$$

It is clear, comparing the above relation with Eq.(2.16), that $\dot{M}_p = \dot{M}_g$. That is, the mass flow rate of the particle-phase is equal to that of the gas-phase in the dimensionless space. It can be said that this is true also for the subsonic nozzle flow. However, it does not hold true that $\dot{\bar{M}}_g = \dot{\bar{M}}_p$ in the dimensional space.

Again, it should be noted that $\dot{M}_p$ decreases in ν. In the present numerical experiments $\dot{M}_p=0.49908$ at $\nu = 1$, $\dot{M}_p=0.40702$ at $\nu = 3$ and $\dot{M}_p=0.35271$ at $\nu=5$ for the supersonic nozzle flow. From Eq.(2.15), we have,

$$\dot{\bar{M}}_g = \dot{M}_g \bar{p}_0 \bar{A}_*(\gamma/\bar{R}\bar{T}_0)^{1/2} \quad \text{and} \quad \dot{\bar{M}}_p = \nu \dot{\bar{M}}_g \tag{2.33}$$

where $\bar{R}$ is the gas constant. Thus, $\dot{\bar{M}}_p = 6.09 \times 10^{-3}$ [kg/s] at $\nu = 1$, $\dot{\bar{M}}_p=0.0149$ [kg/s] at $\nu = 3$ and $\dot{\bar{M}}_p=0.0215$ [kg/s] at $\nu = 5$. In passing, for the above subsonic nozzle flow, $\dot{M}_p=0.42593$ at $\nu = 1$, $\dot{M}_p=0.31366$ at $\nu = 3$ and $\dot{M}_p=0.25894$ at $\nu = 5$. Again, $\dot{\bar{M}}_p = 9.36 \times 10^{-4}$ [kg/s] at $\nu = 1$, $\dot{\bar{M}}_p = 2.06 \times 10^{-3}$ [kg/s] at $\nu = 3$ and $\dot{\bar{M}}_p = 2.86 \times 10^{-3}$ [kg/s] at $\nu = 5$.

Finally, the position where $p = 0.994$ has been regarded as the end point of the equilibrium region. Therefore, we should be like to emphasize that the perturbation between the equilibrium and the non-equilibrium flows has been made at the above position for the supersonic nozzle flow.

2.6 Conclusion

We have constructed a system of equations governing the nozzle flow of gas-particle mixture to evaluate all of the flow properties in the flow field. It has been stressed that the equation to determine the gas-phase velocity plays an important role from the point of view of the numerical treatment. Eq.(2.9) is clearly singular in the transonic region.

Therefore, for the subsonic nozzle flow, all of the flow properties have been calculated on the basis of the nozzle geometry with the parallel region by the specified area method. What is remarkable is that the flow properties vary even in the parallel region for the case $\nu \neq 0$, while for $\nu = 0$, the pressure, temperature and velocity of the gas-phase remain unvaried in the parallel region.

Next, for the supersonic nozzle flow, the specified pressure method has been employed by a pressure profile given along the nozzle axis. All of the flow properties in the whole region from the subsonic flow to the supersonic flow have been obtained in accord with the given pressure profile. Again, it has been demonstrated that the nozzle configuration can be designed according to the desired pressure profile.

In conclusion, we note that the theoretical procedure mentioned here has the attractive aspect whereby the nozzle flow of the gas-particle mixture can be exactly understood from a numerical point of view.

Reference

1. Kliegel, J. R., 9th Int. Symp. on Combustion, Academic press, New York,(1963), p.811.

2. Chang, I. S., AIAA J., 18(1980), p.1455.

3. Ishii, R. and Umeda, Y., Phys. Fluids, 30(1980), p.752.

4. Zucrow, M. J. and Hoffman, J. D.,"Gas-dynamics II", John Wiely and Sons, New York,(1977).

5. Hatta, N., Ishii, R., Takuda, H., Ueda, K. and Kokado, J., Trans. ISIJ, 28(1988), p.930.

6. Hatta, N., Takuda, H., Ishii, R. and Fujimoto, H., ISIJ Int., 29(1989), p.605.

7. Henderson, C. B., AIAA J., 14(1976), p.707.

8. Carlson, D. J. and Hoglund, R. F., AIAA J., 2(1964), p.1980.

9. Hatta, N., Fujimoto, H., Ishii, R., Umeda, Y. and Kokado, J., ISIJ Int., 29(1989), p.911.

10. Hatta, N., Kokado, J., Ishii, R. and Fujimoto, H., Mem. Fac. Engg. Kyoto Univ., 51-2(1989), p.73.

Chapter 3

Numerical analysis of gas-particle two-phase subsonic freejets

[18]

3.1 Introduction

Gas-particle flows are used in a wide range of various industrial applications such as cyclone separators and classifiers, pneumatic conveying of powder, spray drying and cooling, as well as mist cooling, which is commonly applied to the secondary cooling zone in the continuous casting process of slabs. For analyzing gas-particle flow through a nozzle, a number of models have been developed. We also have extended the quasi-one-dimensional flow model which was described by Zucrow and Hoffman[1] to the case where the continuous distribution of particle size is present, and we have nearly established the analytical procedure to evaluate all of the flow properties for both gas and particle phases in a nozzle [2-4].

Gas-particle flows are characterized by coupling between phases. The thermal coupling through heat transfer from the gas-phase to the particle-phase and the momentum coupling through aerodynamic drag responsible for particle motion must be incorporated in the numerical flow model.

Next, as discussed by Crowe[5], the flow of gas-particle mixture can be categorized according to the significance of particle-particle collisions on particle motion. A flow in which particle motion is controlled by collisions is a dense flow. A flow in whcih particle motion is controlled by the aerodynamic forces on the particle is regarded as a dilute flow. The delineation between dilute and dense flow is qualitatively established by the ratio of the aerodynamic response time $\bar{\tau}_A$ to the time between collisions $\bar{\tau}_C$. If $\bar{\tau}_A/\tau_C < 1$, a particle has time to respond to the local gas velocity field before the next collision so its motion is dominated by aerodynamic forces. In such case, the flow can be regarded as a dilute one. Also, Ishii et al. [6] have quantitatively given the criterion for the diluteness of gas-particle suspensions from a little different angle. They state that the except some extreme situations particle-particle collisions can be neglected if the particle mass loading ratio ν is $O(1)$ and hence the particle volume fraction ϵ_p is $O(10^{-3})$. The effect of collisions

is neglected in the present numerical model, because the mixture composed of air and water-droplet will be treated in an allowable range of ν.

This chapter is concerned with a numerical analysis of subsonic gas-particle free jets exhausted from a round nozzle into a quiescent gas. Therefore, a system of equations governing the nonequilibrium, steady and quasi-one-dimensional nozzle flow of gas-particle mixture is numerically solved from a reservoir to a nozzle exit, and then all of the flow properties at the nozzle exit are applied to the boundary condition of two-phase free jets. The numerical model for gas-particle flows is constructed by incorporating the particle trajectory method[7,8] into the system of gas-phase equations in the so-called two-fluid model[9]. The particle clouds are divided into a large number of small subclouds according to Ishii et al.[6]. In each subcloud, the particles are approximated to have the same velocity and temperature. The particle flow field is solved by following the behavior of all the subclouds in the flow field. The axisymmetric Navier-Stokes equations for the gas-phase interacting with the particle-phase are solved using the Stokes hypothesis. In estimating the momentum and energy transfer rates between gas and particle phases, the contributions from the clouds to the gas-phase are averaged in a computational cell with an appropriate cross-sectional area. The present calculations are performed with a single particle size. Three cases are treated where $\bar{r}_p = 0.5\mu m, 2.5\mu m$ and $15\mu m$, respectively, where $\bar{r}_p$ denotes the radius of droplet. Again, the mass loading ratio is taken to be $\nu_0 = 0.3$ in a reservoir for any case.

3.2 Governing Equations

The flow model for gas-particle mixtures is built up on several usual assumptions as follows;

(1) Particles are spherical water-droplets with a uniform diameter and a constant specific heat.

(2) Particles occupy negligible volume and are discrete, so that particle-particle collision, agglomeration and/or decomposition of the particles are neglected, as mentioned already.

(3) Gas-particle interaction occurs through aerodynamic drag responsible for particle motion.

(4) Energy exchange between particles and gas occurs only through convection.

(5) Particles have a uniform internal temperature.

(6) No phase transformation takes place.

(7) Effects of gravity and fluid turbulence are neglected.

The equations governing the two-phase flow are described by introducing the following nondimensional quantities:

$$t = \frac{\bar{t}}{\bar{L}/\bar{c}_0}, \quad x = \frac{\bar{x}}{\bar{L}}, \quad y = \frac{\bar{y}}{\bar{L}}, \quad \rho = \frac{\bar{\rho}}{\bar{\rho}_0}, \quad p = \frac{\bar{p}}{\bar{p}_0},$$

$$u = \frac{\bar{u}}{\bar{c}_0}, \quad v = \frac{\bar{v}}{\bar{c}_0}, \quad T = \frac{\bar{T}}{\bar{T}_0}, \quad c = \frac{\bar{c}}{\bar{c}_0}, \tag{3.1}$$

$$x_p = \frac{\bar{x}_p}{\bar{L}}, \quad y_p = \frac{\bar{y}_p}{\bar{L}}, \quad u_p = \frac{\bar{u}_p}{\bar{c}_0}, \quad v_p = \frac{\bar{v}_p}{\bar{c}_0}, \quad T_p = \frac{\bar{T}_p}{\bar{T}_0}$$

where t, x, y are the time, axial distance and radial distance, respectively; ρ, p, u, v, T and c are the density, pressure, axial velocity, radial velocity, temperature and speed of sound of the gas, respectively. $\bar{L}$ is a characteristic length of the flow field and the nozzle radius at the exit is taken as $\bar{L}$. The subscripts 0 and p denote the reference condition and particles, respectively, and overbars denote the dimensional quantities.

3.2.1 Particle-phase

A discrete particle-cloud model[6] is applied to solve the particle-phase. In this model, a whole particle cloud is divided into a large number of small subclouds. The particle flow field is obtained by following these individual subclouds separately in the whole flow domain.

By labelling the particle subclouds subscripts $k (k = 1, 2, 3, \ldots)$ and denoting the velocity components and temperature of a particle located at $(x_{pk}(t), y_{pk}(t))$ by $(u_{pk}(t), v_{pk}(t))$ and $T_{pk}(t)$, respectively, the momentum and energy equations the k-th particle subcloud are expressed by

$$\frac{d\mathbf{E}_{pk}}{dt} = \mathbf{I}_{pk} \tag{3.2}$$

in which

$$\mathbf{E}_p = \begin{bmatrix} x_p \\ y_p \\ u_p \\ v_p \\ T_p \end{bmatrix}, \qquad \mathbf{I}_p = \begin{bmatrix} u_p \\ v_p \\ A_p(u - u_p) \\ A_p(v - v_p) \\ B_p(T - T_p) \end{bmatrix} \tag{3.3}$$

The parameters A_p and B_p are defined by

$$A_p = \frac{f_p}{\Gamma_\tau}, \qquad B_p = \frac{2g_p}{3\Gamma_\tau Pr\theta} \tag{3.4}$$

in which

$$f_p = \frac{C_D}{C_{D,Stokes}}, \qquad g_p = \frac{Nu}{Nu_{Stokes}} \tag{3.5}$$

$$\Gamma_\tau = \frac{\bar{\tau}_A}{\bar{\tau}_F}, \qquad \theta = \frac{\bar{C}_{pp}}{\bar{C}_{pg}}, \qquad \gamma = \frac{\bar{C}_{pg}}{\bar{C}_{vg}} \tag{3.6}$$

Again, $\bar{C}_{vg}$ and $\bar{C}_{pg}$ are the specific heats at constant volume and pressure of the gas, $\bar{C}_{pp}$ is the specific heat of the particle material. γ is the specific heat ratio of the gas. C_D is the particle drag coefficient and Nu is the Nusselt number. The subscript $Stokes$ denotes the Stokes flow regime. Also, $\bar{\tau}_A$ and $\bar{\tau}_F$ are defined by

$$\bar{\tau}_A = \frac{\bar{\rho}_{mp}(2\bar{r}_p)^2}{18\bar{\mu}}, \qquad \bar{\tau}_F = \frac{\bar{L}}{\bar{c}_0} \tag{3.7}$$

Here, $\bar{\rho}_{mp}$ is the material density of the particles, and $\bar{\mu}$ is the gas viscosity given by

$$\bar{\mu} = \bar{\mu}_0 T^\delta \tag{3.8}$$

where δ is an appropriate constant. Again, the following non-dimensional properties,

$$\mu = \frac{\bar{\mu}}{\bar{\mu}_0}, \quad \lambda = \frac{\bar{\lambda}}{\bar{\lambda}_0} = 1 + \bar{\beta}(\bar{T} - \bar{T}_0) \tag{3.9}$$

are introduced, where λ is the thermal conductivity of the gas.

C_D and Nu used in the present study are those given by Henderson[10] and Carlson & Hoglund [11], respectively. This sphere-drag coefficient accounts for rarefaction, inertial and compressibility effects and also that of a temperature difference between the particle and the gas. In addition, virtual mass force, pressure gradient force, and Basset force are all neglected. An order of magnitude study based upon the equation of motion given by Maxey and Reily[12] reveals that virtual mass and pressure gradient are of the order of $\bar{\rho}/\bar{\rho}_{mp}$, and Basset force is of order of $(\bar{\rho}/\bar{\rho}_{mp})^{1/2}$. Since $(\bar{\rho}/\bar{\rho}_{mp})$ is of order of 10^{-3} for a typical gas-water droplet flow system in this study, the neglect of those forces may be justified.

For an axisymmetric flow system, the particle cloud in the physical space forms a ring cloud. Denoting the number of particle contained in the k-th cloud per unit depth by $N_{pk} = (\bar{N}_{pk}/\bar{n}_{pE}/\bar{L}^2)$, where $\bar{n}_{pE}$ is the number density at the nozzle exit, the number of particles in the subcloud can be given by $2\pi y_{pk} N_{pk}$. Thus, we have

$$N_{pk} = (y_{pk}^*/y_{pk})N_{pk}^* \tag{3.10}$$

where the asterisk denotes the conditions of particles at the nozzle exit.

3.2.2 Gas-phase

Introducing the Stokes hypothesis, the system of the axisymmetric Navier-Stokes equation for the gas-phase interacting with the particle-phase is given by

$$\frac{\partial \mathbf{Q}}{\partial t} + \frac{\partial \mathbf{F}_1}{\partial x} + \frac{\partial \mathbf{F}_2}{\partial y} + \frac{\partial \mathbf{G}_1}{\partial x} + \frac{\partial \mathbf{G}_2}{\partial y} + \frac{1}{y}\mathbf{H} + \mathbf{H}_p = 0 \tag{3.11}$$

in which

$$
\mathbf{Q} = \begin{bmatrix} \rho \\ \rho u \\ \rho v \\ e \end{bmatrix}, \mathbf{F}_1 = \begin{bmatrix} \rho u \\ \rho u^2 + p/\gamma \\ \rho uv \\ u(e + p/\gamma) \end{bmatrix}, \mathbf{F}_2 = \begin{bmatrix} \rho v \\ \rho uv \\ \rho v^2 + p/\gamma \\ v(e + p/\gamma) \end{bmatrix},
$$

$$
\mathbf{G}_1 = \frac{1}{Re_0} \begin{bmatrix} 0 \\ f_x \\ -\tau \\ uf_x - v\tau - \frac{1}{(\gamma-1)Pr_0}\lambda\frac{\partial T}{\partial x} \end{bmatrix},
$$

$$
\mathbf{G}_2 = \frac{1}{Re_0} \begin{bmatrix} 0 \\ -\tau \\ f_y \\ vf_y - u\tau - \frac{1}{(\gamma-1)Pr_0}\lambda\frac{\partial T}{\partial y} \end{bmatrix},
$$

$$
\mathbf{H} = \begin{bmatrix} \rho v \\ \rho uv - \tau/Re_0 \\ \rho v^2 - \alpha/Re_0 \\ v(e+p)/\gamma + \left[vf_y - u\tau - \frac{1}{(\gamma-1)Pr_0}\lambda\frac{\partial T}{\partial y}\right]/Re_0 \end{bmatrix},
$$

$$
\mathbf{H}_p = \begin{bmatrix} 0 \\ F_{px} \\ F_{py} \\ \dot{Q}_p + \dot{W}_p \end{bmatrix} \tag{3.12}
$$

with

$$
\left.\begin{aligned}
f_x &= \frac{2}{3}\mu\left(\frac{\partial v}{\partial y} + \frac{v}{y} - 2\frac{\partial u}{\partial x}\right), \\
f_y &= \frac{2}{3}\mu\left(\frac{\partial u}{\partial x} + \frac{v}{y} - 2\frac{\partial v}{\partial y}\right), \\
\tau &= \mu\left(\frac{\partial v}{\partial x} + \frac{\partial u}{\partial y}\right), \\
\alpha &= 2\mu\left(\frac{\partial v}{\partial y} - \frac{v}{y}\right), \\
Pr_0 &= \frac{\bar{C}_{pg}\bar{\mu}_0}{\lambda}, Re_0 = \frac{\bar{L}\bar{c}_0\bar{\rho}_0}{\bar{\mu}_0}
\end{aligned}\right\} \tag{3.13}
$$

Furthermore, $F_{px}, F_{py}, \dot{Q}_p$ and $\dot{W}_p$ are expressed by

$$
\left.\begin{aligned}
F_{px} &= \frac{\nu_E}{S_p}\sum N_{pk}A_{pk}(u - u_{pk}) \\
F_{py} &= \frac{\nu_E}{S_p}\sum N_{pk}A_{pk}(v - v_{pk}) \\
\dot{Q}_p &= \frac{\nu_E}{S_p}\sum N_{pk}B_{pk}\frac{\theta}{\gamma-1}(T - T_{pk}) \\
\dot{W}_p &= F_{px}u + F_{py}v - \frac{\nu_E}{S_p}\sum N_{pk}A_{pk}\left\{(u - u_{pk})^2 + (v - v_{pk})^2\right\}
\end{aligned}\right\} \tag{3.14}
$$

in which

$$
S_p = \frac{\bar{S}_p}{\bar{L}^2}, \quad N_p = \frac{\bar{N}_p}{\bar{n}_{pE}\bar{L}^2}, \quad \nu_E = \frac{\bar{n}_{pE}\bar{m}_p}{\bar{\rho}_E} \tag{3.15}
$$

Table 3.1: Physical parameters for gas and droplets adopted.

Gas(Air)	Particle(Water droplet)
$\gamma = 1.4$	$\bar{C}_{pp} = 4187$ J/kg·K
$\bar{C}_{pg} = 1009$ J/kg·K	$\bar{\rho}_{mp} = 1000$ kg/m^3
$\bar{\nu}_0 = 2.0 \times 10^{-5}$ Pa·s	
$\bar{\lambda}_0 = 0.028$ W/m·K	
$\delta = 0.76$ (see Eq.(3.8))	
$\bar{\beta} = 2.68 \times 10^{-3}$ K^{-1} (see Eq.(3.9))	
Pr=0.71	

Here, the summation including in Eq.(3.14) is taken over the cloud whose centers (x_{pk}, y_{pk}) are in the computational cell with the sectional area $S_p(= \Delta x \cdot \Delta y)$. The subscript E denotes the nozzle exit condition. Also, $\bar{n}_p$ is the number density and $\bar{m}_p = (4/3)\pi\bar{r}_p^3\bar{\rho}_{mp}$.

In addition, the total energy per unit volume of the gas e and the sound of speed c are given by

$$
e = \frac{p}{\gamma(\gamma - 1)} + \frac{1}{2}\rho(u^2 + v^2) \qquad (p = \rho T) \tag{3.16}
$$

$$
c = T^{1/2} \tag{3.17}
$$

3.3 Numerical Procedure and Computational Condition

Flow fields of gas-particle two-phase subsonic free jets are solved as a perturbation from the nozzle exit condition. Therefore, the system of equations governing the gas-particle mixture flow in a nozzle [2] is numerically solved for determining the nozzle exit condition.

The gas-particle mixture composed of air and water-droplets of a single size is treated. Three cases are considered where $\bar{r}_p = 0.5\mu m, 2.5\mu m$ and $15\mu m$, respectively. The mass loading ratio is assumed to be $\nu_0 = 0.3$ in a reservoir for any case.

The nozzle geometry is given by $A = (x + 5)^2 + 1$ for $x \le -5$ and $A = 1$ for $-5 < x \le 0$, where A denotes the sectional area of the nozzle. It is noted that the nozzle exit at $x = 0$ corresponds to the origin of the jet axis. The nozzle radius in the constant area region is set to be $\bar{L} = \bar{D}/2 = 5 \times 10^{-3}$m.

The reservoir condition is that $\bar{p}_0 = 1.8 \times 10^5$ Pa and $\bar{T}_0 = 323$K. The ambient gas condition is that $\bar{p}_\infty = 1.0 \times 10^5$ Pa and $\bar{T}_\infty = 300$ K. Thus, the initial gas condition is that $p = 0.556$, $T = 0.929$ and $u = v = 0$ over the whole computational domain. Physical constants of the gas and particles used here are listed in Table 3.1.

The numerical flow properties at the nozzle exit are shown in Table 3.2. It is noted that $v_E = 0$ and $p_E = 0.556$ for all $\bar{r}_p$. The numerical results at $x = 0$ are applied to the jet boundary condition at the origin of the free jet region.
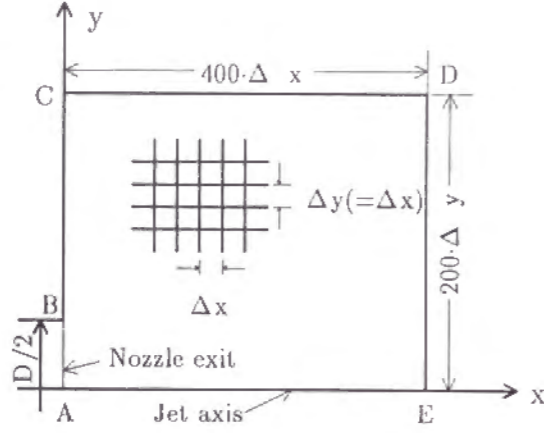
Figure 3.1: Geometry of computational domain.

The equations for the gas-phase consist of the inviscid terms, the viscous terms, the axisymmetric term and the interaction term by the presence of particle-phase. The inviscid terms are solved by using a TVD(Total Variation Diminishing) scheme by Chakravarthy and Osher [13] and the other terms are solved by using the central differencing scheme. Therefore, the computational domain is divided into a number of small cells and the physical variables are defined at the cell center. Also, the physical variables at interface between two neighboring cells are calculated by the Roe approach [14].

Figure 3.1 indicates the geometry of the computational domain. The domain size corresponds to $10\bar{D}$ in the axial direction and $5\bar{D}$ in the radial direction in a half section. Here, the computational domain is divided into 400×200 cells in the $x-$ and $y-$directions, respectively.

We wish briefly mention the boundary condition of the computational domain. The ambient gas condition is imposed to the upstream boundary BC, the side one CD and the downstream boundary DE, the symmetric condition is done to the jet axis, AE, and the jet condition is applied to the jet exit plane AB [15].

Here, we consider the effect of selecting the cell size, $\Delta x(=\Delta y)$, on the numerical accuracy. Δx is determined by dividing the nozzle radius in n equal parts. For various n values, the numerical experiments have been performed for single-phase(gas-only) flows. The results have been compared with each other. Figure 3.2(a) indicates the calculated

Table 3.2: Numerical flow properties at nozzle exit for $\bar{r}_p = 0.5\mu m, 2.5\mu m$ and $15\mu m$, respectively.

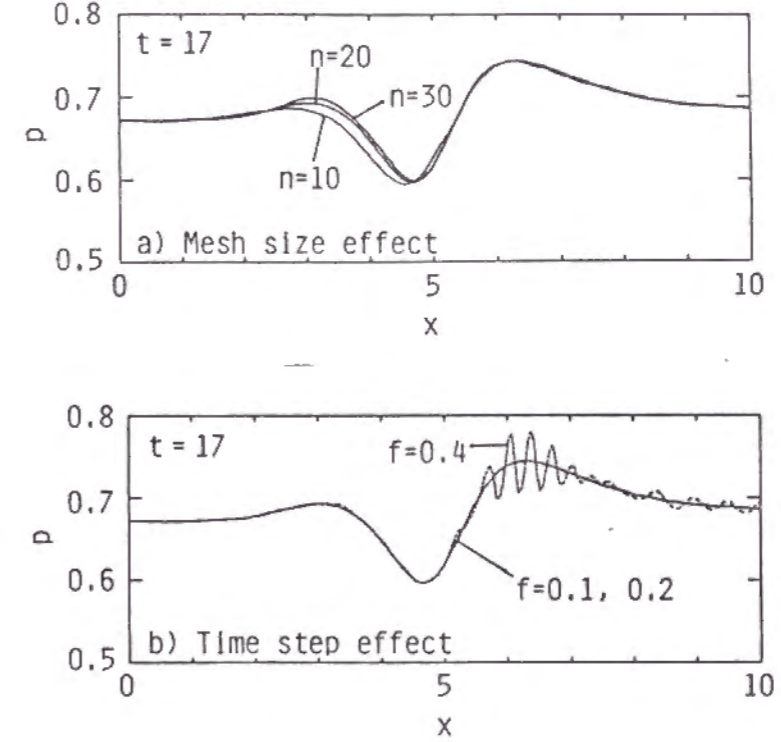| $\bar{r}_p(\mu m)$	u_E	T_E	u_{pE}	v_{pE}
0.5	0.783	0.928	0.780	0.930
2.5	0.775	0.903	0.706	0.957
15.0	0.799	0.874	0.452	0.989

Figure 3.2: Preliminary check on effects of mesh size (a) and computational time step (b) on numerical accuracy. Note that for the check of the numerical accuracy, the pressure distribution of gas-only jet flow in an axial direction is taken for example, and that computations shown in Fig.3.2(a) are performed on the CFL number, $f=0.2$. Also, $n=30,20$ and 10 correspond to $\Delta x = 1/3, 1/20$, and $1/10$, respectively.

pressure distributions along $y=0.05$ at $t=17$ for $n=10,20$ and 30,respectively. We wish to add that the value of $n=20$ is corrected by the Roe approach. The numerical error is at most 3.8 percent between $n=10$ and 30. Accordingly, $\Delta x=0.05$, corresponding to $n=20$, is selected in the present simulation.

Next we consider the effect of computational time interval, Δt, on the numerical accuracy. Δt is determined by the CFL(Courant-Friedrichs-Levy) condition for the gas-phase flow [16]. The numerical results obtained by various CFL numbers have been compared with each other. Figure 3.2(b) indicates the pressure distributions along the x-axis(precisely, $y=0.025$) at $t=17$ for $f=0.1,0.2$ and 0.4, respectively, where f is the CFL number. The numerical result of $f=0.4$ is observed to be oscillatory downstream. No significant difference is recognized between $f=0.1$ and 0.2. Therefore, we have selected $f=0.2$ throughout the present simulations. Also, we have found that Δt determined by this f is always much smaller than two kinds of characteristic non-dimensional times for the particle phase $\tau_{pv}(= A_p^{-1})$ and $\tau_{pT}(= B_p^{-1})$. Therefore, this Δt is also used for the

particle-phase solution.

For the purpose of obtaining the time-converged two-phase flow structure, the numerical results at a sufficiently large number of time steps are required owing to using an explicit time-dependent difference scheme. In the present calculation, the gas-only flow field is solved for the first 10000 time steps, and then two-phase flow field is solved for the next 15000 time steps so that the time-converged solutions may be found in as a short computational time as possible.

3.4 Numerical results

In this section, the behavior of particles in the gas flow is demonstrated in detail. The particles are exhausted at $y^*_{pk} = (k - 0.5)/30$ $(k = 1 \sim 30)$ on the nozzle exit plane at every time interval Δt.

Figures 3.3(a) to 3.3(c) give the center locations of particle subclouds along streaklines in the mixture jet flow for $\bar{r}_p$=0.5, 2.5 and 15μm, respectively. It is noted that the particles in these figures are limited to only those exhausted at every 20 time steps. From these figures some significant and interesting features will be pointed out. The fluctuating scale in particle motion may be considered to depend upon the particle size. We notice, at a glance, from these figures that for smaller particles ($\bar{r}_p = 0.5\mu m$), the fluctuation of the particle motion begins to occur in a relatively downstream region. This may be based upon the fact that the gas-phase continues to maintain more momentum to a relatively large distance in the axial direction, because the velocity and temperature of the particle-phase with $\bar{r}_p = 0.5\mu m$ at the nozzle exit are very similar to those of the gas-phase. On the other hand, for larger particles, the difference in velocity and temperature between the gas and particle phases becomes larger at the nozzle exit, and therefore the fluctuation of the particle motion begins to occur considerably upstream.

Figures 3.4(a) to 3.4(c) show the contours of equal vorticity $\zeta (= \partial v/\partial x - \partial u/\partial y)$ for $\bar{r}_p$=0.5, 2.5 and 15 μm, respectively. We find that vortical structures occur due to the velocity difference between the main jet flow and the ambient gas at the jet boundary(Kelvin-Helmholtz instability). Comparing Figs. 3.3(a) to 3.3(c) with Figs. 3.4(a) to 3.4(c) for the corresponding particle radius at the same time, we can find that the region with relatively large vorticity roughly corresponds to the particle-free-region. Chung and Troutt[17] state that particles tend to move away from the core of larger-vortex structures. The present numerical results are quite consistent with their results. One of the most important features to be noted in the present simulation is that a perfectly time-converged(steady) solution, in the conventional sense, can not be reached, even at $t \to \infty$. However, the global flow structure of the gas-particle mixture jet does not change with time. Rather, the vortical structures occur at the nozzle exit somewhat periodically. The vortices are convected downstream and agitate the jet boundary. That is, when a vortical structure is convected some distance downstream, another new vortex is produced at the nozzle exit. Thus process is repeatedly continued.

Figures 3.5(a) to 3.5(c) give the pressure distributions along the jet axis (strictly, $y = 0.025$) for $\bar{r}_p = 0.5, 2.5$ and 15μm, respectively. It can be seen that pressure becomes almost constant upstream and fluctuates downstream, and that the position where
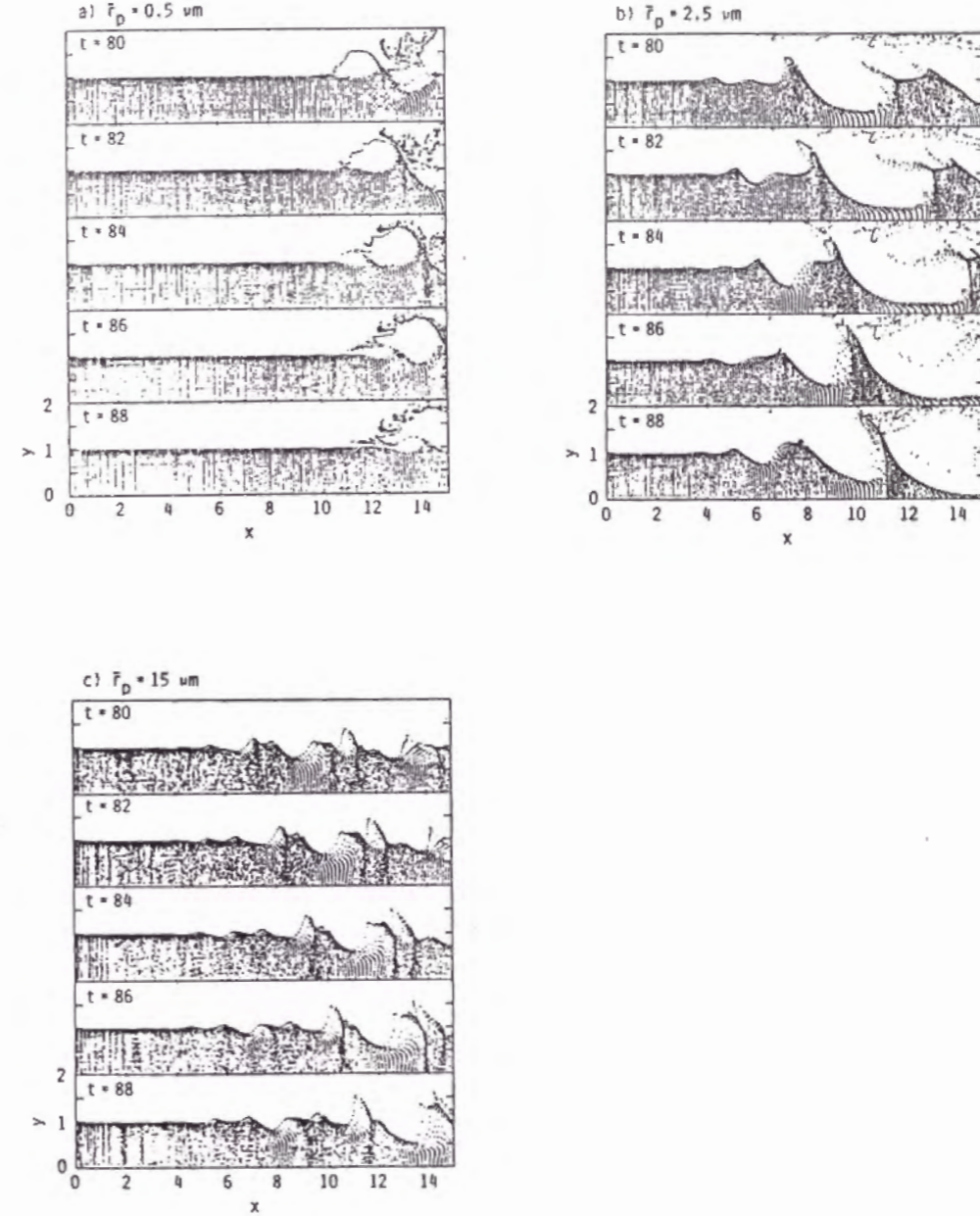

Figure 3.3: Locations of centers of particle subclouds along streaklines for $\bar{r}_p = 0.5\mu m$(a), $2.5\mu m$(b) and $15\mu m$(c).
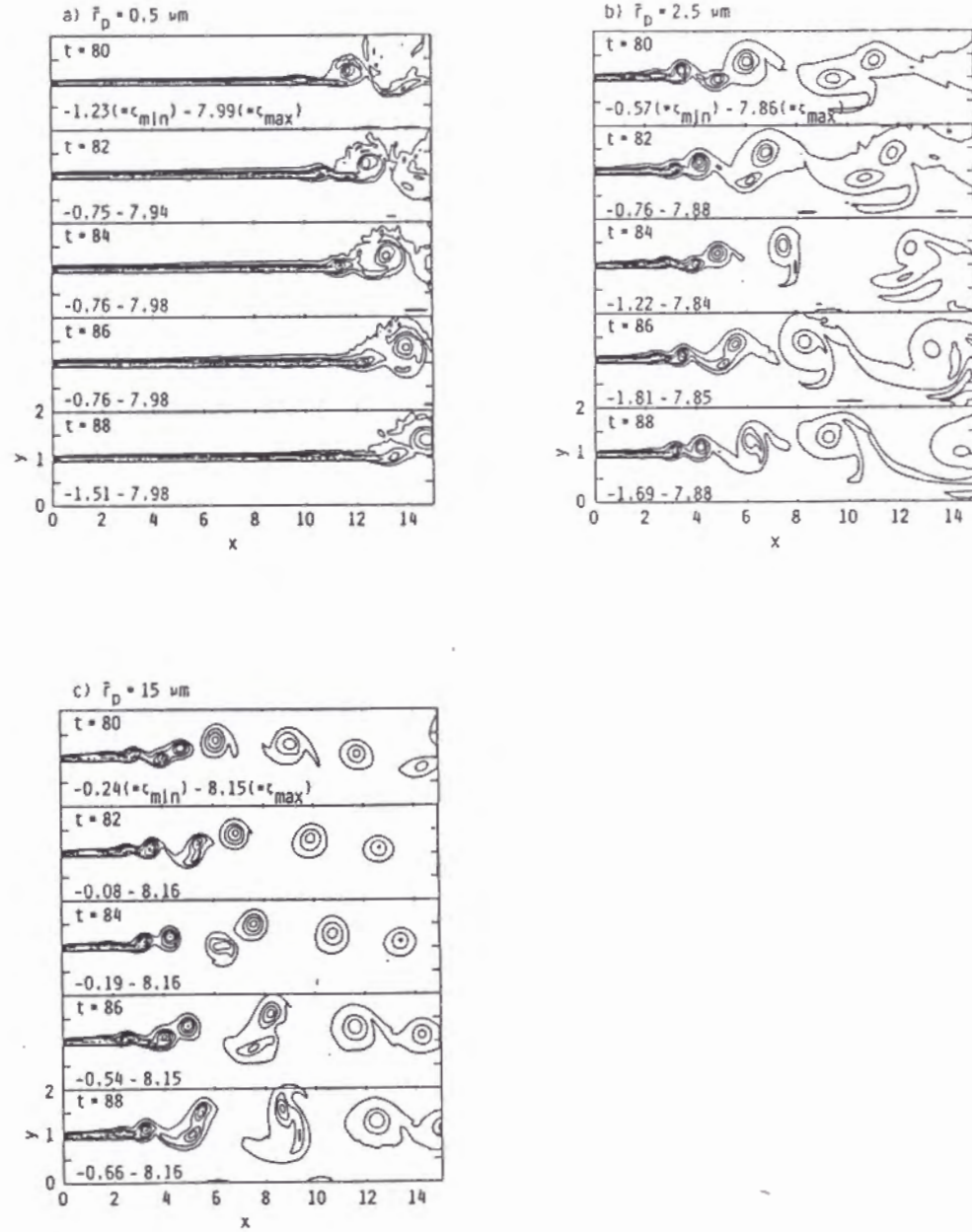
a) $\bar{r}_p = 0.5\ \mu m$

b) $\bar{r}_p = 2.5\ \mu m$

c) $\bar{r}_p = 15\ \mu m$

Figure 3.4: Contours of equal vorticity ζ of gas flow. Note that these contours are drawn by dividing the difference between the maximum and minimum values(ζ_{max} and ζ_{min}) into 10 equal parts.
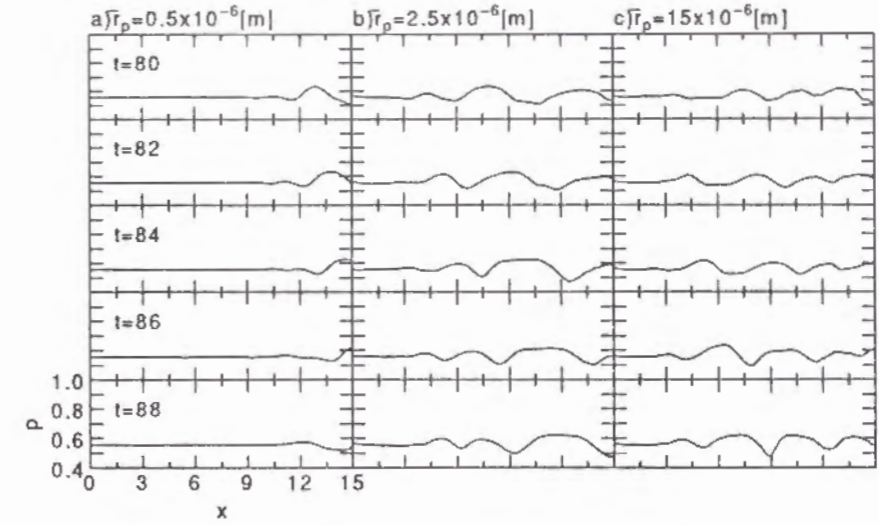

Figure 3.5: Distributions of gas pressure along jet axis.

pressure begins to change depends on the particle radius. The wavelength of pressure variation seems to be equal to $2\bar{D}$ or so. One of the most interesting features is that the low-pressure locations along the jet axis agree roughly with the x-coordinate of those with the larger vorticity(see Fig. 3.4), where the radial distance of outermost particle stream becomes smaller (see Fig. 3.3).

Figures 3.6(a) to 3.6(c) indicate the velocity distributions for the gas and particle phases along the jet axis. Here, the gas and particle phase velocities indicate $V = (u^2 + v^2)^{1/2}$ and $V_p = (u_p^2 + v_p^2)^{1/2}$, respectively. The behavior for both V and V_p is seen to be widely different depending on the particle size. V_p for smaller particles ($\bar{r}_p = 0.5 \mu m$) almost perfectly responds to the velocity fluctuation of the gas flow. However, for $\bar{r}_p = 15 \mu m$, the particles do not have sufficient time to respond to the changing velocity field of the gas-phase. The particles of $\bar{r}_p = 2.5 \mu m$ reveal the intermediate velocity response between the cases of $\bar{r}_p = 0.5 \mu m$ and 15 μm.

Figures 3.7(a) to 3.7(c) show the temperature distributions for the gas and particle phases along the jet axis. The particle temperature T_p for a larger size ($\bar{r}_p > 2.5 \mu m$) is almost constant regardless of a considerably large temperature fluctuation of gas-phase. This may be considered to be due to the effect of the thermal inertia. On the other hand, the behavior of T_p for smaller particles($\bar{r}_p = 0.5 \mu m$) is analogous to that of V_p and roughly responds even to the small temperature fluctuation of gas-phase. It may be concluded that the flow structure of two-phase mixtures containing particles smaller than $\bar{r}_p = 0.5 \mu m$ is approximately in velocity and thermal equilibrium between the two phases. That is, the transfer rate for both momentum and energy between the gas and particle phases is extremely sensitive for the case of smaller particles.

Figures 3.8(a) to 3.8(c) give variations in gas-phase pressure with time at five fixed positions($\bar{x} = j\bar{D}; j = 1 \sim 5$) along the jet axis from $t=50$ to $t=90$. It can be seen from these figures that the pressure variation with time occurs negligibly slightly upstream
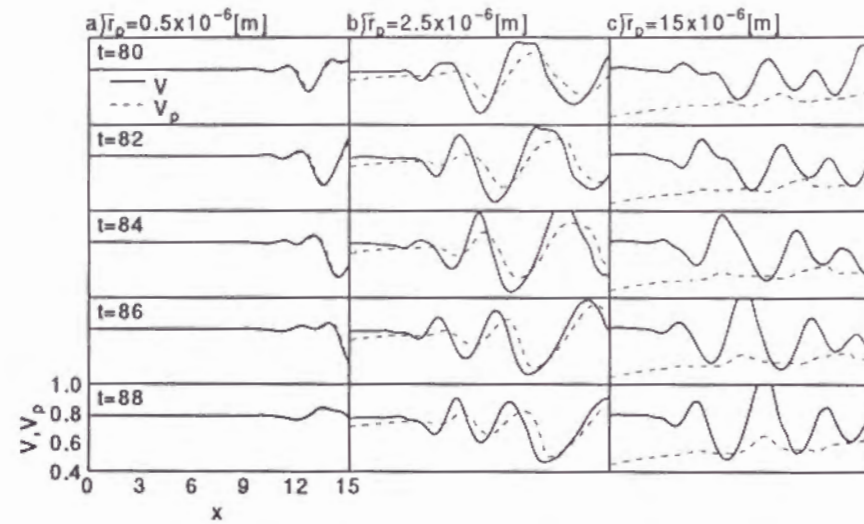
Figure 3.6: Distributions of gas-particle velocity V and particle-phase velocity V_p along jet axis.
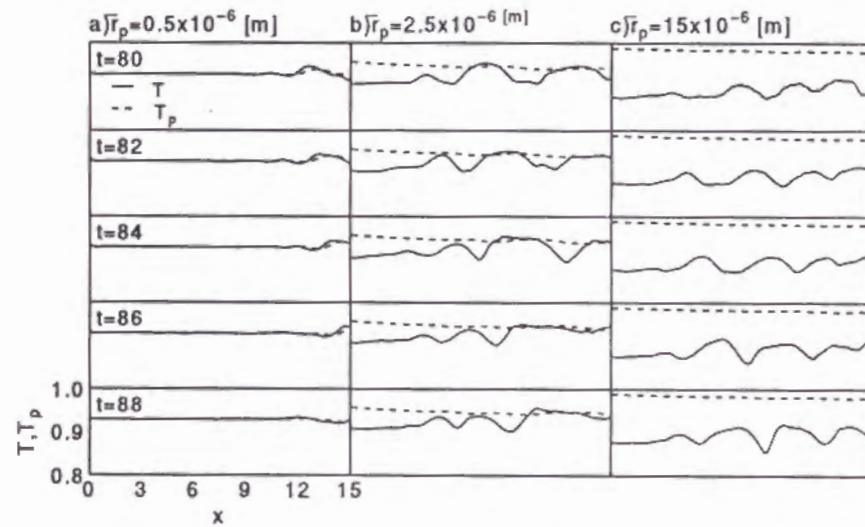

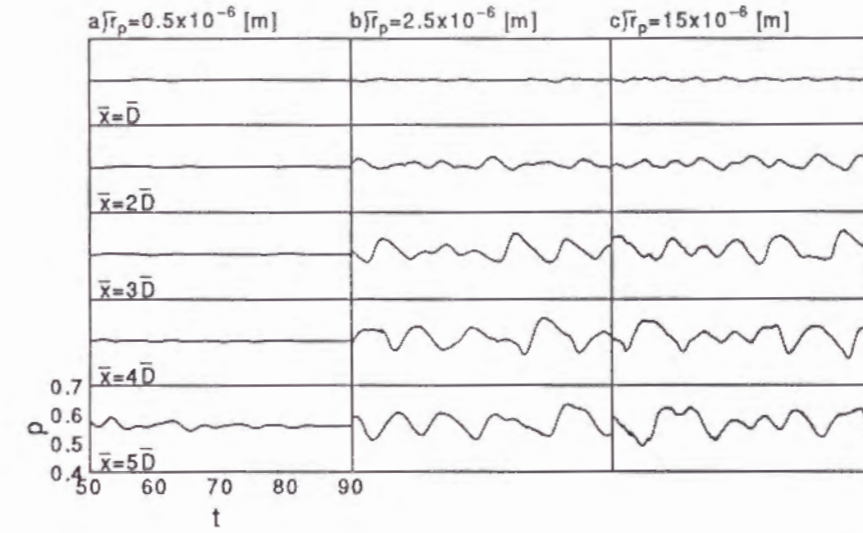Figure 3.7: Distributions of gas phase temperature (T) and particle-phase temperature (T_p) along jet axis.

Figure 3.8: Variation of pressure with time at five points ($\bar{x} = j\bar{D}; j = 1 \sim 5$) along jet axis from $t = 50$ to $t = 90$.

and appreciably strongly downstream. Also, for the case of $\bar{r}_p = 0.5\mu m$, the amplitude of variation is very small even in the downstream region, while for larger particles the pressure fluctuates in a wide range. It is clearly understood that the pressure wave propagates from upstream to downstream with an almost constant velocity.

Figures 3.9(a) to 3.9(c) indicate the time-averaged pressure and temperature of the gas-phase over the time range from $t=60$ to $t=90$. Both the pressure and the temperature are kept almost constant everywhere along the jet axis for the three particle sizes, regardless of being an appreciable fluctuation of instantaneous pressure and temperature.

3.5 Experimental

Essentially it would be desirable to calculate mist flows for which experimental data are available so that a direct comparison could be made. Unfortunately, experiments which provide sufficient data to specify the mist flows do not appear to exist. Therefore, we have made a very simple experiment by using the experimental setup shown in Figure 3.10. The air mist nozzle (Kyoritu Gokin, KNT type) is attached on the top of the chamber. The straight nozzle of 2mm in diameter and 3mm in length is equipped on the bottom of the chamber. The gas-water droplets mixture is first injected from the upper nozzle into the chamber, and then exhausted from the straight nozzle to the atmospheric surrounding. The purpose of chamber would be that the two-phase jet flow from the upper nozzle is once stagnant so that the computational condition could be satisfied. However, in reality, an air/water separation appears to partly occur at the chamber bottom. This has been confirmed by the variation of droplet size along the jet axis. In the present experiment, the droplet size distribution, as well as the velocity distribution, has been measured by an LDA(Laser-Doppler anemometry) system.
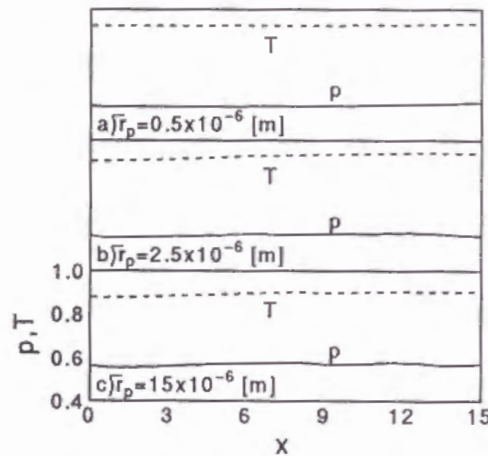
Figure 3.9: Time-averaged pressure and temperature along jet axis. Note that time-averaged values are taken over a time period from $t = 60$ to $t = 90$.
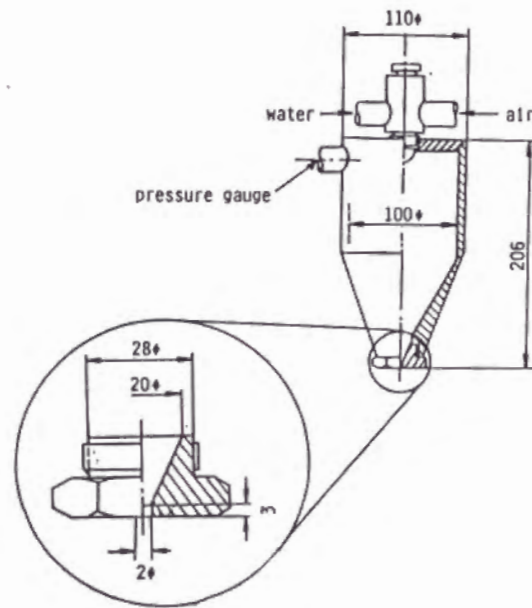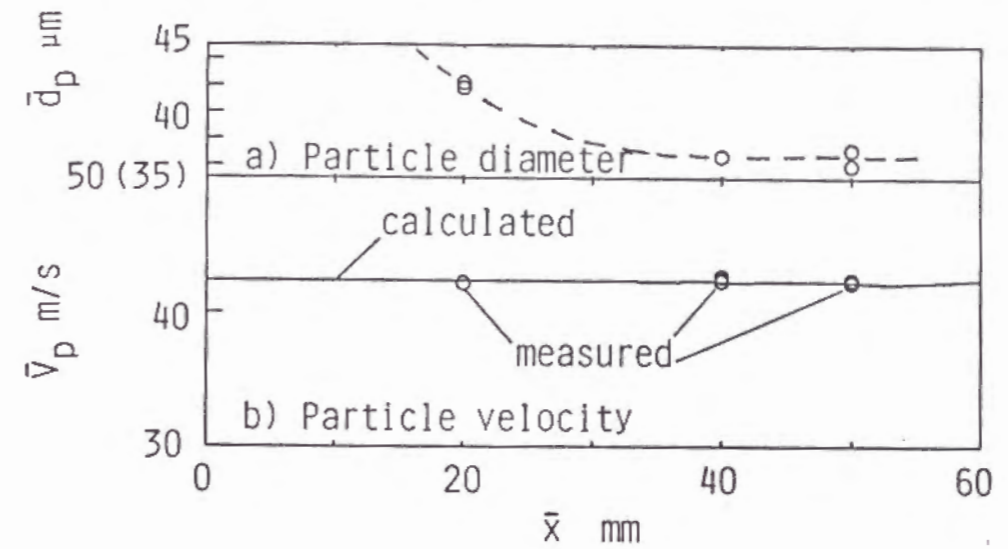

Figure 3.10: Experimental apparatus

Figure 3.11: Mean droplet diameter distribution along jet axis measured by LDA system(a) and comparison of mean droplet velocity distribution measured by LDA system with calculated one by using present numerical model. Note that 100 samples are taken at measurement of one time as data for diameter as well as velocity, and that the time of measurement of one time as data for diameter as well as velocity, and that the time of measurement is all twice at the individual measuring point.

Here, it should be noted that this LDA system, which is called the phase doppler particle analyzer, can measure not only the particle velocity, but also the particle size. Basically this belongs to the same optical system as the conventional LDA one, but three detectors are equipped at a constant space behind the receiver window. A particle passing through the crossing point of two beams scatters the light, and thereby the interference flinge pattern occurs. The flinge interval is proportional to the particle size and the particle size is determinable by measuring the spatial frequency of interference flinge pattern. Again, this system can be applied to a spherical particle of $0.5\mu m$ to $3000\mu m$ in diameter. But, the errors within plus or minus 1.0 per cent or so for larger particles($> 100\mu m$) and within 3.0 percent or so for smaller particles ($\leq 5\mu m$) seem to be unavoidable.

The droplet size ranges from $7\ \mu m$ to $75\mu m$ downstream of 40mm from the straight nozzle exit and the droplet velocity ranges from 15m/s to 75m/s in the region between 20mm and 100mm from the nozzle exit. Also, the mass loading ratio has been measured to be 1.2.

Figure 3.11(a) indicates the measured mean droplet diameter distribution along the jet axis. It can be seen that the relatively large droplets at the location of 20mm from the nozzle exit diminish in mean diameter downstream from there. Further, we note that the droplet size could not be measured in the region from the nozzle exit to the location 20mm or so downstream from it. This may be due to the fact that a stable droplet size is not achieved near the nozzle exit.

Also, it must be noted that it was impossible to measure the gas-phase velocity owing

to the presence of water droplets. Even though the measurement is made by including small seed particles, the results so obtained must be unreliable due to the sticking effect of these particles and water-droplets.

It has been found that the mean droplet velocity distribution along the jet axis measured by the LDA system remains almost constant in the region between 20 and 50mm from the nozzle exit. This implies that in such region the two-phase flow is kept approximately in velocity equilibrium. Therefore, for computational purpose, the gas and particle phases have been assumed to be in equilibrium with each other at the nozzle exit, and the droplet velocity at the nozzle exit has been approximated to be the same as the measured mean droplet velocity.

The volume mean diameter, as well as the mean velocity has been obtained on the basis of the data processing. Such mean values have been introduced to computational data so that the calculation could be carried out.

Practically, the droplet velocity distribution has been calculated by using the present model on the condition that $\bar{u}_E = \bar{u}_{pE} = 42$m/s, $\bar{r}_p = 18.5\mu m$ and $\nu_E = 1.2$. Figure 3.11(b) indicates the comparison of the calculated result with the measured one.

3.6   Discussion

To predict the particle motion in the jet flow, a Lagrangian approach is followed. The trajectory of each particle in the flow is numerically solved directly from the equations of motion. Some assumptions in the particle motion analysis have been introduced. We have already demonstrated that the neglect of virtual mass force, pressure gradient force and Basset force is justified on the basis of an order of magnitude study[12]. Also, the effect of fluids turbulence has been neglected in this analysis. The inclusion of this is inhivitively costly in terms of computer time and memory, in particular, for the two-phase flow problem. However, it may be valid from the numerical results presented here that no turbulence model is needed to establish the overall nature of the flow.

Next, in spite of drastic approximations, very good agreement between the calculated and the experimental results has been obtained. In this analysis, the assumption that the gas-phase is in velocity equilibrium with the particle-phase at the nozzle exit has been used. In reality, it may be reasonable to consider that at least in the vicinity of the nozzle exit the gas-phase is deviates from equilibrium with the droplet-phase, and that the former velocity at the nozzle exit is higher than the mean droplet ones measured in the range from 20mm to 50mm from the nozzle exit, while the latter velocity is lower than the measured values. However, a velocity equilibrium state may be reached immediately downstream from the nozzle exit(see Fig. 3.11(b)). We consider from such a point of view that the above assumption is not so far from the truth at least in the present situation, although it is very difficult to concretely discuss the validity.

Furthermore, we discuss the problem to characterize the particle behavior in a gas flow from a qualitative point of view. Chung and Troutt[17] have numerically analyzed the particle dispersion in an axisymmetric jet by following particle trajectories in a jet flow simulated by discrete vortex rings. According to their analysis, the effectiveness of the large turbulent structures for moving particles in the mixing region can be characterized by the Stokes number, that is, the ratio of the aerodynamic response time $\bar{\tau}_A$ of a particle defined by Eq.(3.7) to the characteristic time scale $\bar{D}/\bar{u}_E$ of the flow field. For the ratio $\gamma_\tau (= \bar{\rho}_{mp}(2\bar{r}_p)^2 \bar{u}_E/18\bar{\nu}\bar{D}) \gg 1$, the particles will not have sufficient time to respond to the gas flow and will move in nearly rectilinear path. For $\gamma_\tau \ll 1$, the particles will have sufficient time to respond to the spreading velocity field of the gas jet. On the other hand, for the condition $\gamma_\tau \sim O(1)$, the gas jet may be able to temporarily capture the particles and fling them beyond the fluid momentum mixing region.

The Stokes numbers for these individual mixtures are that $\gamma_\tau = 0.08$ for $\bar{r}_p = 0.5\mu m$, $\gamma_\tau = 2.0$ for $\bar{r}_p = 2.5\mu m$ and $\gamma_\tau = 75$ for $\bar{r}_p = 15\mu m$, respectively. The present results shown in Figs. 3.6(a) to 3.6(c) and Figs. 3.7(a) to 3.7(c) are clearly quite consistent with the previous discussion.

3.7   Conclusion

For understanding behavior characteristics of gas-particle two-phase free jets practically, a system of equations for the gas and particle phases has been numerically solved for the mixture composed of air and water-droplets. There are some variations in the instantaneous flow properties of the gas-phase depending upon the size of droplets contained in the mixture, but time averaged values over a time period show a quasi-steady flow state. The vortical structure occurring at the jet boundary of the nozzle exit is convected along the boundary downstream and agiates the jet flow.

Again, the numerical water-droplet velocity distribution calculated by using the present flow model has been compared with the measured values. The overall agreement has been found to be remarkable good.

Additionally, it has been confirmed that the response of the particle motion to the gas flow can be specified by the Stokes number, and that the flow structure of mixture with very small particles is in the velocity and thermal equilibrium between the two-phases.

Reference

1. Zucrow, M. J. and Hoffman, J. D., Gas Dynamics, Vol.2, Wiley, New York, (1977), p.53.

2. Hatta, N., Ishii, R., Takuda, H., Ueda, K. and Kokado, J., Trans. Iron Steel Inst. Jpn., (1988), p.930.

3. Hatta, N., Takuda, H., Ishii, R. and Fujimoto, H., ISIJ Int., 29(1989), p.605.

4. Hatta, N., Fujimoto, H., Ishii, R. and Umeda, Y., and Kokado, J., ISIJ Int., 29(1989), p.911.

5. Crowe, C. T., ASME J. Fluids Engg., 104(1982), p.297.

6. Ishii, R., Umeda, Y. and Yuhi, M., J. Fluid Mech., 203(1989), p.475.

7. Crowe, C. T., ASME J. Fluids Engg., 99-2(1977), p.325.

8. Dukowicz, J.K., J. Compu. Physics, 35(1978), p.229.

9. Harlow, F. and Amsden, A., J. Compu. Phys., 17(1975), p.19.

10. Henderson, C. B., AIAA J., 29(1976), p.911.

11. Carlson, D. J. and Hoglund, R. F., AIAA J., 2(1964), p.1980.

12. Maxey, M. R. and Riley, J. J., Phys. Fluids, (1983), p.883.

13. Chakravarthy, S. R. and Osher, S., AIAA paper 85-0163, (1985).

14. Roe, P. L., J. Compu. Phys., 43(1981), p.357.

15. Matsuda, T., Umeda, Y., Ishii, R., Yasuda, A. and Sawada, K., Memoirs of the Faculty of Engg., Kyoto University, 49-1(1987), p.84.

16. Godunov, S. K., Matemat. Sbornink, 47(1959), p.271, also Cornell Aeronautical Laboratory Translation.

17. Chung, J. N. and Troutt, T. R., J. of Fluid Mech., 186(1988), p.199.

18. Hatta, N., Ishii, R. and Fujimoto, H., Trans. ASME J. Fluids Engg., 114(1992), p.420.

Chapter 4

Numerical analysis of flow patterns of impinging liquid sprays in a cold model for cooling a hot flat plate

[15]

4.1 Introduction

There are many industrial situations in which a fine liquid spray contacts and cools a surface which is at a temperature in excess of the liquid saturation temperature. This process is commonly called the spray or mist cooling. In iron- and steel-making industries, the mist cooling method is an established technique and applied to the secondary cooling in the continuous casting system so that a comparatively precise cooling may be achieved to optimize the withdraw velocity of cast slabs and the position of the crater end.

The purpose of the research reported herein is not to identify the fundamental heat transfer processes involved in spray cooling, but to analyze flow structures of the two-phase air-water droplet mixture jet impinging on a flat plate normal to flow.

The equations governing the steady quasi-one-dimensional nozzle flow of a gas containing suspend condensed phase, derived by Zucrow and Hoffman[1], have been extended to the case where a continuous distribution of particle size is present[2]. Then, the system of equations has been applied to the expanding flow of gas-particle mixtures not only in a subsonic nozzle but also in a De Laval nozzle[3-5].

Thereafter, the numerical analysis of gas-particle mixture flows in a free jet region has been made in such a situation that a two-phase mixture is exhausted from a subsonic nozzle into a quiescent gas[6]. The numerical result exhibits that smaller particles tend to follow the gas flow pattern, while the fluctuation of the particle motion becomes smaller for larger particles. The final purpose for a set of such investigations is to find the theoretical heat transfer mechanism of the so-called mist cooling. Hence, the problems of impinging jet on a solid wall must be settled first. A theoretical analysis or experimental measurement approach to explaining this phenomenon may be difficult. The following are the probable reasons for not suggesting either of the two approaches mentioned above.

First, the gas-phase and the particle-phase must be treated as different media. That is, the former is regarded as a continuum medium, and the latter is regarded partly as a discrete one. Second, the numerical procedure of impinging particles on the surface is very difficult. For the secondary cooling of cast slabs, the impinging droplets are deflected from the surface by a thin vapor film which is formed on impact. This is commonly referred to as the Leidenfrost state. In short, non-wetting phenomenon occurs and the direct contact between droplet and hot wall is not observed. In fact, it is possible that in a hot model large droplets with a high velocity break up into small ones on impact and are deflected from the surface. On the other hand, it is anticipated that small particles can evaporate before reaching the hot surface.

Therefore, for simplicity, the numerical calculations of mist flows consisting of air and water-droplets are made on the assumption that particle reflection from the surface is perfectly elastic. Again, the present numerical model is a cold one. The numerical results so obtained exhibit that for larger particles they are dispersed in the flow field owing to the elastic reflection from the surface. The greater part of such particles becomes slow in motion, or simply stays because there is negligible gas velocity in the almost stagnant ambient region outside the mixing core flow. Contributions of these water-droplets to the intensity of the mist cooling may be reduced to a certain degree.

Subsequently, the usage of a low-velocity annular gas-only flow which surrounds a round nozzle co-axially is considered. By so doing, it may be possible to push back particles dispersed spatially from the core flow by the impingement on the surface, to the surface again. We wish to check the effect of the coaxial annular gas flow on the flow field of the particle phase. The present calculations are performed with a single particle size. The two-phase mixture is assumed to be composed of air and water-droplets.

4.2 Governing equations

The flow model for air-droplet mixture is constructed under the following assumptions. (1) No phase change takes place, because the calculation is made in a cold model. (2) The volume occupied by the particles is negligible. (3) The particle-particle collision is neglected, that is, the particles do not interact with each other. (4) Particles are spherical in shape with a uniform diameter and a constant material density. (5) The gas, as well as the particles, has a constant specific heat. (6) As mentioned in the previous section, the particle reflection is elastic. (7) Gravitational effects are not considered.

Here we consider the validity of the items (2) and (3). It is commonly accepted that the material density $\bar{\rho}_{mp}$ of liquid particles is larger by a magnitude of order of 10^3 than that of a gas $\bar{\rho}$. We define the ratio, ν, of the mass of the particle phase to that of the gas phase as $\nu = \epsilon_p \bar{\rho}_{mp}/(1-\epsilon_p)\bar{\rho} \simeq \epsilon_p \bar{\rho}_{mp}/\bar{\rho}$, where ϵ_p denotes the volume fraction occupied by the particle phase per unit volume. Thus, we have $\epsilon_p = \nu\bar{\rho}/\bar{\rho}_{mp}$. When a particle is injected into a uniform space involving the particle cloud of the mean particle spacing $\bar{s}_p$, the particle mean free path $\breve{\lambda}_p$ is expressed by the order of $\bar{s}_p/\epsilon_p^{2/3}$. Thus, $\breve{\lambda}_p/\bar{L} \simeq (\bar{s}_p/\bar{L})/\epsilon_p^{2/3}$, where L denotes a characteristic length of the flow field. Therefore, if $\bar{s}_p/\bar{L} = O(\epsilon_p^{2/3})$, then, $\breve{\lambda}_p/\bar{L} = O(1)$. In this case, the gas particle mixture may be regarded as dilute, and the direct collisions between particles can be neglected. In the

present simulation, the order of ν is unity and therefore $\epsilon_p \simeq O(10^{-3})$. That is to say, if $\nu \simeq O(1)$, $\bar{s}_p/\bar{L} \simeq O(10^{-2})$ may be considered to be a sufficient condition for particles not to collide each other.

In our calculation, the dimensionless variables and parameters are introduced, and the governing equations to be solved will be expressed by dimensionless quantities. It is physically important to rewrite the dimensional equations into dimensionless ones and to solve them in such a way as to realize the similarity of the flow pattern as well as the general validity. The main dimensionless variables introduced into the system of governing equations are defined as

$$
\left.
\begin{aligned}
&t = \frac{\bar{t}}{\bar{L}/\bar{c}_0}, \quad x = \frac{\bar{x}}{\bar{L}}, \quad y = \frac{\bar{y}}{\bar{L}}, \quad \rho = \frac{\bar{\rho}}{\bar{\rho}_0}, \quad p = \frac{\bar{p}}{\bar{p}_0}, \\
&u = \frac{\bar{u}}{\bar{c}_0}, \quad v = \frac{\bar{v}}{\bar{c}_0}, \quad T = \frac{\tilde{T}}{\bar{T}_0}, \quad c = \frac{\bar{c}}{\bar{c}_0}, \\
&x_p = \frac{\bar{x}_p}{\bar{L}}, \quad y_p = \frac{\bar{y}_p}{\bar{L}}, \quad u_p = \frac{\bar{u}_p}{\bar{c}_0}, \quad v_p = \frac{\bar{v}_p}{\bar{c}_0}, \quad T_p = \frac{\bar{T}_p}{\bar{T}_0}
\end{aligned}
\right\}
\tag{4.1}
$$

where t, x and y are the time, axial distance and radial distance, respectively. u, v, p, ρ, T and c are the axial velocity, radial velocity, pressure, density, temperature and speed of sound of the gas, respectively. The subscripts p and 0 denote particles and reference conditions, and the overbar denote the dimensionless quantities. $\bar{L}$ is the characteristic length of the flow system.

In addition to Eq.(4.1), for later convenience, we define the following nondimensional parameters:

$$
f_p = \frac{C_D}{C_{D,Stokes}}, \qquad g_p = \frac{Nu}{Nu_{Stokes}}
\tag{4.2}
$$

$$
\Gamma_r = \frac{\bar{\tau}_A}{\bar{\tau}_F}, \qquad \theta = \frac{\bar{C}_{pp}}{\bar{C}_{pg}}, \qquad \gamma = \frac{\bar{C}_{pg}}{\bar{C}_{vg}}
\tag{4.3}
$$

in which C_D and Nu represent the drag coefficient and the Nusselt number, respectively. The subscript $Stokes$, denotes the Stokes flow regime (i.e. $Re < 1$, Re : the particle Reynolds number). $\bar{C}_{pg}$ and $\bar{C}_{vg}$ are the specific heat of the gas phase at a constant pressure and volume, respectively. $\bar{C}_{pp}$ denotes the specific heat of the particle material. $\bar{\tau}_A$ is called the aerodynamic response time of a particle, assuming the Stokes drag law, and $\bar{\tau}_F$ the characteristic time of the flow system. These are defined by

$$
\bar{\tau}_A = \frac{\bar{\rho}_{mp}(2\bar{r}_p^2)}{18\bar{\mu}}, \qquad \bar{\tau}_F = \frac{\bar{L}}{\bar{c}_0}
\tag{4.4}
$$

in which $\bar{r}_p$ is the particle radius. The gas viscosity $\bar{\mu}$ is given by

$$
\bar{\mu} = \bar{\mu}_0 \left(\frac{\bar{T}}{\bar{T}_0}\right)^{\delta}
\tag{4.5}
$$

where δ is an appropriate constant. Again, we introduce the following nondimensional properties;

$$\mu = \frac{\bar{\mu}}{\bar{\mu}_0}, \quad \lambda = \frac{\bar{\lambda}}{\bar{\lambda}_0},$$

(4.6)

in which λ is the thermal conductivity of the gas.

Here, it is noted that the particle drag coefficient C_D and the Nusselt number Nu used in the present study are those given by Henderson [7] and Carlson & Hoglund[8], respectively.

4.2.1 Particle phase

In the present model, the whole particle cloud is divided into a large number of small subclouds. It is assumed that all the particles belonging to each subcloud have the same velocity and temperature. The particle flow field is solved by selecting an appropriate and representative particle in each subcloud and by following the properties of the particle along the particle trajectory.

By labelling the particle subclouds by subscripts $k(k = 1, 2, 3, \ldots)$ and denoting the velocity components and temperature of a particle located at $(x_{pk}(t), y_{pk}(t))$ by $(u_{pk}(t), v_{pk}(t))$ and $T_{pk}(t)$, respectively, the momentum and energy equations of the k-th particle subcloud are expressed by

$$\frac{d\mathbf{E}_{pk}}{dt} - \mathbf{I}_{pk} = 0,$$

(4.7)

in which

$$\mathbf{E}_p = \begin{bmatrix} x_p \\ y_p \\ u_p \\ v_p \\ T_p \end{bmatrix}, \qquad \mathbf{I}_p = \begin{bmatrix} u_p \\ v_p \\ A_p(u - u_p) \\ A_p(v - v_p) \\ B_p(T - T_p) \end{bmatrix}.$$

(4.8)

The parameters A_p and B_p appearing in the system of the foregoing particle equations are defined by

$$A_p = \frac{f_p}{\Gamma_\tau}, \qquad B_p = \frac{2g_p}{3\Gamma_\tau Pr\theta}.$$

(4.9)

Hence, one of the most important tasks is how to evaluate the particle number contained in the k-th subcloud. Since the flow is considered in the axisymmetric coordinate system, the particle cloud in the physical space forms a ring cloud. Denoting the number of particles contained in the k-th subcloud per unit depth by $N_{pk}(= \tilde{N}_{pk}/\bar{n}_{p0}/\bar{L}^2)$, where $\bar{n}_p$ is the number density of particles, the number of particles contained in the k-th subcloud may be given by $2\pi \bar{y}_{pk}\tilde{N}_{pk}$ $(=2\pi(\bar{L}y_{pk})(\bar{n}_{p0}\bar{L}^2 N_{pk}))$. Thus, we have

$$2\pi y_{pk} N_{pk} = 2\pi y_{pk}^\dagger N_{pk}^\dagger \quad \text{or} \quad N_{pk} = (y_{pk}^\dagger/y_{pk}) N_{pk}^\dagger$$

(4.10)

where the cross denotes the conditions of particles in the k-th subcloud at the nozzle exit.

4.2.2 Gas phase

The Stokes hypothesis is introduced into the equations governing the gas-phase flow in order to reduce the number of properties which characterize the field of stresses in a flowing compressible fluid from two to one. On this premise the system of the axisymmetric Navier-Stokes equations for the gas-phase interacting with the particle-phase can be written in conservation from as

$$\frac{\partial \mathbf{Q}}{\partial t} + \frac{\partial \mathbf{F}_1}{\partial x} + \frac{\partial \mathbf{F}_2}{\partial y} + \frac{\partial \mathbf{G}_1}{\partial x} + \frac{\partial \mathbf{G}_2}{\partial y} + \frac{1}{y}\mathbf{H} + \mathbf{H}_p = 0$$

(4.11)

where

$$\mathbf{Q} = \begin{bmatrix} \rho \\ \rho u \\ \rho v \\ e \end{bmatrix}, \mathbf{F}_1 = \begin{bmatrix} \rho u \\ \rho u^2 + p/\gamma \\ \rho uv \\ u(e + p/\gamma) \end{bmatrix}, \mathbf{F}_2 = \begin{bmatrix} \rho v \\ \rho uv \\ \rho v^2 + p/\gamma \\ v(e + p/\gamma) \end{bmatrix},$$

$$\mathbf{G}_1 = \frac{1}{Re_0} \begin{bmatrix} 0 \\ f_x \\ -\tau \\ uf_x - v\tau - \frac{1}{(\gamma-1)Pr_0}\lambda\frac{\partial T}{\partial x} \end{bmatrix},$$

$$\mathbf{G}_2 = \frac{1}{Re_0} \begin{bmatrix} 0 \\ -\tau \\ f_y \\ vf_y - u\tau - \frac{1}{(\gamma-1)Pr_0}\lambda\frac{\partial T}{\partial y} \end{bmatrix},$$

$$\mathbf{H} = \begin{bmatrix} \rho v \\ \rho uv - \tau/Re_0 \\ \rho v^2 - \alpha/Re_0 \\ v(e + p)/\gamma + \left[vf_y - u\tau - \frac{1}{(\gamma-1)Pr_0}\lambda\frac{\partial T}{\partial y}\right]/Re_0 \end{bmatrix},$$

$$\mathbf{H}_p = \begin{bmatrix} 0 \\ F_{px} \\ F_{py} \\ \dot{Q}_p + \dot{W}_p \end{bmatrix}$$

(4.12)

with

$$\begin{aligned} f_x &= \frac{2}{3}\mu\left(\frac{\partial v}{\partial y} + \frac{v}{y} - 2\frac{\partial u}{\partial x}\right), \\ f_y &= \frac{2}{3}\mu\left(\frac{\partial u}{\partial x} + \frac{v}{y} - 2\frac{\partial v}{\partial y}\right), \\ \tau &= \mu\left(\frac{\partial v}{\partial x} + \frac{\partial u}{\partial y}\right), \\ \alpha &= 2\mu\left(\frac{\partial v}{\partial y} - \frac{v}{y}\right), \\ Pr_0 &= \frac{\bar{C}_{pg}\bar{\mu}_0}{\lambda}, Re_0 = \frac{\bar{L}\bar{c}_0\bar{\rho}_0}{\bar{\mu}_0} \end{aligned}$$

(4.13)

Furthermore, F_{px}, F_{py}, $\dot{Q}_p$ and $\dot{W}_p$ are expressed by

$$F_{px} = \frac{\nu_E}{S_p} \sum N_{pk} A_{pk} (u - u_{pk})$$
$$F_{py} = \frac{\nu_E}{S_p} \sum N_{pk} A_{pk} (v - v_{pk})$$
$$\dot{Q}_p = \frac{\nu_E}{S_p} \sum N_{pk} B_{pk} \frac{\theta}{\gamma - 1} (T - T_{pk}) \qquad (4.14)$$
$$\dot{W}_p = F_{px} u + F_{py} v - \frac{\nu_E}{S_p} \sum N_{pk} A_{pk} \left\{ (u - u_{pk})^2 + (v - v_{pk})^2 \right\}$$

in which

$$S_p = \frac{\bar{S}_p}{L^2}, \quad N_p = \frac{\bar{N}_p}{\bar{n}_{pE} \bar{L}^2}, \quad \nu_E = \frac{\bar{n}_{pE} \bar{m}_p}{\bar{\rho}_E} \qquad (4.15)$$

Here, the subscript E denotes the nozzle exit condition, $\bar{m}_p$ is the particle mass of $\bar{r}_p$ in radius($= (4\pi/3) \bar{\rho}_{mp} \bar{r}_p^3$). Again, the summation including in Eq.(4.14) is taken over the clouds whose centers (x_{pk}, y_{pk}) are in the computational cell with the sectional area $S_p (= \Delta x \Delta y)$.

The system of the gas-phase equations supplemented by

$$e = \frac{p}{\gamma(\gamma-1)} + \frac{1}{2}\rho(u^2 + v^2)$$
$$p = \rho T \qquad (4.16)$$
$$c = T^{1/2}$$

4.3   Computational conditions

The nozzle exit conditions can be numerically determined by solving the system of equations governing two-phase mixture nozzle flows which is described in Ref.[2]. The sectional area A of the nozzle is assumed to consist of the two regions from the reservoir to the nozzle exit as

in the first region of $x < -5$ $\qquad A = (x + 5)^2 + 1$

in the second region of $-5 \leq x \leq 0$ $\qquad$ A=1

It should be kept in mind that the nozzle exit $(x = 0)$ corresponds to the origin of the jet axis. Again, the nozzle radius is taken to be $\bar{D}/2 = 5 \times 10^{-3}$[m] in the second region, and the area is made dimensionless by dividing A by the sectional area in the second region. The reservoir and ambient gas conditions are assumed to be as follows:

the reservoir conditions:

$\bar{p}_0 = 1.8 \times 10^5$ [Pa]
$\bar{T}_0 = 323$[K]
$\nu_0 = 0.3$

the ambient gas conditions:

$\bar{p}_\infty = 1.0 \times 10^5$ [Pa]
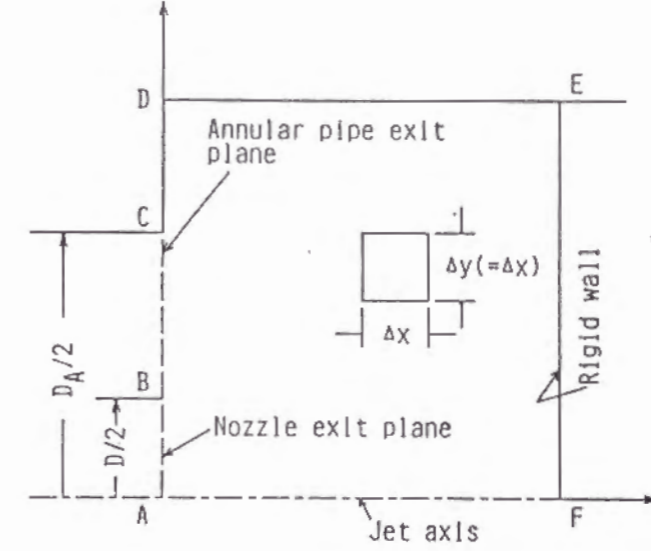$\bar{T}_\infty = 300$ [K]

Figure 4.1: Geometry of computational domain.

where the subscripts 0 and ∞ denote the reservoir and the ambient gas conditions, respectively. It is noted that the reservoir condition is adopted as the reference condition by which the physical variables are non-dimensionalized. Also, in the present numerical experiment, it is assumed that water-particles contained in the mist have a single-size. Three cases are treated where $\bar{r}_p = 1.0$ [μm], 5.0 [μm] and 10 [μm], respectively. Eventually, we have obtained the numerical flow properties at the nozzle exit as follows:$u_E = 0.779, u_{pE} = 0.764, T_E = 0.924, T_{pE} = 0.936$ and p_E=0.556 for the mixture of $\bar{r}_p = 1.0$ [μm], $u_E = 0.779, u_{pE} = 0.627, T_E = 0.888, T_{pE} = 0.973$ and p_E=0.556 for the mixture of $\bar{r}_p = 5.0$ [μm], $u_E = 0.790, u_{pE} = 0.519, T_E = 0.879, T_{pE} = 0.984$ and p_E=0.556 for the mixture of $\bar{r}_p = 10$ [μm], respectively, These numerical results provide the jet boundary condition at the origin of the two-phase jet impinging on a surface.

The gas-phase equations are solved by using the TVD(Total Variation Diminishing) scheme developed by Chakravarthy and Osher[9], and the particle-phase is solved by applying a discrete particle-cloud model. In the scheme, the computational domain is divided into a large number of small cells and the physical variables are defined at the cell center. That is, the computational domain is divided into 120×200 cells (or meshes) in the x- and y- directions, respectively. Here, we wish to add that the physical variables at interface between two neighboring cells is calculated by the Roe approach[10].

Figure 4.1 indicates the geometry of computational domain of the case where the coaxial annular gas-only flow is present. The annular pipe is assumed to consist of coaxial inner and outer circular tubes. The thickness of the inner tube is neglected and therefore $\pi(D_A^2 - D^2)/4$ corresponds to the annular gas-only flow region, where D_A is the inner diameter of the outer pipe. Again, the gas-phase is assumed to be discharged from the annular region at $x = 0$ with a uniform velocity $u_A(v_A = 0)$. The pressure and temperature of the gas-phase discharged from the annular region are equal to p_∞ and T_∞ of the ambient gas, respectively. The computation of $D = D_A$, of course, corresponds to the case where the coaxial annular gas flow is absent.

The characteristic length of the flow field is taken to be equal to $\bar{D}/2(\equiv \bar{L})$.

We wish to mention the effect of selecting the cell size $\Delta x, \Delta y$ as well as the computational time interval Δt on the numerical accuracy. First, we consider the problem of the cell size Δx has been determined (Δy is taken to be equal to Δx) by dividing the nozzle radius in n equal parts. For $n = 5, 10, 15, 20$ and 30 the numerical results, for example, the values of the pressure distribution along the x-axis have been compared with each other at a certain same time. It has been confirmed that the numerical results for the case where n is selected at 20 and 30 are almost unvaried, although the accuracy is improved, as n is increased. Then, $\Delta x(= \Delta y)=0.05$, corresponding to $n=20$, is selected in the present numerical simulation.

Next, the time interval Δt is determined by the CFL(Courant-Friedrichs-Lewy) condition for the gas-phase flow [11]. The numerical results obtained by using various CFL numbers have been compared with each other at a certain same time, and then it has been confirmed that almost the same numerical results are obtained on the condition that the CFL number, $f \leq 0.25$. Throughout the present numerical experiments, the CFL number is selected at $f=0.25$. Also, we wish to stress that the time interval, Δt, determined by this CFL number is always much smaller than the particle relaxation times $\tau_{pv}(= 1/A_p)$ and $\tau_{pT}(= 1/B_p)$ for the present flow conditions. Therefore, this Δt is also used in the particle-phase solution.

The numerical boundary conditions of the computational domain are employed in the following mode. The jet condition is applied on the line AB (see Fig.4.1). The gas inflow condition is imposed to the line BC corresponding to $(D_A - D)/2$ of the annulation. The ambient gas condition is imposed to the upstream boundary CD and the side boundary DE. It is self-evident that for the case where the coaxial annular gas flow is absent, the boundary condition imposed to the line BC is the same as that of CD. The no-slip condition is applicable to the downstream boundary EF corresponding to the flat plate surface where $u = v = 0$. The symmetry condition is applied to the jet axis, AF. For detailed physical interpretation of each condition, refer to Matsuda et al.[12].

In addition, the initial ambient gas condition is that $p = 0.556$, $T = 0.929$ and $u = v = 0$ over the whole computational domain. The two-phase jet and the cocurrent annular gas-only flow region to blow at $t = 0$ from the round nozzle and the annular pipe, respectively.

The present calculations are performed by an explicit time-dependent difference scheme. Therefore, in order to obtain the time-converged two-phase flow structure we must require the numerical results at a sufficiently large number of time steps. In the present calculation, the gas-only flow field is solved for the first 20000 time steps, and then the flow field of the two-phase mixture is computed for the next 15000 time steps (from the 20001 to the 35000 time step) so that the time-converged solutions may be obtained as in short computational time as possible.

Physical constants of the gas and particles adopted here are listed in Table 4.1. Again, the thermal conductivity, $\bar{\lambda}$, is formulated as

$$\bar{\lambda} = \bar{\lambda}_0 + 7.5 \times 10^{-5}(\bar{T} - \bar{T}_o). \tag{4.17}$$

Table 4.1: Physical constants of gas and particles

Gas(air)	Particle(water droplet)
$\gamma = 1.4$	$\bar{C}_{pp} = 4187$ [J/kg·K]
$\bar{C}_{pp} = 1009$ [J/kg·K]	$\bar{\rho}_{mp} = 1000$ [kg/m³]
$\bar{\mu}_r = 2.0 \times 10^{-5}$ [Pa·s]	
$\delta = 0.76$	
$\bar{\lambda}_0 = 0.028$ [W/m·K]	
$Pr = 0.71$	

4.4 Numerical results

In various industrial fields, it is often crucially important to know the particle trajectories in a carrier gas. In this section, the behavior of particles in the gas flow is investigated in detail. In the jet flows impinging on a flat plate, the particles are injected with an initial velocity determined by the particle size at fixed points on the nozzle exit plane at each time step after the final step in the one-phase solutions.

Figure 4.2 shows the one-phase solution at N=20000 ($t \sim 135$, N; time step) for the case where $D_A = 2D$ and $u_A = 0.5u_E$, where u_E denotes the gas velocity at the exit of the inner nozzle. The viscous forces in the equations of gas motion are taken into consideration according to one of the reviewers of this paper. He has pointed out that the friction forces in free jets lead to the turbulent exchange with stagnant gas of the ambient region and herewith to the gas entertainment.

Now we consider the impinging two-phase mixture jet flow for the case where the coaxial annular gas-only flow is absent.

Figure 4.3 gives the velocity vector fields for the gas-phase and the particle-phase of $\bar{r}_p =1.0$ [μm] at $t \sim 100$. The particles are exhausted from the nozzle exit plane at $y_{pk}^\dagger = (k - 0.5)/20$ ($k = 1 \sim 20$) at every time interval Δt. Also, it is noted that only the particles ejected from the nozzle at every 20 time steps are chosen in the present vector fields of the particle phase. It can be seen that the main jet flow of gas-phase interacts with the ambient gas at the jet boundary. Also, the magnitude of particle velocity becomes much smaller near the surface and the distance of the reflection from it is very small and hence the velocity of rebounding particles is negligibly small in magnitude. That is, the impinging particles can not be reflected from the surface at all, but can be transported only in the radial direction except for a small part of particles which is influenced by the motion of vortical structures of the gas-phase. An appreciable concentration of particles can be seen to occur on the surface.

Figure 4.4 indicates the corresponding velocity vector fields for $\bar{r}_p =5.0$ [μm] at $t \sim 100$. At a glance, these flow fields are entirely different from the previous case of 1.0[μm]. With increasing particle size, the particles impinge on the plate surface with larger normal velocity components. It is empirically and theoretically reasonable to consider that larger particles are not decelerated due to the mass effect or inertia effect regardless of the decrease in the normal velocity components of gas-phase near the plate surface. As a
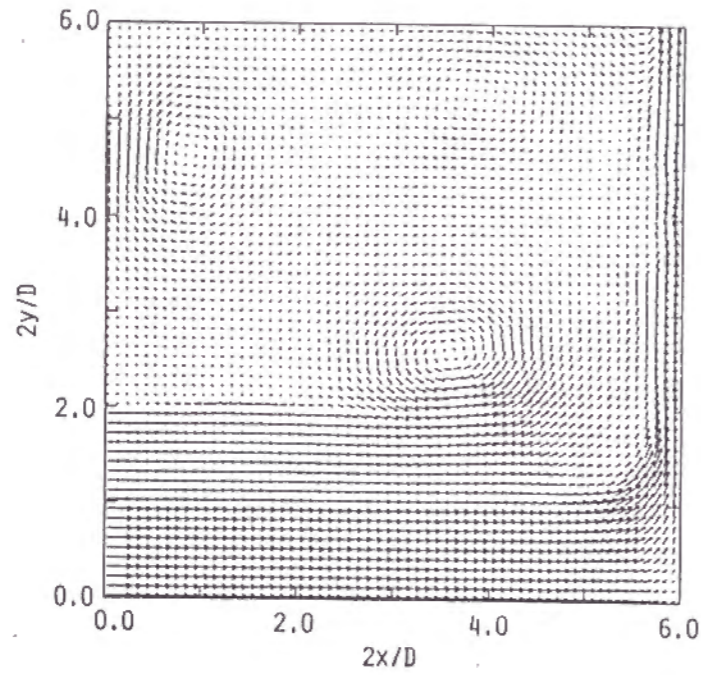
Figure 4.2: Velocity vector field for interaction of impinging central single phase (gas-only) jet with low velocity annular one on a surface at $t \sim 135$.
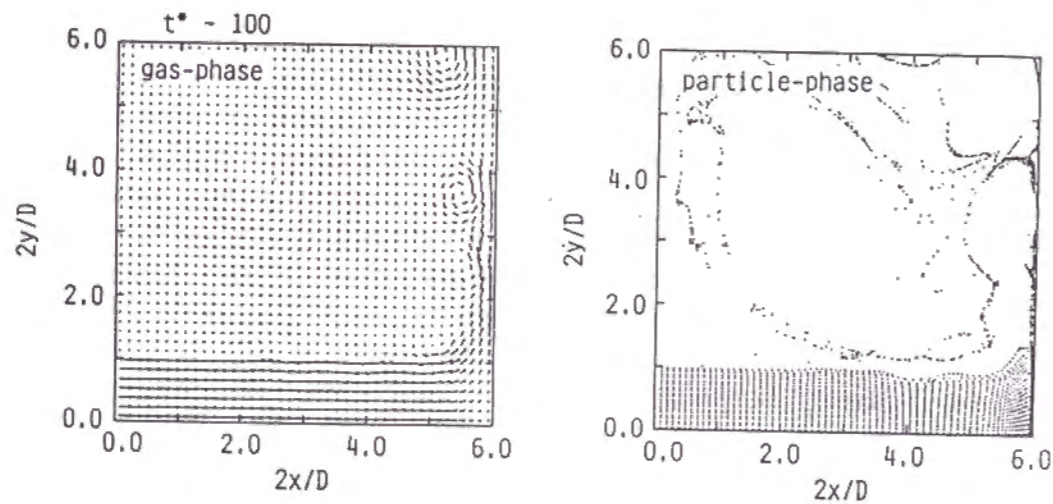

Figure 4.3: Velocity vector fields for both gas and particle phases for mixture of $\bar{r}_p = 1.0$ [μm] at $t \sim 100$ without annular gas flow.
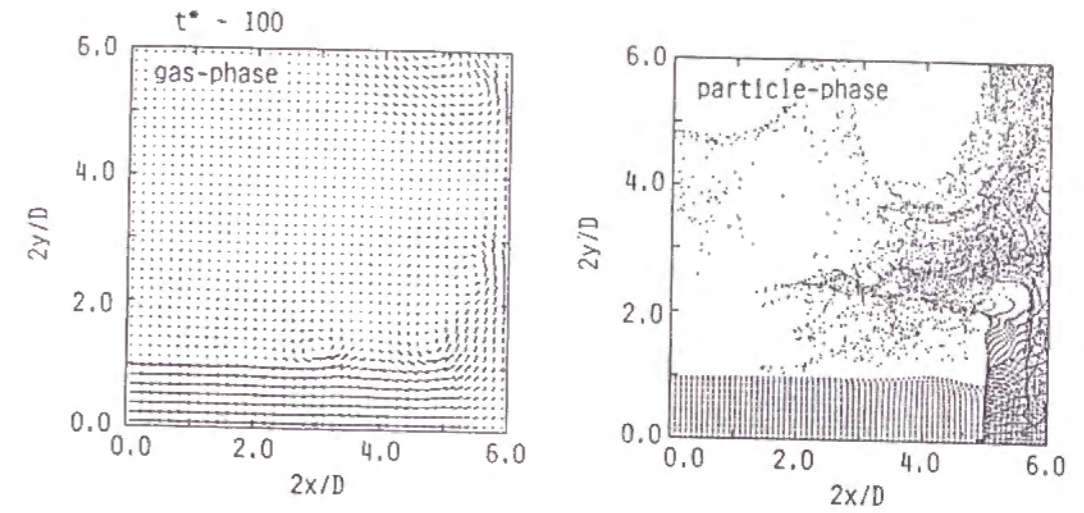

Figure 4.4: Velocity vector fields for $\bar{r}_p = 5.0$ [μm] corresponding to Figure 4.2 at $t \sim 100$.

result, the reflected particles travel upstream larger distances until these are decelerated by the gas flow and are again pushed back in the main flow direction. It is understood that an appreciable part of particles does not directly contact the plate surface.

Figure 4.5 indicates the corresponding results for $\bar{r}_p$=10 [μm] at $t \sim$100. It can be seen that a great part of droplets are reflected far from the surface after the impingement process. The dispersion state of particles are found to be widely different from that of smaller ones in comparison with the case where droplets of $\bar{r}_p$ =1.0 [μm] contact the surface or are very close to it, although the assumption of perfectly elastic reflection is introduced to the numerical model.

Next, we consider the flow fields of the gas and particle phases for the case where the coaxial annular gas flow is present. The numerical calculations are performed on the condition that $D_A = 2D$ and $u_A = 0.5u_E$.

Figure 4.6 gives the numerical results for $\bar{r}_p$ =1.0 [μm] at $t \sim$100. It can be seen that the particles cover the surface in an almost sticking state. It is very interesting that there are almost no distinct vortical structures in the flow field of the gas phase and there are no distortions in the gas velocity vectors nearest to the surface. Therefore, the particles are transported by the gas flow in a regular manner on the surface, compared with the case where the coaxial gas flow is absent.

Figure 4.7 shows the calculated flow fields of $\bar{r}_p$ =5.0[μm] at $t \sim$100. The particles can be divided into two groups. One is the particles impinging on the surface near the jet axis which experience a few collisions with the surface, before they flow out of the free jet region. The other is the particles impinging on the surface near the jet boundary which experience only one collision. The latter particles are pushed back toward the surface by the coaxial flow. At any rate, it may be confirmed from this numerical results that all of the particles are transported in the radial direction on the surface, although they are not so close to the surface.

Figure 4.8 indicates the numerical results of $\bar{r}_p$ =10[μm] at $t \sim$100. This case is similar to the previous case of $\bar{r}_p$ = 5.0[μm] except that the effect of the particle reflection from
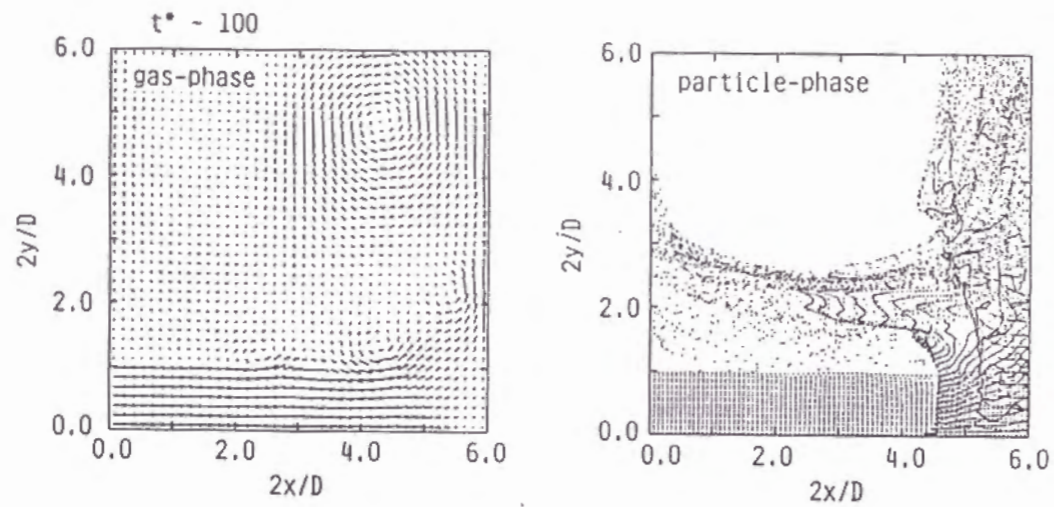
Figure 4.5: Corresponding velocity vector fields for $\bar{r}_p = 10$ [μm] at $t \sim 100$.
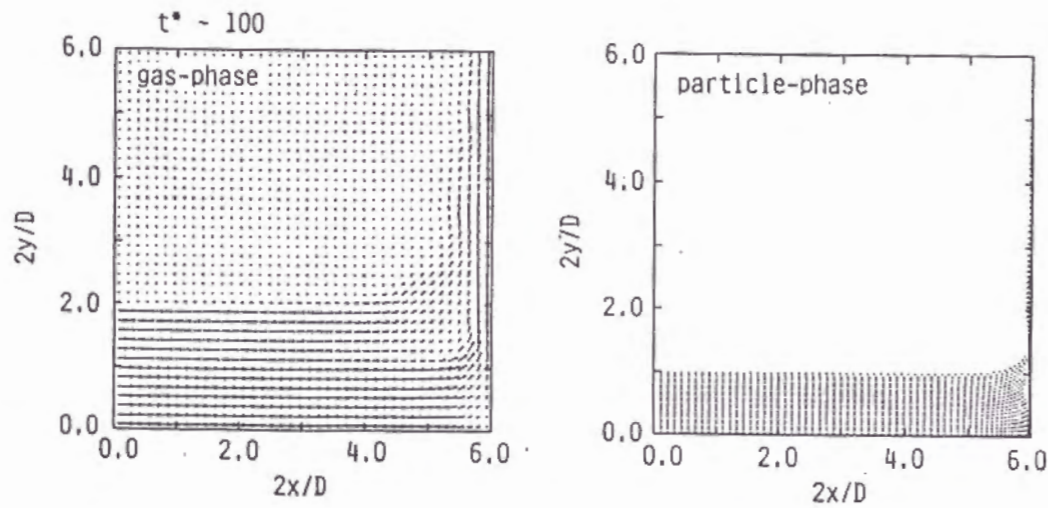

Figure 4.6: Velocity vector fields of gas and particles of $\bar{r}_p = 1.0$ [μm] for the case where $D_A = 2D$ and $u_A = 0.5u_E$ at $t \sim 100$.
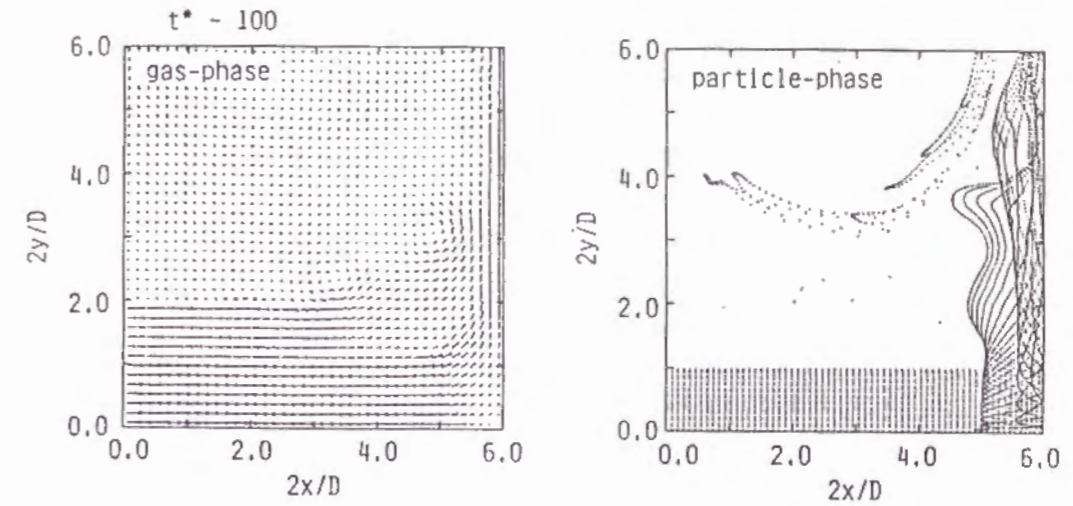

Figure 4.7: Velocity vector fields for $\bar{r}_p = 5.0$ [μm] corresponding to Figure 4.6.

the surface is considerably large in comparison the previous case. The particles which experience a few collisions with the surface are pushed back to the surface by the coaxial gas flow. A part of particles is observed to be slow in motion, or simply stays because there is very small gas velocity in the downstream region of the wall jet. In truth, one of the reviewers of this paper has pointed out that the numerical results that single particles simply stay in a negligible gas velocity region are based upon neglecting the body force in the derivation of the equations of particle motion. This approach, however, is not only very costly but also almost impossible in terms of computer time and storage requirements due to the fact that the introduction of the body force (the gravitational force) results in the three-dimensional problem, because the horizontal flows are considered here.

We note that for every gas-phase flow vortical structures occurring at the jet boundary near the nozzle exit are transported to the downstream and the same process is almost steadily repeated. It is a characteristic feature that the motion of smaller particles is strongly influenced by such vortical structures, especially on the wall jet boundary.

4.5 Discussion

It is important to characterize how the particles disperse in a gas flow according to the difference in the particle size, especially when the gas-particle two-phase flow is applied to the secondary cooling in the continuous casting system. This is because the flow fields for the gas and particle phases give a strong influence to the cooling intensity. Chung and Troutt[13] have numerically analyzed the particle dispersion in an axisymmetric jet by following particle trajectories in a jet flow simulated by discrete vortex rings. According to their analysis, the effectiveness of the large turbulent structures for moving particles in the mixing region can be characterized by the Stokes number, that is, the ratio of the aerodynamic response time $\bar{\tau}_A$ defined by Eq.(3.7) to the characteristic time scale $\bar{D}/\bar{u}_E$ of the flow field. For the ratio $\gamma_\tau (= \bar{\rho}_{mp}(2\bar{r}_p)^2\bar{u}_E/18\bar{\mu}\bar{D}) \gg 1$, the particles have not enough time to respond to the gas flow and move in approximately rectilinear path. For
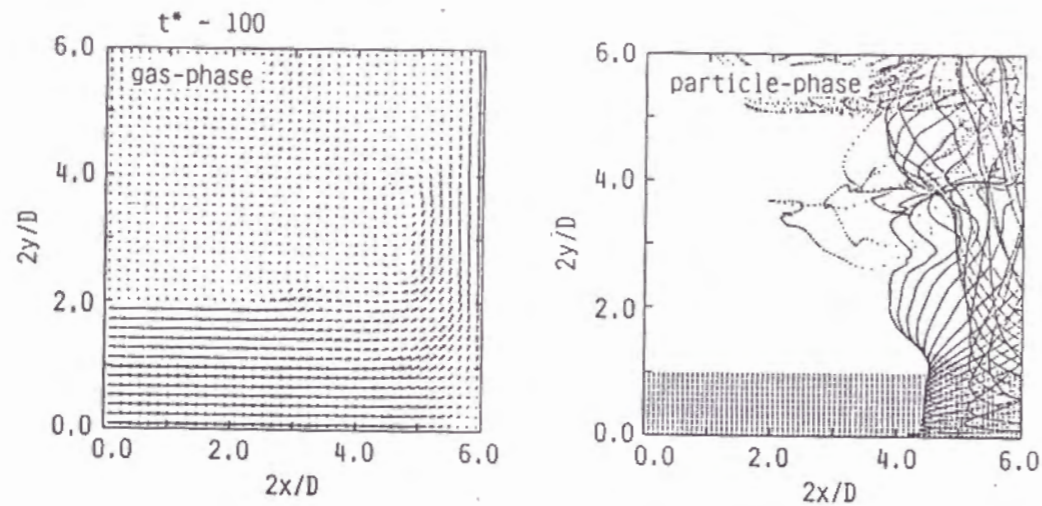
Figure 4.8: Corresponding velocity vector fields for $\bar{r}_p = 10$ [μm].

$\gamma_\tau \ll 1$ the particles have sufficient time to respond to the spreading velocity field of the gas jet and disperse laterally with the spreading rate of the gas jet. In addition, for $\gamma_\tau \sim 1$ the gas jet can capture the particles and fling them beyond the fluid momentum mixing region.

We consider the application of the above regime of the particle motion to the present numerical results by taking for example the case where the coaxial gas-only flow is absent, because the velocity difference at the jet boundary between the free jet and the ambient gas regions is larger than in another case.

Figure 4.9 shows the streaklines of particles exhausted from each starting radial point on the nozzle exit plane with the identical condition to that in Fig.4.3. $\gamma_\tau = 0.34$ in this case. The particles form an almost straight trajectory except for those whose discharging points are closer to the nozzle wall, until they reach the surface. Also, the particles closer to the jet boundary travel radially on the surface with a very small velocity and then are separated from it by a vortical structure of the flowing gas. At any rate, the particles follow the fluctuation of the gas phase. This is quite consistent with the above regime of the smaller Stokes number.

Figure 4.10 shows the corresponding result for $\bar{r}_p = 5.0$ [μm]. $\gamma_\tau = 8.7$ in this case. For starting radial locations which are closer to the centerline, the particles interact with the core flow of the jet which carries more momentum in the axial direction. This means that particles exhausted at locations closer to the jet axis have higher axial momentum and then experience a few collisions and less reflection distance. After that, they are transported radially on the surface. But, the particles exhausted at locations near the nozzle wall experience only one collision. These particles reflected from the surface move away from the core flow of the jet and get flung out to the almost stagnant ambient region. They are not transported to the radial direction on the surface, but reveal somewhat complicated behavior outside the free jet and the wall jet regions.

Figure 4.11 shows the corresponding result for $\bar{r}_p = 10$[μm]. The present case where $\gamma_\tau = 35.6$ demonstrates that the distance which the particles exhausted at locations near
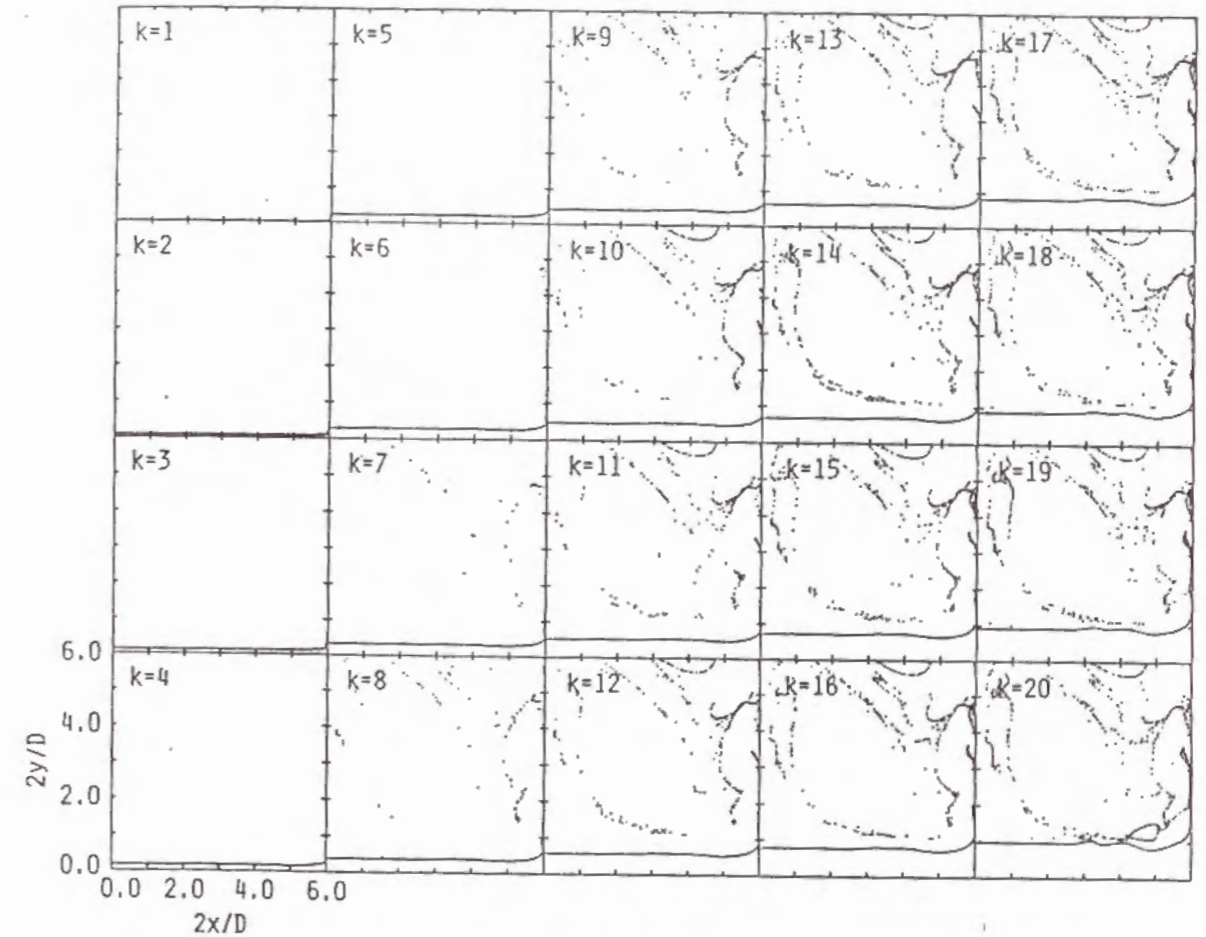

Figure 4.9: Particle distribution pattern at $t \sim 100$ for particles of $\bar{r}_p = 1.0$ [μm] exhausted at each starting point on nozzle exit plane without annular gas flow.
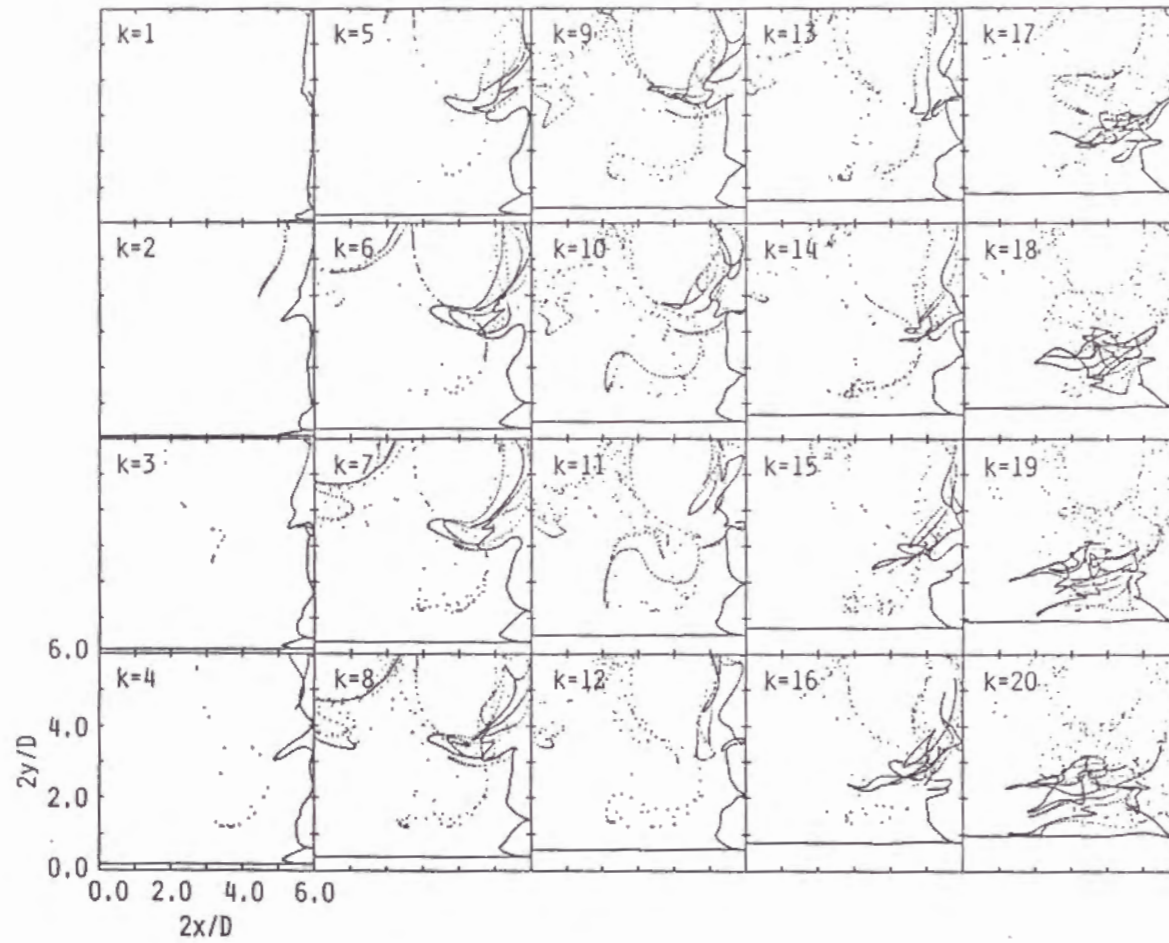
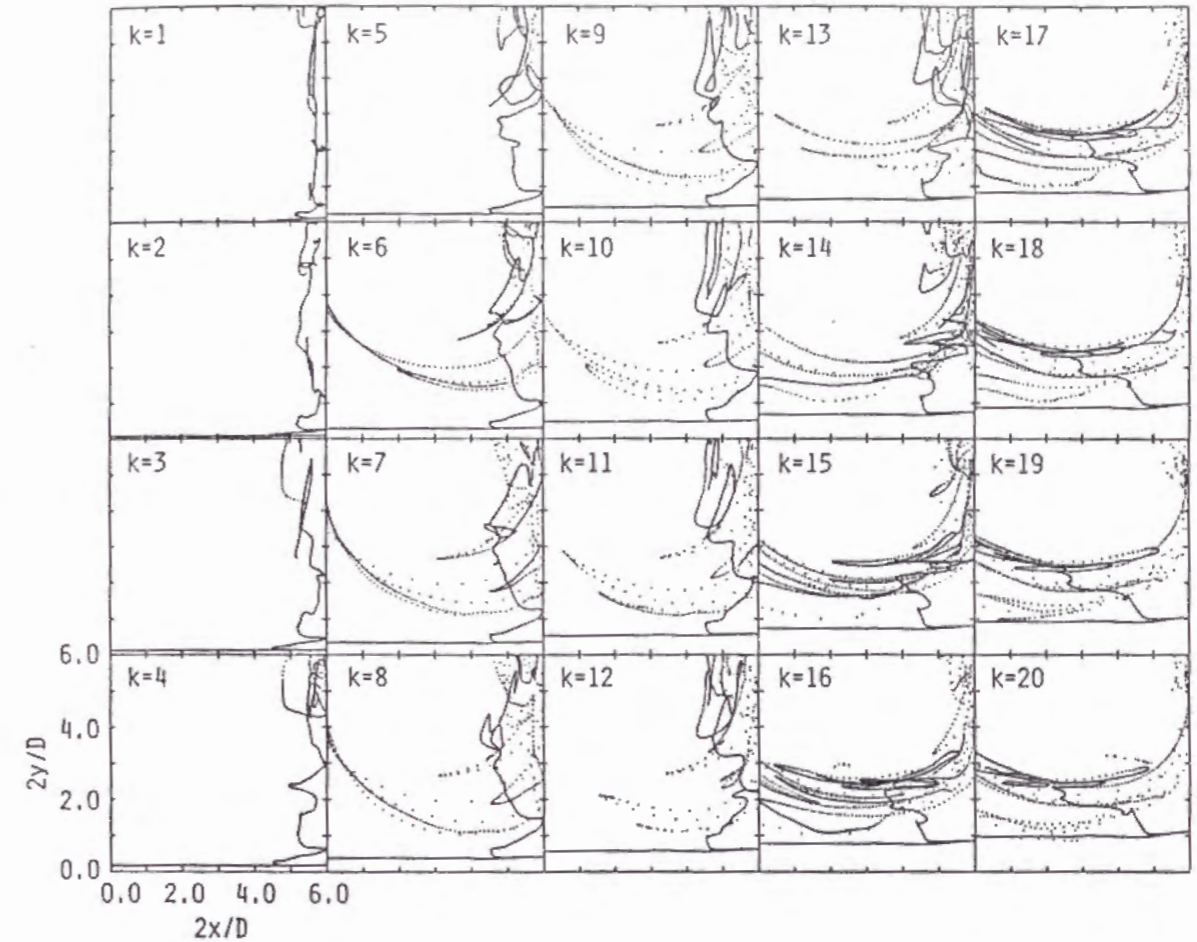Figure 4.10: Particle distribution pattern at $t \sim 100$ for $\bar{r}_p = 5.0$ [μm] corresponding to Figure 4.9.

Figure 4.11: Corresponding numerical result for $\bar{r}_p = 10$ [μm].

the nozzle wall travel by the reflection from the surface is notably large. As seen in Fig. 4.10, the particles exhausted at locations near the centerline tend to move radially on the surface after a few collisions, while the particles exhausted at locations near the nozzle wall do not always approach the surface after only one collision and move very unsteadily outside the core flow of the jet and the wall jet. This is due to the presence of a large scale leading vortex remaining downstream of the wall jet in an almost stationary state (see Fig.4.5).

In general, relatively larger particles with smaller drag/inertia ratios move away from the core of the relatively large vortical structures and penetrate the outer region. For even higher γ_τ, particles become less influenced by the flow structures as shown in Figs. 4.10 and 4.11 where the radial dispersion of $\bar{r}_p=10$[μm] is much reduced as compared with that of 5[μm], and the latter is much smaller than that of 1[μm]. It has been demonstrated from the previous numerical experiments that the annular gas flow can push back these dispersed particles to the surface. However, at the present stage, it is very difficult to evaluate the effect of including annular gas on the mist cooling intensity from a quantitative point of view.

To predict the particle motion in the impinging jet flow a Lagrangian approach is

followed. The trajectory of each particle in the flow is numerically solved directly from the equation of motion. Some assumptions in the particle motion analysis are introduced. First, virtual mass force, pressure gradient force and Basset force are all neglected. An order of magnitude study based on the equation given in Maxey and Riley[14] reveals that virtual mass and pressure gradient are of the order of the density ratio, $\bar{\rho}/\bar{\rho}_{mp}$, and Basset force is of the order of $(\bar{\rho}/\bar{\rho}_{mp})^{1/2}$. Since, $\bar{\rho}/\bar{\rho}_{mp}$ is assumed to be 10^{-3} for a gas-water droplet flow system, the neglect of those forces may be justified. In addition, Chung and Troutt state that Basset force may become relatively important for $\gamma_r > O(10^2)$ as compared to the drag force which is the dominant force in the particle motion analysis. Other force fields including gravity are neglected in this analysis. The axisymmetric flow is considered to be horizontal, as mentioned already. The inclusion of the gravitational force is inhibitively costly in terms of computer time and memory. Also, the effect of fluid turbulence is neglected due to the same reason as the above.

It is assumed that no particle coalescence or particle breakup occurs. This implies that the particles are sufficiently dispersed that particle collisions are infrequent. In fact, $\nu = O(1)$ and $\bar{s}_p/\bar{L} = O(10^{-2})$ give a sufficient condition for the particle phase to be dilute, as described in the previous section. Therefore, we believe that the neglect of particle-particle collision is approximately justified.

The assumption that the particle reflection from the surface is elastic is not commonly justified regardless of whether the numerical model is in a hot or cold one. The mechanism of the reflection of water-droplets from the hot surface beyond the Leidenfrost point is considered to be entirely different from that of the solid particles. The reflection or deflection of droplets may occur owing to the fact that the thermal energy transferred from the hot surface to them changes into the kinetic energy. At the present stage, it is very tedious to follow the thermal process exactly. This problem also remains for future study.

4.6　Conclusion

The numerical analysis of flow pattern of two-phase mixture impinging on a flat plate has been performed by a time-dependent technique. The mixtures composed of air and water-droplets have been treated. In order to put together droplets dispersed radially to the surface, the introduction of an annular gas-only flow has been proposed and the interaction of the central impinging two-phase jet on the surface with the low velocity annular jet has been simulated from a point of view of numerical experiments. The flow structures for air and droplets strongly depend upon the particle size. It is clearly demonstrated that for smaller particles the particle distribution pattern gives a good visualization of the jet vortex structures in the jet flow and particle dispersion is approximately equal to that of the fluid. For larger particles the particles do not have sufficient time to respond to the large vortex structures and move in somewhat rectilinear path.

The numerical results reveal that it is roughly possible to put together the dispersed particles to the surface by the annular gas-only flow, although the effect of including the annular gas flow on the cooling intensity has not been examined from a quantitative point of view.

Reference

1. Zucrow, M. J. and Hoffman, J. D., Gas Dynamics, vol.II, John Wiley and Sons, New York(1977)53.

2. Hatta, N., Ishii, R., Takuda, H., Ueda, K. and Kokado, J.Trans. ISIJ(1988), p.930.

3. Hatta. N. Takuda, H,, Ishii, R. and Fujimoto, H., ISIJ Int. 29(1989), p.605.

4. Hatta. N. and Nakamura, M., ISIJ Int. 29(1989), p.796.

5. Hatta, N., Fujimoto, H., Ishii, R., Umeda, Y. and Kokado. J.,ISIJ Int. 29(1989), p.911-918.

6. Hatta, N., Fujimoto, H., Ishii, R. and Kokado. J., ISIJ Int. 31(1991), p.53.

7. Henderson, C. B., AIAA J., 14(1976), p.707.

8. Carlson, D. J. and Hoglund, R. F., AIAA J. 2(1964), p.1980.

9. Chakravarthy, S. R. and Osher, S.,AIAA paper 85-0363.

10. Roe, P. L., J. Compu. Phys., 43(1981) p.357.

11. Godunov, S. K., Matenat. Sbornik 47(1959) p.271.

12. Matsuda, T. Umeda, Y., Ishii, R. Yasuda, A. and Sawada, K., Mem. Fac. Engg. Kyoto University, 49-1(1987), p.84.

13. Chung, J. N. Troutt, T. R.. J. Fluid Mech., 186(1988), p.199.

14. Maxey, M. R. and Riley, J. J., Phys. Fliuds (1983), p.883.

15. Hatta, N., Fujimoto, H. and Takuda, H., Applied Sci. Res., 50(1993), p.129.

Chapter 5

Collision dynamics of a water droplet impinging on a rigid surface above the Leidenfrost temperature [11]

5.1 Introduction

To predict spray/mist cooling heat transfer, it is indispensable to systematically understand the collision dynamics of liquid droplets on a heated rigid surface beyond the Leidenfrost temperature. Again, because there are a number of parameters affecting heat transfer mechanism between the droplets and the surface and the interaction among of these parameters are very complicated, it is even now a difficult task to evaluate the cooling capacity by a predictable expression.

The collision dynamics of a water droplet on a hot solid surface beyond the Leidenfrost temperature are discussed from an experimental point of view. Now, let it be assumed that a water droplet falls vertically through air and terminates its flight by colliding with a horizontally fixed hot plate surface. After the droplet impinges on the surface it can splash, spread and/or rebound. It is well-known that the phenomenon to be expected may be governed by both the impact energy of the droplet and the temperature of the surface. When the droplet has the low Weber number corresponding to a low impact energy, the droplet may stick and spread and eventually reside as a lens-shaped mass on the surface or rebound as a bowling pin-shaped mass from the surface. While for high Weber numbers the droplet may shatter during the deformation process. According to a few investigations[1,2] performed so far it was confirmed that both the maximum spreading diameter on the surface and the boundary whether the droplet rebounds or shatters depend on the Weber number. Also, it was reported[3] that the resident time of the droplet on the hot plate surface agrees approximately with the first-order vibration period of a freely oscillating droplet. These experimental results were derived by using relatively large droplets of $1 \sim 3$ mm in diameter. Actually, the droplet diameters in spray cooling are regarded as being in the range between 100 μm and 500 μm. It can

be doubtful whether the experimental results obtained by using such comparatively large droplets are applicable directly to the case where the droplet size is small in the order of 100 μm.

Next, we have undertaken the theoretical analysis of mist/spray cooling process to assess the cooling intensity. To do this, we numerically analyzed flow structures of the two-phase air-water droplet mixture jet impinging on a flat plate normal to flow[4,5]. However, the numerical calculations were made on the assumption that the droplet reflection from the surface is perfectly elastic. The major reason for introducing the assumption was because the coefficient of restitution remains unclarified between the water droplets and the hot surface. Indeed, we can find some investigations on the collision of a very small droplet with a hot solid surface. Pederson[6], Shoji et al.[7], and Xiong & Yuen[8] treated the collision phenomena of fairly small droplets of the order of 100 μm on the hot surface. However, they placed emphasis not upon the collision dynamics, but upon the heat transfer between the droplet and the surface. Jeffrey & Patrick[9] examined the deformation process of the droplet with the Weber number as the parameter. That is, they inspected the Weber number before and after the collision, when the droplet rebounds, and measured the diameter and velocity distributions of individual particles, when the droplet shatters during the deformation process. But the criterion of the rebounding and the disintegrating was not made clear because the experimental condition was restricted to a narrow range.

In the present chapter, the collision behavior of water droplets from 300 μm to 600 μm in diameter on the surface heated at 500 °C and the rebounding/disintegrating phenomena have been investigated experimentally. The first purpose of the present study is to examine whether or not the past empirical rules obtained by using the large droplets of 1 mm to 3 mm in diameter give an applicability to the case where the droplet size is much smaller. The second is to clarify the relation between the Weber number and the coefficient of restitution when the droplet rebounds from the heated rigid surface. In this sense, the deformation process of the droplet was measured only on the condition that it can not be disintegrated into many particles.

The period required for the droplet of 400 μm in diameter to rebound from the surface after the collision is only 1.0 ms or shorter. Therefore, it is difficult to follow the time-variation of the droplet deformation process, even though the high speed camera capable of taking 10000 frames/s is adopted. In addition, the droplet behavior is so susceptible to influences from a very small environmental change that it is uncontrollable by the adjustment of the experimental apparatus. Accordingly, the deformation process of the droplet impinging on the hot surface has been measured by a number of video images on the basis of the statistical procedure. The droplet images were exposed twice per frame by two flashes in a certain time interval to catch the variation of the droplet deformation process with time.

5.2 Experimental apparatus

Figure 5.1 shows a schematic diagram of the experimental apparatus by which the deformation process of a droplet impinging on a heated rigid surface beyond the Leidenfrost

temperature can be measured.

The water stored in a gastight tank is introduced to a needle and the droplet is formed through the needle. The water is pressurized statically by a high pressure air to ensure repeatability of droplet formation and release at the needle tip. The needle is flat tipped and set vertically. A uniformly spaced stream of droplets is generated with an almost equal diameter and velocity at the needle tip. Also, the adjustment of the spacing of droplets can be made in accord with the vibration frequency of a needle oscillator. A disk of 200 mm in diameter rotates horizontally between the needle exit and the heated surface. Only one droplet per revolution can pass through the slit hole of the rotating disk and reach the horizontal heated surface. The droplet size as well as the impinging velocity is easily changeable by the water pressure, the vibration frequency of the needle oscillator and the inner diameter of the needle. But, it is impossible to change only the droplet diameter on the condition of keeping the impinging velocity constant and the inverse is also impossible. By this experimental apparatus, droplets of 300 μm to 700 μm can be generated in the impinging velocity range between 1.2 m/s and 6.0 m/s.

The droplet falls vertically onto a 6 mm thick by 28 mm diameter Inconel alloy 625 test surface. The test surface temperature is measured by the chromel-alumel thermocouples and adjusted by the thermocontroller unit. Throughout the present paper, the surface temperature is fixed at 500 °C. But, it should be noted that the temperature change during the experiments is confirmed to be within plus or minus 20 °C.

The deformation process of the droplet is recorded by using a video camera which is equipped with a macro lens. The droplet images are exposed by the back light method using two micro flash units, which are scheduled to operate at a constant time interval. The first flash is adjusted to catch the droplet just before the collision with the surface. The flash timing is adjusted by using both an optical sensor perceiving the slit position on the disk and a delay timer. In the present experiments, the droplet is photographed in the range of the time interval from 100 μs to 1600 μs. The time interval of the two flash units can be set by a flash controller. The lightening period of the flash units is kept below 2 μs. The droplet image can be exposed only during flashing. The time variation of the droplet height and width during the deformation is recorded by many double exposure video images on the basis of the statistical procedure. The droplet diameter before reaching the heated surface can be directly measured from the video image. Also, the impinging velocity can easily be estimated from both the moving distance of the droplet and the time interval of the two flashes, as shown in Photo. 5.1(a). When the impinging velocity is measured, the both images of the same droplet photographed by the first and second flashes are required to be before the collision with the surface, and the time interval of two flashes is adjusted below 200 μs. The time order of two droplet images can be distinguished by two different color flashes. Photo. 5.1(a)~(d) is output by the monochrome video printer taken from the color images.

The resident time of the droplet during the deformation on the hot surface after the contact with it can be evaluated from the distance between the droplet and the surface in the first exposed image, the impinging velocity and the time interval of two flashes. Thereby, the height and the width of the droplet on the surface can be measured directly from the second exposed image. The droplet deformation process is pursued by a lot of droplet images, for example, as shown in Photo. 5.1(a) ~ (d). Here it should be noted
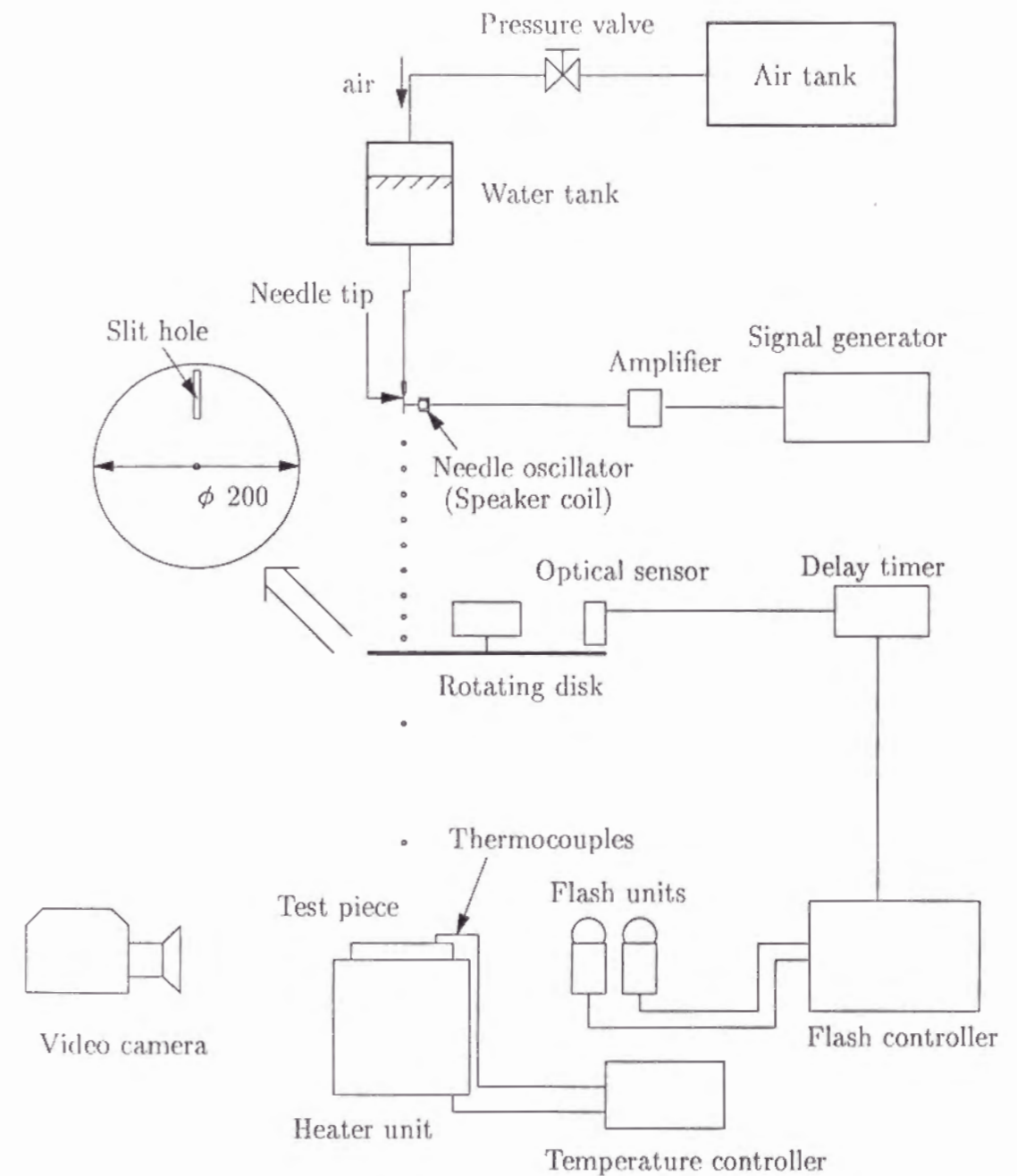

Figure 5.1: Schematic view of experimental apparatus.

that the flashing time intervals of Photo. 5.1(a) ~ (d) are different from each other, the time interval is 200 μs, 200 μs, 600 μs, 800 μs for Photo. 5.1(a), (b), (c) and (d), respectively. Again, the measurement accuracy determined by the resolution of the video image is within plus or minus 0.006 mm in the present measurement unit.

5.3 Results and discussion

First, the deformation and rebounding phenomena of the droplet after making contact with the hot surface beyond the Leidenfrost temperature have been inspected under the condition that the droplet size ranges from D_p=330 μm to 600 μm in diameter and the impact velocity is changed in the range from V_0=1.7 m/s to 5.7 m/s. The droplet and surface temperatures were kept at 20°C and 500°C, respectively. Figure 5.2 shows the rebounding and disintegrating cases with the Weber number We and Reynolds numbers Re as parameters on the V_0 vs. D_p diagram, where the solid circles correspond to the rebounding case and the empty ones denote the disintegrating case. It is noted that We as well as Re is represented by the physical properties at 20°C. There could be observed the droplets which break up into two pieces in air after rebounding and these were, of course, regarded as belonging to the rebounding group. The critical Weber number, which shows the boundary between rebounding and disintegrating, was proposed by some researchers in prior experimental investigations. Ueda et al.[2] gave 70 to the critical Weber number on the basis of the experimental results obtained on condition that the droplets of 1 mm to 3 mm in diameter fell on the flat stainless steel and copper surfaces heated at 300 °C.

Again, Shoji et al.[7] made an experimental study on condition that the droplets of 300 μm to 3530 μm impinge on the flat nickel surface heated in the temperature range from 300 °C to 800 °C and thereby proposed that the critical Weber number exists in the range between 80 and 90. According to the present experimental results, the critical Weber number is nearly 50 and relatively small in comparison with the above mentioned two investigations. We consider that the rebounding condition is influenced not only by the Weber number, but also by other parameters such as the surface temperature, the surface roughness and the surface material, etc.. As pointed out from an experimental point of view, the Leidenfrost temperature drastically changes with the surface material and roughness[10] and the boiling phenomenon of the droplet is also changeable depending upon such parameters.

Thus, on the basis of the present result, we tried to investigate the deformation behavior of the droplet on the Inconel alloy 625 surface heated at 500 °C in the range of We smaller than 50. Figure 5.3 shows the typical time history of the deformation process of the droplet after the collision with the surface under the experimental condition that D_p=0.46 mm and V_0=1.72 m/s (We=18.9 and Re=791). H, W and C denote the droplet height, the width and the distance between the droplet bottom and the surface after rebounding from the surface, respectively (see Figure 5.4). Here, it should be noted that H, W and C are non-dimensionalized by the initial spherical droplet diameter D_p and t is done by D_p/V_0. By the way, t=1 corresponds to 267 μs. Again, the variations of W, H and C with t in Figure 5.3 have been pursued by many video images of droplets, as has been mentioned already. In an early stage of $t < 0.8$, H decreases at the almost constant
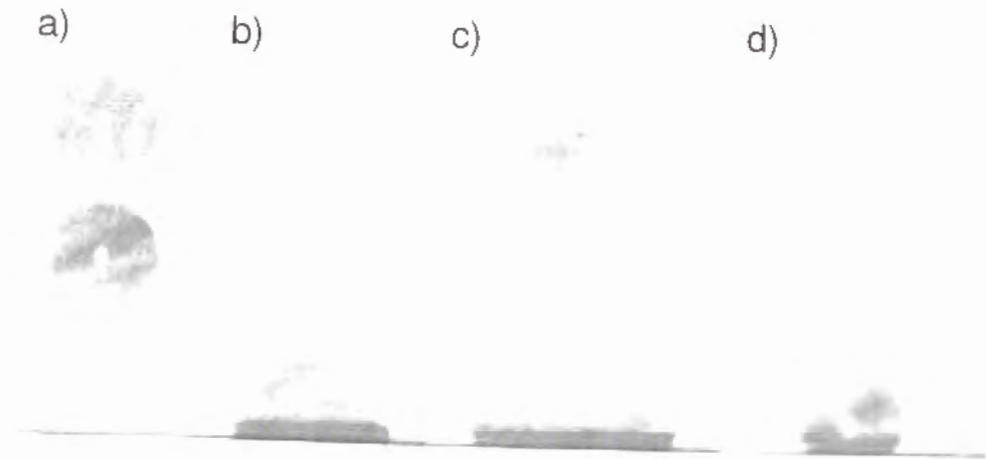

Photo. 5.1 : Droplet deformation process impinging on a plate using two flash units. Note that time interval of two flashes is 200 μs, 200 μs, 600 μs and 800 μs, for (a), (b), (c) and (d), respectively.
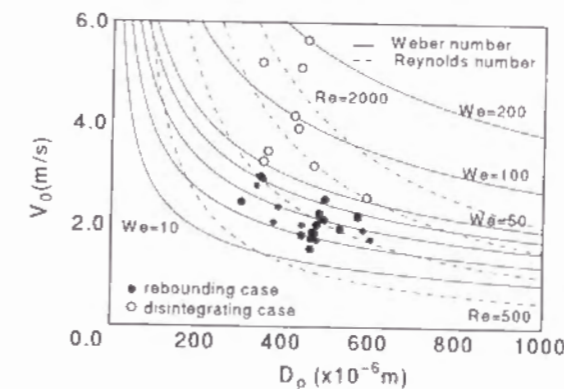

Figure 5.2: Rebounding and disintegrating cases with We and Re as parameters on V_0 and D_p relation.
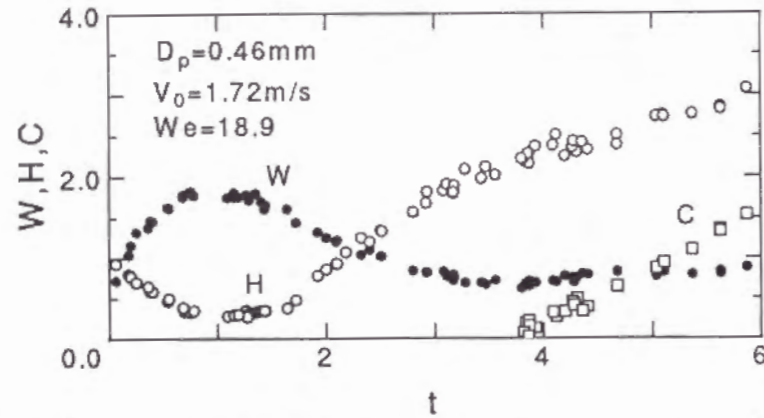
Figure 5.3: Time history of deformation process of droplet on condition that D_p=0.46 mm and V_0=1.72 m/s.
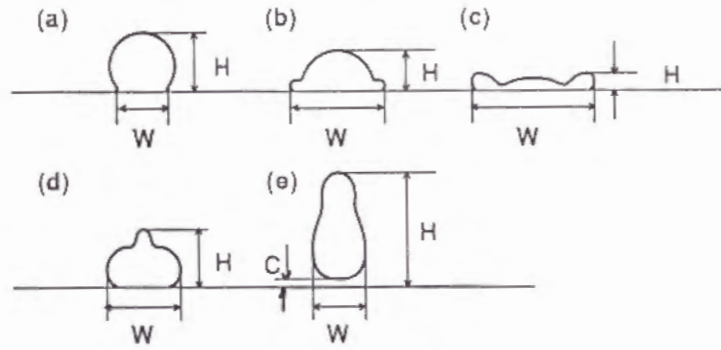

Figure 5.4: Definition of droplet height H, width W and distance C from bottom of droplet to plate surface after rebounding from surface.

rate which is equal to approximately the impact velocity, while W increases with time. After the droplet height H reaches the minimum value around t=1.0, its increasing rate is very slowly for a short time. After $t \simeq 1.7$ the increasing rate of H becomes remarkable suddenly. On the other hand, W reaches the maximum value around t=1.0 and thereafter continues to decrease. But, after $t \sim 3.5$, there is observed almost no notable change in W. Here, what is worthy of attention is that the droplet rebounds from the surface around t=3.8 when the droplet length $(=H - C)$ is approximately 2.2 times the initial droplet diameter D_p. However, the droplet tends to shorten as time elapses. It may be reasonable to consider that the upward velocity of the bottom side of the droplet becomes larger than that of the top side.

It should be noted that in a later stage after the collision with the surface the measured values tend to be scattered. This tendency becomes remarkable as the Weber number is increased. The major reason is due to the fact that most of droplets can not keep the shape axially symmetric when the droplets are lengthened as a bowling pin-shaped mass
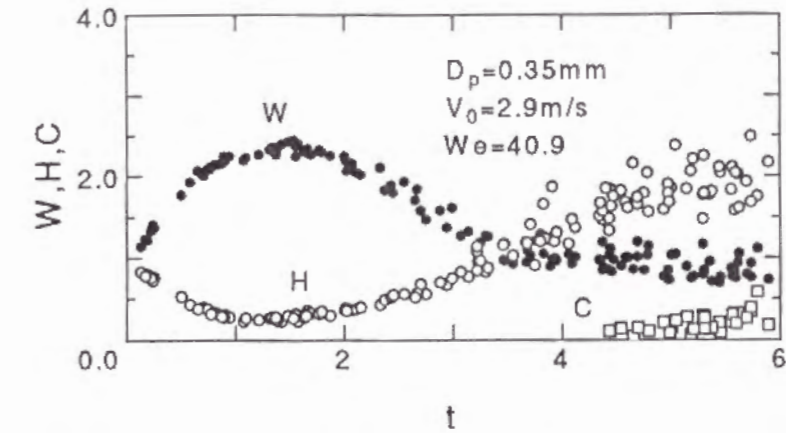

Figure 5.5: Time history of deformation process of droplet on condition that D_p=0.35 mm and V_0=2.9 m/s.

on the surface. Figure 5.5 indicates the time history of the deformation process of the droplet after the collision with the surface on condition that D_p=0.35 mm and V_0=2.9 m/s (We=41 and Re=1015). The dispersion of the measured values of W, H and C after rebounding from the surface becomes obviously remarkable compared with the case shown in Figure 5.3.

The maximum spreading diameter of droplets impinging on a high temperature surface was investigated experimentally by a few researchers. The empirical formulae were proposed in the form of the function of only the Weber number. Akao et al.[1] proposed the following form of

$$D_{max}/D_p = 0.613 We^{0.39} \tag{5.1}$$

and Ueda et al.[2] gave the following relation as

$$D_{max}/D_p = 0.87\left(\frac{We}{6} + 2\right)^{0.5} \tag{5.2}$$

The above two expressions were obtained using the relatively large droplets of the order of a few millimeters in diameter.

Figure 5.6(a) indicates the relation between D_{max}/D_p and We, where D_{max} denotes the maximum spreading diameter after the collision with the surface. The solid circles show the present experimental results obtained by using droplets of 330 μm to 600 μm in diameter. Also, the empty circles denote the results given by Ueda et al., which were obtained by using droplets of 0.94 mm to 2.5 mm in diameter at the saturation temperature of water. Therefore, the Weber number was estimated by the physical properties at 20 °C for the present case and at 100 °C for the case of Ueda et al..

The above mentioned two experimental formulae are found to give good agreement with each other in the range of the Weber number larger than 25. The present experimental data is also seen to be fairly close to these formulae, but the values are slightly small in comparison with the two formulae. Then, because it was considered that the maximum spreading diameter depends not only upon the Weber number, but also upon the
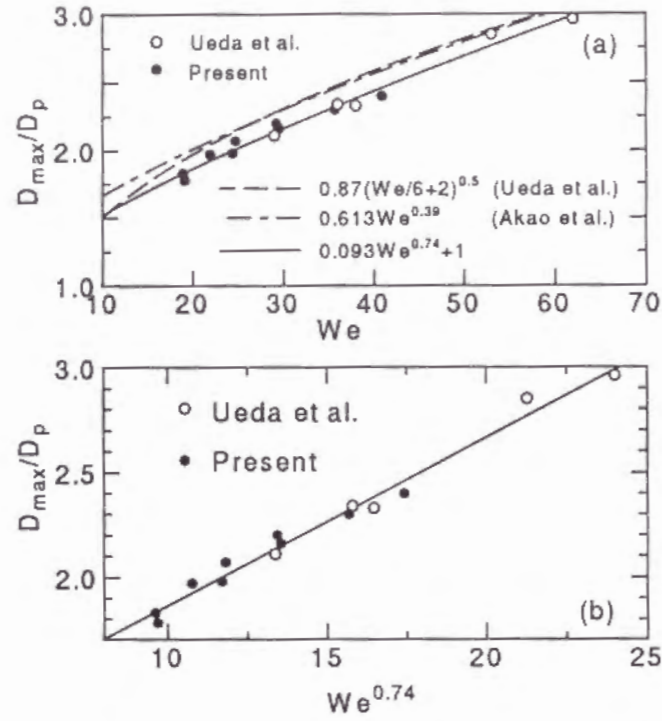
Figure 5.6: Relation between maximum spreading diameter after collision with surface and the Weber number(a). Comparison of formula built up in present study with measured values(b).

Reynolds number, the effect of the Reynolds number on D_{max} was inspected by plotting the value of D_{max} against the Reynolds number. As a result, almost no significant effect could be found. Then the formula capable of giving best-fit to the present experimental data was built up in the form of

$$D_{max}/D_p = 0.093We^{0.74} + 1 \qquad (5.3)$$

The numerical value obtained by the above expression could be found to give good agreement not only with the present data, but also with the results by Ueda et al.. Such a relation may evidently be understood in Figure 5.6(a) as well as 5.6(b).

Wachters et al.[3] and Ueda et al.[2] reported that the resident time of droplets on the hot surface is approximately equal to the first-order vibration period t of a freely oscillating droplet given in the form of

$$t = \frac{\pi}{4}\sqrt{\frac{\rho D_p^3}{\sigma}} \qquad (5.4)$$

in which ρ and σ denote the density and the surface tension, respectively. Shoji et al.[7] confirmed experimentally that Eq.(5.4) holds true for relatively small droplets of the order of 100 μm. Figure 5.7 gives the variation of the resident time with the droplet size. It was found that from this figure that the values obtained by Eq.(5.4) are in good agreement with the measured resident time of droplets in the size range of 0.33 mm to 0.48 mm. Concretely speaking, the resident time is estimated to be only 500 μs for D_p=0.3 mm and 1 ms for D_p=0.5 mm. It may be understood that as soon as the droplet impinges on the hot surface, it can be instantaneously in direct contact with the surface and after
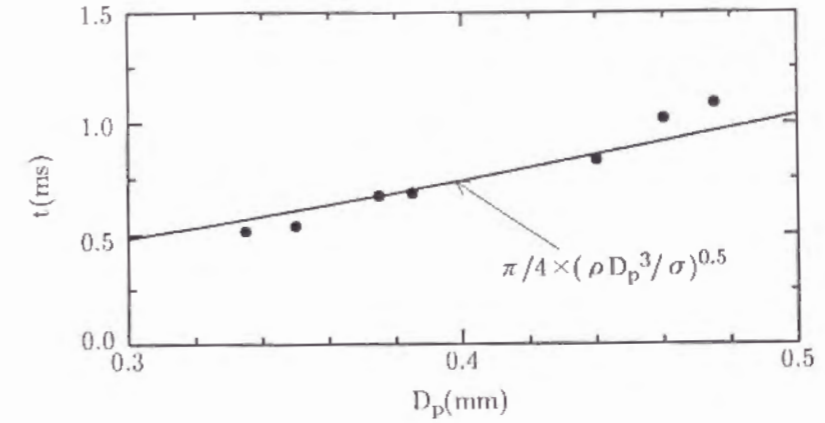

Figure 5.7: Variation of resident time with droplet size.

a very short wetting time the droplet is isolated from the surface through a vapour film. Therefore, it is very difficult to quantitatively assess the effect of the wetting on the cooling intensity from a thermal point of view.

Figure 5.8 shows the coefficient of restitution of droplets against the Weber number in the size range of D_p=0.33 mm to 0.48 mm. As droplets are not spherical in shape after impact on the surface, but lengthened as a bowling pin-shaped mass on rebounding from the surface, the rebounding coefficient e is defined in the form,

$$e = \left| \frac{0.5(V_{top} + V_{bottom})}{V_0} \right| \qquad (5.5)$$

in which V_{top} and V_{bottom} are the rebounding velocity at the top and bottom parts of the droplet, respectively. The velocities have been determined directly by following the variation of H and C with time at the moment when the droplet leaves the surface (see Fig. 5.3). It is understood from this figure that the coefficient is more than 0.5 in the range of We <18 and becomes small with the Weber number. There has been almost no measured records of the rebounding coefficient, so far as we know. Only Jeffrey & Patrick[9] measured it on condition that the water droplet of D_p=302 μm impinging on a steel surface heated at 400°C. They reported that the average rebounding velocity was 0.94 m/s for V_0=2.4 m/s. The measured result (e=0.392 at We=24) agrees well with the present experimental data, as shown in Figure 5.8. Finally, we wish to propose the empirical formula giving the relation between the coefficient of restitution and the Weber number as

$$e = 1 - 0.087We^{0.59} \qquad (5.6)$$

in the present experimental range. It is noted that the solid line drawn in Figure 5.8 obeys the above expression.
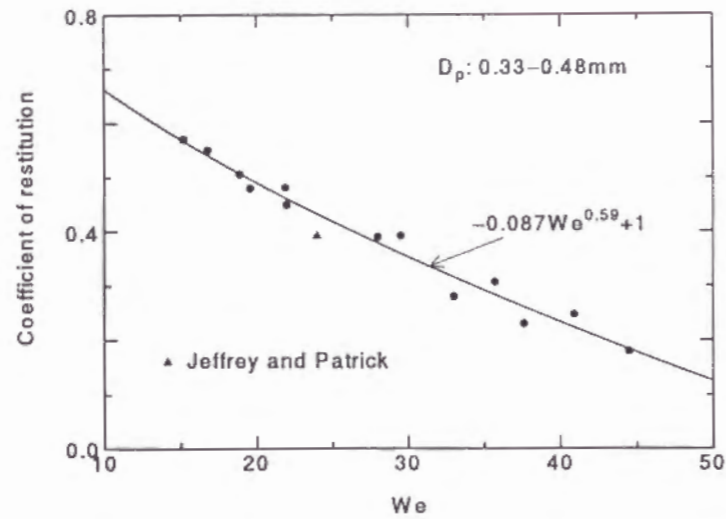
Figure 5.8: Coefficient of restitution of droplet against Weber number in size range of $D_p=0.33$ mm to 0.48 mm.

5.4 Conclusion

The deformation process as well as the rebounding one of water droplets from 300 μm to 600 μm in diameter impinging on the rigid surface heated at 500°C have been investigated experimentally. The impact velocity has been changed in the range from $V_0=1.7$ m/s to 5.7 m/s. The results obtained in the present study are summarized as follows:

1) The critical Weber number, which corresponds to the boundary whether the droplet breaks up on the surface or not, is nearly 50 in the present experiments and fairly small in comparison with prior experimental results proposed by a few researchers.

2) The maximum spreading diameter of droplets on the surface has been inspected. The present data has been found to give fairly good agreement with the results obtained by the prior two experimental formulae. But, the present data have been slightly small in comparison with two formulae (see Figure 5.6(a)). Accordingly, the formula capable of giving best-fit to the present data has been built up as a function of the Weber number. The value obtained by this formula has been found to be in good agreement not only with the present data, but also with the results by the other researchers (see Figure 5.6(b)).

3) The variation of the resident time of droplets on the surface with the droplet size has been confirmed to be in good agreement with the first-order vibration period of freely oscillating droplet.

4) The coefficient of restitution has been found to be more than 0.5 for $We<18$ and to decrease with the Weber number. Also, the empirical formula capable of predicting the coefficient of restitution in the range of $We<50$ has been proposed in the form of a function of the Weber number.

Reference

1. Akao, F., Araki, K., Mori, S. and Moriyama, A., Trans. ISIJ, 20(1980), p.737.

2. Ueda, T., Enomoto, T. and Kanetsuki, M., Bull. of JSME, 22(1979), p.724.

3. Wachters, L. H. J. and Westerling, N. A., Chem. Engg. Sci., 21(1966), p.1047.

4. Hatta, Fujimoto, H. and N., Ishii, R., ISIJ Int.,31-4(1991), p.342.

5. Hatta, N., Fujimoto, H. and Takuda, H., Applied Sci. Research, 50(1993), p.129.

6. Pedersen, C. O., Int. Heat Mass Transfer, 13(1970), p.369.

7. Shoji M., Wakunaga T. and Kodama K., JSME-B, 50-451(1984), p.716.

8. Xiong, T. Y. and Yuen, M. C., Int. J. Heat and Mass Transfer,34-7(1991), p.1881.

9. Jeffrey D. Naver and Patrick V. Farrell, SAE technical paper 930919,(1993).

10. Chandra, S. and Avedisian, C. T., Int. J. Heat Mass Transfer, 35-10(1992), p.2377.

11. Hatta, N., Fujimoto, H., Takuda, H., Kinoshita, K. and Takahashi, O., To be published in ISIJ Int.

Chapter 6

Deformation process of a water droplet impinging on a solid surface
[15]

6.1 Introduction

The process of cooling a high temperature surface with a water spray is widely used in iron- and steel-making industries. Specifically, the spray cooling method is applied to the secondary cooling zone in a continuous casting process. Also, the hot strip passing through the last finishing roll is cooled on a runout table from the austenitic finishing temperature to the coiling temperature. In this case, the upper strip surface is cooled by the laminar flow cooling method, while the lower surface is cooled by the water spray. Hence, the numerical analysis of the flow field of subsonic free jets of gas-particle mixtures composed of air and water droplets was performed[1]. Again, the problem of flow structures of the two-phase subsonic jet impinging on a flat plate normal to the flow, corresponding to the mist/spray cooling situation, was solved on the assumption that the droplets are perfectly elastically reflected from a surface by the present authors [2]. However, we cannot shed further light on the mist/spray cooling mechanism without understanding the deformation process of individual water droplets impinging on a plate surface.

Practically speaking, in spite of the widespread use of this cooling method, there seems to be a conspicuous lack of knowledge concerning the spray cooling mechanism. Therefore, many experimental studies have been performed focusing upon the collision and deformation processes of a water droplet impinging on a hot plate surface (Wachters and Westerling [3], Ueda et al. [4], Akao et al. [5] and Chandra & Avedisian[6]). However, the diameters of spherical water droplets adopted in the experiments are relatively large, ranging from 1mm to 3mm. This is because the high speed deformation process of the droplet must be observable from a photographic point of view. Actually the droplet diameters in spray cooling are believed to range from $100\mu m$ to $500\mu m$. In this regard, Pederson [7] treated relatively small droplets, from $200\mu m$ to $400\mu m$, but the photographs of the impact process are not sharp enough to allow an understanding of the detailed behaviour in the droplet deformation process. In passing, we note that it is impossible to experimentally measure the inner flow field of a droplet during and subsequent to the collision with a solid surface.

Again, there are a few reports concerning the numerical analyses of the collision and deformation processes of a liquid droplet impinging on the surface. Harlow and Shannon [8] analysed numerically the deformation process of a droplet impinging on a flat plate and compared the result obtained with the experimental data. Although the effect of the surface tension on the deformation process was neglected in their analysis, a fairly good agreement between the numerical and experimental results was found. Turutani et al. [9] studied the deformation process of the droplet using the SMAC method [10] and discussed the effect of surface tension by comparing the numerical results with the experimental values. The two results are found to quantitatively show a similar tendency on the whole. However, in the above mentioned two analytical studies, the surface configurations are not so sharp due to following the free surface by the so-called marker particles. Moreover, these numerical analyses were restricted to an earlier deformation process.

The deformation process of a n-heptane droplet on a stainless steel surface at room temperature was studied using a flash photography method by Chandra & Avedisian [11]. They found that a liquid film formed by the droplet impinging on a surface continued to spread monotonically in a fairly thin discoid-like shape and a maximum diameter of four times the initial droplet diameter. In the present experiment where a water droplet impinges on an Inconel 625 alloy surface, it has been found that the liquid shows the tendency to be stagnant at the periphery of the circular film and concentrates there in a doughnut-like shape, and that thereafter the liquid begins to flow backwards towards the center until it reaches an equilibrium configuration and is concentrated at the central region rather than at the periphery.

In the present chapter, both the radially expanding process of the liquid film formed by a droplet impinging on a solid surface at room temperature, and the subsequent process of flow reversal from the periphery of the circular liquid film towards the central region, have been investigated from numerical and experimental points of view. Concretely, the experimental results performed by the present authors and Chandra & Avedisian [11] have been analysed for a numerical point of view. The inner velocity vector fields as well as the above characteristic parameters have been calculated using an axisymmetric coordinate system. The surface tension effect is taken into consideration. The calculation approach is based on the MAC-type solution method. This need not introduce the so-called marker particles, which will be mentioned later. A comparison has been made between the calculated time histories of droplet diameter and height during the deformation, with corresponding experimental observations. In the present experiments, the time variation of the droplet diameter and its impinging velocity, are determined by direct measurement from multiple-exposure images using micro flash units.

6.2 Conservation equation

The conservation equations to be solved are expressed nondimensionally in terms of the following dimensionless variables.

$$t = \bar{t}/(\bar{D}_p/\bar{u}_0), \quad x = \bar{x}/\bar{D}_p, \quad y = \bar{y}/\bar{D}_p$$
$$u = \bar{u}/\bar{u}_0, \qquad v = \bar{v}/\bar{u}_0, \quad p = \bar{p}/(\bar{\rho}\bar{u}_0^2) \qquad (6.1)$$

in which t is the time; (x,y) denote the coordinates in the radial and axial directions, respectively; (u,v) denote the velocity components in the x- and y-directions, respectively; p is the pressure. $\bar{D}_p$, $\bar{u}_0$ and $\bar{\rho}$ denote the initial droplet diameter, the impinging velocity and the material density of droplet, respectively. Here, overbars denote the dimensional quantities.

The system of equations governing the droplet deformation is given by

$$\frac{\partial u}{\partial x} + \frac{\partial v}{\partial y} + \frac{u}{x} = 0 \qquad (6.2)$$

$$\frac{\partial u}{\partial t} + \frac{\partial u^2}{\partial x} + \frac{\partial uv}{\partial y} + \frac{u^2}{x} = -\frac{\partial p}{\partial x} + \frac{1}{Re}\left[\frac{\partial^2 u}{\partial x^2} + \frac{\partial^2 u}{\partial y^2} + \frac{\partial}{\partial x}\left(\frac{u}{x}\right)\right] \qquad (6.3)$$

$$\frac{\partial v}{\partial t} + \frac{\partial uv}{\partial x} + \frac{\partial v^2}{\partial y} + \frac{uv}{x} = -\frac{\partial p}{\partial y} - \frac{1}{Fr^2} + \frac{1}{Re}\left[\frac{\partial^2 v}{\partial x^2} + \frac{\partial^2 v}{\partial y^2} + \frac{1}{x}\frac{\partial v}{\partial x}\right] \qquad (6.4)$$

in which Re and Fr are the Reynolds number and the Froude number, respectively, defined as:

$$Re = \bar{u}_0 \cdot \bar{D}_p/\bar{\nu}, \qquad Fr = \bar{u}_0/\sqrt{\bar{g} \cdot \bar{D}_p} \qquad (6.5)$$

Here, $\bar{\nu}$ and $\bar{g}$ denote the kinematic viscosity and the gravitational acceleration, respectively.

Next, the pressure balance condition on the free surface yields:

$$p_s - p_\infty + \frac{1}{Re}\frac{\partial U_\eta}{\partial \eta} = \frac{1}{We}\left(\frac{1}{R_1} + \frac{1}{R_2}\right) \qquad (6.6)$$

in which:

$$We = \frac{\bar{\rho}\bar{u}_0^2 \bar{D}_p}{\bar{\sigma}} \qquad (6.7)$$

and p_s and p_∞ are the surface and atmospheric pressure, respectively. R_1 and R_2 are the principal radii of curvature at a given point on a free surface, respectively. η is the coordinate normal to the surface and U_η is the component of velocity in the η-direction. σ is the surface tension. Obviously, the sign of the left hand side of Eq.(6.6) depends upon the sign of R_1 and R_2, that is, whether a concave or convex surface.

6.3 Numerical procedure

The numerical technique suitable for solving free-boundary problems of fluid mechanics, can be divided roughly into two kinds of methods. One is the method to pursue the free surface on a steady coordinate system in a Lagrangian manner, based upon the MAC technique developed by Harlow and Welch [12], the other is to renew the curvilinear coordinate system so that the surfacial coordinates of fluid may fit the free surface boundary

at every new time step [13]. The use of the boundary-fitted curvilinear coordinate system is considered to be of advantage in treating the boundary condition at the free surface easily and strictly and in maintaining the conservation law of mass and momentum at the free boundary faithfully. However, computational cost is appreciably expensive in comparison with the steady coordinate system, because the adjustment must always be made so as to fit the current boundary shape. On the other hand, the numerical technique based on the MAC-type solution method is capable of catching the overturning of a free surface wave and the mixing bubbles in liquid, etc.. In the present investigation, the calculation of the deformation process of a droplet has been performed using the steady coordinate system, because the numerical instability has occurred due to the shape of the droplet just after the collision with the surface. Too large curvature at the free surface has occurred, although the boundary-fitted coordinate system has been tried.

The system of conservation equations has been numerically solved by the finite-differencing approximation of the Navier-Stokes equations governing an axisymmetric incompressible fluid flow. The staggered mesh system has been adopted in the numerical simulation. The second-order upwind scheme, which is commonly called the donor cell method, has been applied to the convection terms and the second-order central differencing scheme has been applied to the viscous terms. Also, the explicit Euler scheme has been adopted for time integrations. First, the velocity vector field has been determined by the finite-differencing approximations to the momentum equations(6.3) and (6.4). Next, the pressure field has been determined by solving the finite-differencing approximation of the Poisson equation on the basis of the iterative procedure. The calculation approach which has been mentioned so far, obeys basically the MAC-type solution method [12], except it uses no marker particles and applies the donor cell method to the convection terms.

Now, we briefly describe the calculating procedure of the free surface configuration. It is assumed that the free surface consists of a large number of segments and the two-end points of each segment are located on the underlying lines of the rectangular cell system. According to Miyata [14], the time evolution of the free surface is followed by the Lagrangian movement of the segments that form the free surface configuration. The end points (x_s^n, y_s^n) of the segments at a time step n, are moved to the new points (x_s^{n+1}, y_s^{n+1}) at the next time step in the Lagrangian manner:

$$x_s^{n+1} = x_s^n + \Delta t \cdot u_s$$
$$y_s^{n+1} = y_s^n + \Delta t \cdot v_s \qquad (6.8)$$

where u_s and v_s denote the velocity components in the radial and axial directions, respectively and Δt is the time increment per cycle. The new segments are temporarily determined by (x_s^{n+1}, y_s^{n+1}). Then, the new formal end-points are given by the intersecting points between the temporary segments and the underlying mesh lines. The submesh system, whose mesh size is half of the main system is introduced in the present calculation. Because the free surface configuration is represented by a succession of line segments, it becomes smoother due to the fact that the number of intersecting points increases to twice that of the main mesh system alone. It should be borne in mind that the calculation of the velocity vector and pressure fields is performed only on the main mesh system. Again, the radial position of the contact line of free surface on the plate is determined by the
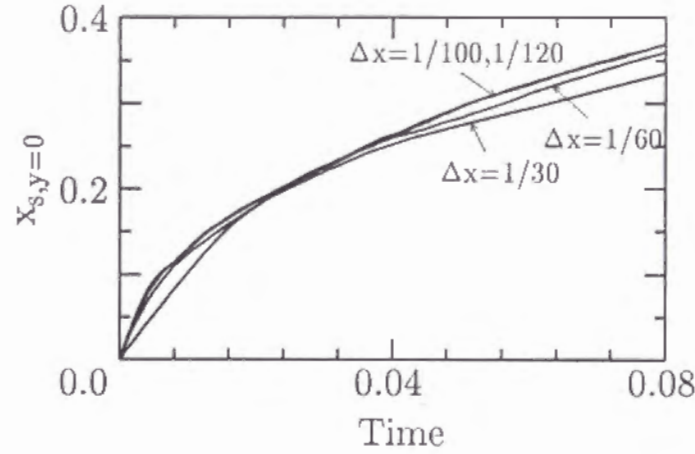
Figure 6.1: Preliminary check on effect of mesh size on numerical accuracy.

linear extrapolation from the two end points close to the solid surface.

In addition, the velocity components of the new segments are determined by the extrapolation from the velocity vector field in the nearest neighboring sites inside the fluid. Also, it is noted that the radii R_1 and R_2 required to estimate the surface pressure p_s (see Eq.(6.6)) are calculable by first and second-order differential terms and these are obtained by a second-order accurate difference approximation. There are some cases where it is impossible to calculate exactly the third term in the left hand side of Eq.(6.6), particularly at a sharply convex or concave region where the grid points are too small in number. Moreover, the term is considered to be negligibly small compared with the other terms in Eq.(6.6). Thereby, we note that this term is neglected.

In the present calculation, the moment of the impingement of droplet on a horizontally fixed flat surface has been set at $t=0$. It has been assumed that the droplet is perfectly spherical in shape and has no velocity distribution in its own body at $t=0$.

Next, we consider the effect of selecting the mesh size on the numerical accuracy. The regular square mesh($\Delta x = \Delta y$) has been adopted in this calculation. For various mesh sizes, the numerical experiments have been performed and the results have been compared with each other.

Figure 6.1 gives the time variation of the radial distance $x_{s,y=0}$ of the contact line of a droplet for $\Delta x = 1/30, 1/60, 1/100$ and $1/120$, respectively, on condition that Re=1500, We=62.5 and Fr=42.9. As a result, the numerical error has been found to be at most 1% between $\Delta x=1/100$ and $\Delta x=1/120$. Accordingly, $\Delta x=1/100$ has been selected in the present calculation for the sake of saving the computer memory and CPU time.

Again, the computational time interval Δt should be determined by the CFL(Courant-Friedrichs-Lewy) condition as follows;

$$\Delta t = f \times \text{Min} \left(\frac{\Delta x}{\sqrt{u^2 + v^2}} \right) \tag{6.9}$$

where f is the CFL number. The condition of $f \leq 0.5$ has to be satisfied because the submesh system is introduced in the present numerical model, as mentioned above.

The same numerical experiments as the above case have been performed for $f=0.07$, 0.05 and 0.04, respectively. As a result, almost no significant numerical error has been recognized between $f=0.05$ and 0.04. Accordingly, we select $f=0.05$ throughout the present simulations.

We wish to add previously that the no-slip condition is adopted ($u = v = 0$ at the wall) and the pressure condition at the solid/liquid interface is given by

$$p' = p_{1/2} - \frac{1}{2}v_1 |v_1| + \frac{\Delta y}{Fr^2} - \frac{2v_1}{Re \cdot \Delta y} \tag{6.10}$$

in which p' and $p_{1/2}$ denote the pressure at the external and the interior cells of the wall respectively, and v_1 is the velocity component normal to the wall.

6.4   Experimental procedure

The experimental study has been undertaken to understand the deformation process of impinging droplet on the plate surface. It is desirable to calculate the deformation process of a droplet for which the experimental data are available so that a direct comparison can be made.

Figure 6.2 shows a schematic diagram of the experimental apparatus. Water stored in a gastight tank is introduced to a needle and the droplet is formed through the needle. The water has been pressurized statically by a high pressure air to ensure repeatability of droplet formation and release at the needle tip of 0.2 mm in inner diameter. A needle oscillator using speaker coil, which vibrates with a particular frequency, has been attached to the needle tip so that droplets with a uniform diameter and a constant velocity may be produced. A 18cm diameter disk, which has a long and narrow rectangular hole (which will be called the slit hole hereafter), rotates horizontally between the needle tip and the solid surface. Accordingly, a large number of droplets appearing from the needle tip have been blocked by the rotating disk, but only one droplet per revolution can pass through the slit hole of the rotating disk and reach the flat surface.

The video camera recorder, which is equipped with a macro filter, has horizontally been fixed at the same level as the solid surface. The close-up image of the droplet on the video screen has been taken by the back light method using micro flash units. The video camera recorder, the solid surface on which the droplet impinges and micro flash lights have been arranged in a straight line. The optical sensor unit perceiving the position of the slit hole on the disk, sends a signal to the delay timer when a droplet is passing through the disk hole. The delay timer transmits a signal to the flash controller units (Sugawara SG303A, MP102A) with a delay time. The two micro flash units (Sugawara MP230) providing a 1.6 μs or shorter duration flash are triggered in a scheduled time intervals of 60~500 μs, when signals are sent from the flash controller units. Again, the error of the time interval is controlled below 1 μs. The video image has been set to be exposed only by the flash light. The moving distance of droplet during a flash is smaller than the measurement accuracy mentioned below.

The droplet size has been measured directly from a video still image using a personal computer. Again, because the measurement accuracy of the video still image depends upon the resolution of video system and the image magnitude, it can not be bettered
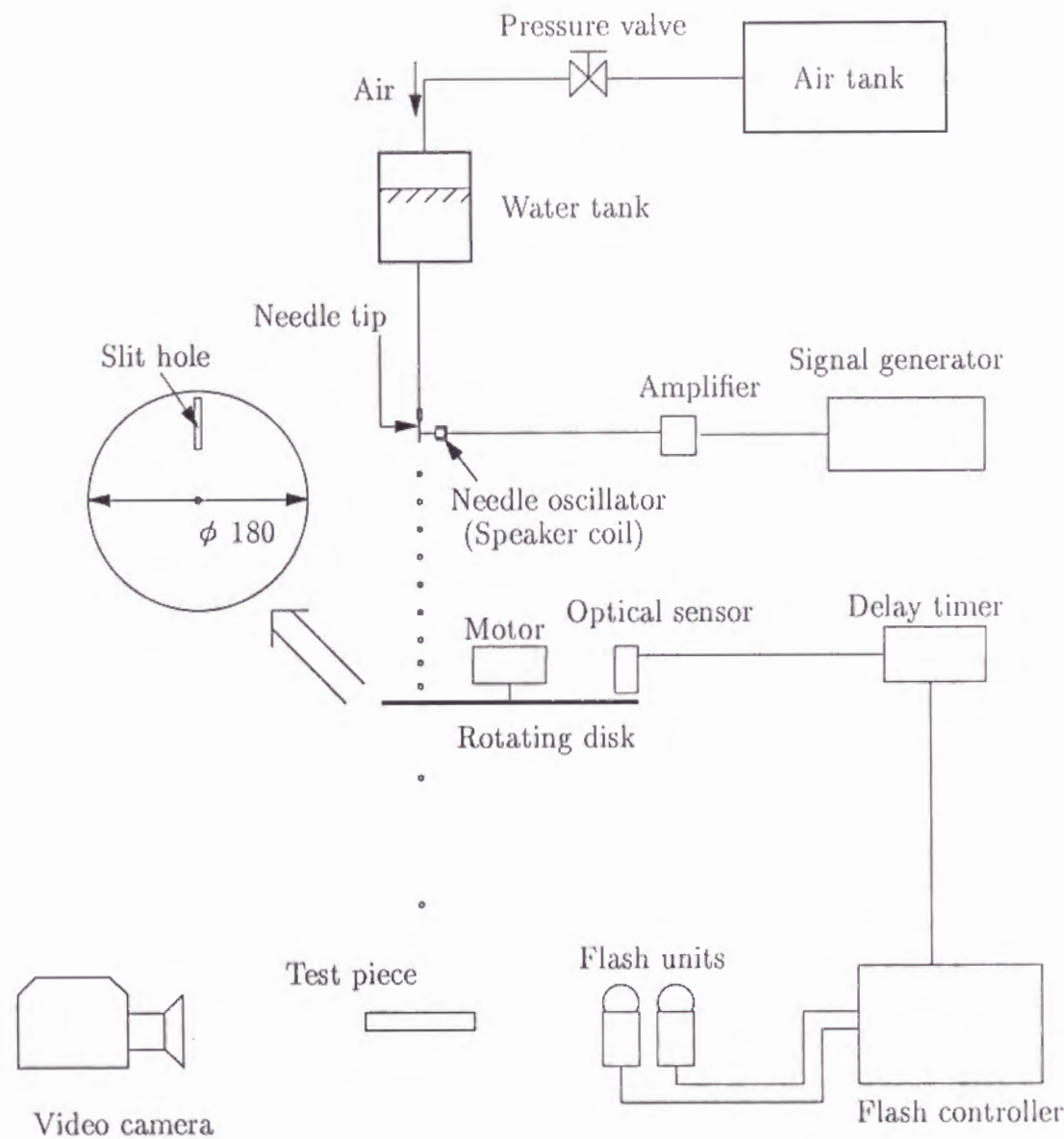
Figure 6.2: Experimental apparatus

than 0.008 mm in the present measurement system. The impinging velocity can be easily estimated by the moving distance of the droplet in the time interval from one flash to another. The time history of the droplet deformation has been measured from a lot of multi-exposure images of the droplet before the collision with the surface at the first flash and after the collision at the second flash. The period from the moment of impact to the second flash can be calculated from the three factors; the impinging velocity, the distance between the bottom/top of the droplet at the first flash and the surface, and the time interval between the two flashes.

Strictly speaking, it is difficult to always produce droplets with the same diameter and the same velocity with each other. Therefore, the diameter of all droplets on the video image has been measured to obtain the exact experimental data. Again, the impinging velocity can be regarded as constant on condition that the delay timer is set at the same delay time, because droplets with different velocities are not caught on a small video frame area. Incidentally, the velocity of droplet can be varied in the range from 1.3 m/s to 4.0 m/s in the present experimental apparatus.

6.5 Results and discussion

First, we consider the effect of the physical properties of the plate surface on the deformation process of droplets. The surface material is Inconel 625 alloy. In order to examine whether the effect of the physical properties of the surface is significant or otherwise, the deformation process of droplet impinging on the waxed plate surface has been compared with the case of the non-waxed(naked) plate surface on condition that $\bar{D}_p = 0.4$[mm] and $\bar{u}_0 = 3.75$[m/s] (Re=1500 and We=78). Figure 6.3(a) demonstrates the comparison between the two cases. We note that the height $\bar{h}$ and the radius $\bar{r}$ are normalized by the initial droplet diameter $\bar{D}_p$ and the dimensionless height $h(= \bar{h}/\bar{D}_p)$ and the dimensionless radius $r(= \bar{r}/\bar{D}_p)$ obey the definition shown in Figure 6.3(b). There is no observed difference in the time history of the height and the radius, at least, in the early period of impact. The deformation processes are similar to each other.

Also, the evolution of wetted area and spreading rate, both of a droplet on a stainless steel surface and of a droplet spreading over a thin film created by deposition of a prior droplet were compared with each other using a n-heptane droplet by Chandra & Avedisian [11]. The experimental results show that the deformation process of the droplet spreading on a thin liquid film is essentially the same as on a solid surface during the early period. Again, they found that the radius of the n-heptane film on the surface at the ambient temperature of 24 °C increases monotonically until it reaches a maximum.

However, it has been found in the present experiment using the water droplet that the film begins to recoil towards the center after the radius reaches a maximum on the solid surface at the ambient temperature, as described below. Practically, we believe that the interaction of the physical properties of the surface material with those of the liquid should be taken into consideration. In other words, the deformation process of a liquid droplet on a solid surface in the later stage after impact is considered to strongly depend upon a proper affinity at the solid/liquid interface, although the deformation process may be regarded as independent of the surface condition only during the early period of impact,
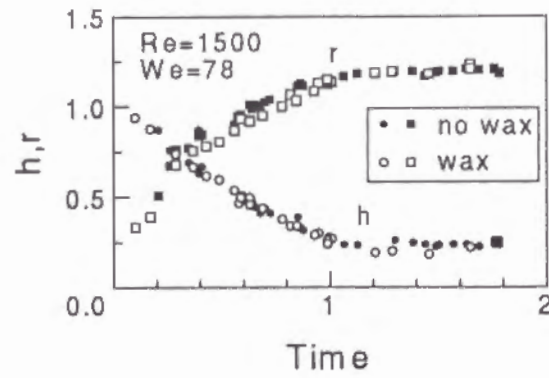
Figure 6.3: Effect of physical properties of plate surface on deformation process(a) and definition of droplet height h and radius r(b). Note that the experimental uncertainties in both the droplet radius r and height h are kept within $\pm$ 0.041 on a nondimensional scale.

as pointed out by Chandra & Avedisian.

However, the introduction of the above interaction effect into the numerical model is not taken into account in the present simulations, although the whole deformation process from the moment of impact to reaching the final configuration is not able to give appreciable agreement with the experimental data. At any rate, let us compare the numerical results obtained by the present model with the experimental ones for the case where a water droplet impinges on an Inconel 625 alloy surface. Figure 6.4(a) shows the comparison between the calculated and experimental time histories of the height h and the radius r on condition that $\bar{D}_p=0.5$[mm] and $\bar{u}_0=3.0$[m/s] (Re=1500 and We=62.5). It can be seen from this figure that the calculated time history of the reduction process of $h(= \bar{h}/\bar{D}_p)$ shown by the solid line gives fairly good fit to the experimental data by the solid circles. Also, the calculated time history of the spreading process of $r(= \bar{r}/\bar{D}_p)$ shown by the solid line is roughly in agreement with the experimental data by the empty circles. Strictly speaking, the calculated value is a little more than the experimental one, but the difference is at most 4% in the range of $t >0.5$. Figure 6.4(b) shows the time variation of the calculated liquid volume during the deformation due to the numerical error. Here, the initial spherical volume is fixed at unity. It may be regarded that the numerical error of the liquid volume is at most 3%. As mentioned above, it has been clarified that the calculated deformation process of the droplet is in agreement with the experimental in the early period of impact ($t < 1.5$). Then, the subsequent process is investigated. Figure 6.4(c) indicates the comparison between the calculated and experimental results in the period of $t < 5.0$ just after impact on condition that $\bar{D}_p= 0.39$ [mm] and $\bar{u}_0=2.25$ [m/s] ($Re=878$ and $We=27$). The calculated and experimental time variations of h and r have been found to agree well with each other in the time range of $t \leq 2.5$. However, a significant difference between the calculated and experimental results appears in the subsequent deformation process. The experimental r-value decreases because of the recoiling process in the time range of $t \geq 2.5$, while the calculated value remains almost unvaried. This may occur due to the fact that the no-slip condition is adopted at the liquid/solid interface as the boundary condition and thereby the contact line around the circular wetted area is

unmovable towards the center.

Now, we consider the deformation process and the flow field after the droplet impinges on the plate. Figure 6.5(a) gives the evolution of the free surface configuration and the velocity vector field on condition that Re=1500, We=62.5 and Fr=42.86. Figure 6.5(b) shows the distribution of pressure p on the solid surface. Here, $p = 0$ corresponds to the ambient pressure and the negative pressure corresponds to a lower than ambient pressure. It is noted that the magnitude of the velocity vector in this figure is comparable at every time stage. The water film radially expands in the early period of impact, because the pressure at the impinging region is higher than that at the peripheral region. The edge part in the neighbourhood of the contact line is observed to be roundish owing to the surface tension effect. The velocity boundary layer is formed in the thickness direction of the water film. This is due to the fact that the velocity components are set at zero at the liquid/solid interface in the no-slip condition. The calculated results show that the liquid flows radially from the center to the relatively stagnant edge zone of water film and the roundish edge zone expands in the early period of impact ($t<1.6$). As a result, the central part of the liquid film becomes lower than the height of the edge zone between $t=1.2$ and 1.6.

The film radius reaches a maximum value at $t\simeq1.6$ owing to the decrease in the radial velocity component, the fluid friction with the solid surface and the reversal of the pressure gradient in the radial direction. Thereafter, the liquid flows radially backwards from the edge part to the center. Such a reversal phenomenon of flowing direction is strongly governed by the vortical structure appearing at the roundish edge zone. The center of vortical structure formed first near the contact line, moves upwards. As a result, the edge zone moves in the radial direction ($t=1.2 \sim 1.6$). On the other hand, the flow towards the center on the underside of the edge zone is formed and comes into collision with another flow from the center towards the periphery. Finally, the collision of the two flows leads to a rising flow and thereby the roundish edge zone grows in both the thickness and the width($t=2.0 \sim2.4$). As the time elapses further, the flow towards the center becomes superior to the flow from the center towards the periphery. As a natural consequence, the position where the flow towards the central part collides with the opposite flow, is seen to shift towards the center with time. That is to say, the position where the liquid film thickens, is shifted from the peripheral region to the center. On the other hand, the central liquid film with a smaller and almost uniform thickness is seen to be in an almost stagnant state($t=2.0\sim 3.2$). Thereafter, the flow from the periphery to the center becomes dominant and again the central part of the liquid film is elevated. As a whole, the configuration of the water film in this state is high in the central zone and lower with increasing water film radius($t=6.0$).

Photo. 6.1(a) to (e) indicate the time variation of the deformation process on the same condition as the case of Figure 6.5. These have been obtained by a video printer taken from the video image. The droplets have been photographed from a slightly oblique and upper side of the plate surface and a flashlight is snapped once per droplet. Therefore, it should be noted that the droplets taken in each instantaneous photograph, are different from each other, that is to say, the same droplet has not been followed, but the various instantaneous behaviors of different droplets have been photographed and arranged in regular sequence. Also, the time elapsed after the collision of each droplet with the surface
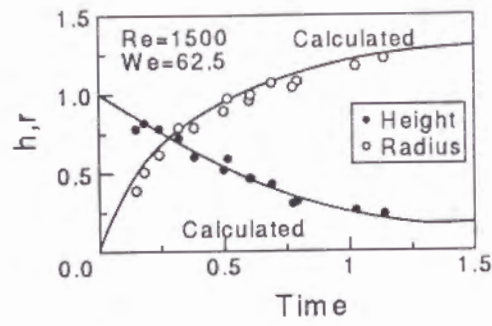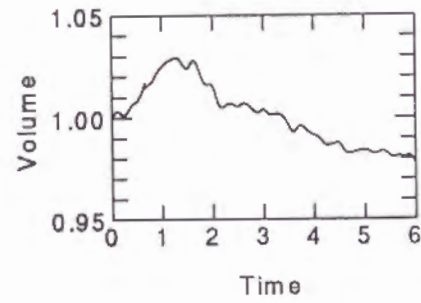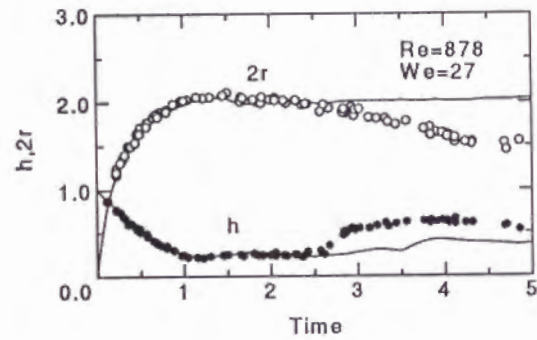
Fig. 6-4(a)

Fig. 6-4(b)

Fig. 6-4(c)

Figure 6.4: Comparison of numerical time histories of droplet height h and radius r with experimental values(a) and time history of numerical droplet volume during deformation(b) for Re=1500 and We=62.5. And comparison of numerical result and experimental ones for Re=878 and We=27(c). Note that the experimental uncertainties in both the droplet radius r and height h are kept ±0.041 on nondimensional scale in Fig. 6.4(a) and Fig. 6.4(c), and that the numerical error of the droplet volume during deformation is at most 3 % in Fig. 6.4(b).
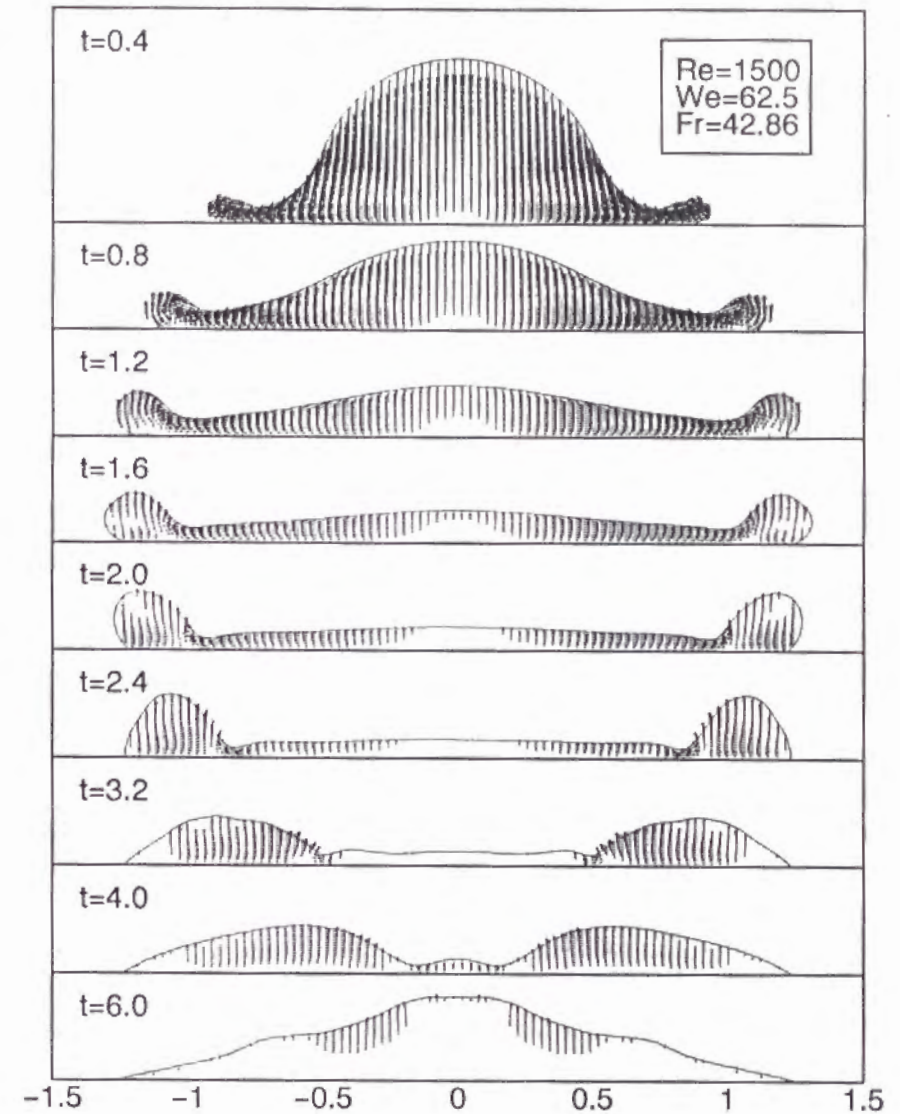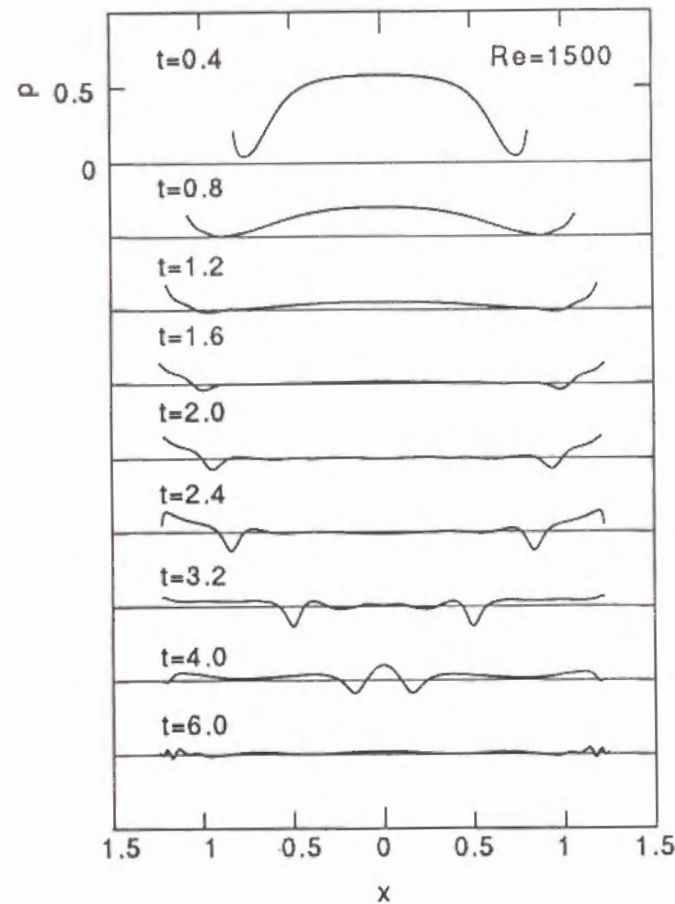

Fig. 6.5(a)

Fig. 6.5(b)

Figure 6.5: Numerical free surface configuration and velocity vector field of a droplet impinging on a flat plate(a) and pressure distribution along the surface (b) with Re=1500, We=62.5 and Fr=42.86.

could not be measured accurately due to being too short event. At any rate, it has been visually observed that droplets impinging on the solid surface form a radial liquid film and spread with time (see Photo. 6.1(a),(b) and(c)). Again, when the liquid film expands in a discoid-like form, the thickness of the central region, is seen to be smaller than that of the peripheral one, as shown in Photo. 6.1(d). Furthermore, it is observed in Photo. 6.1(e) that thereafter, flow reversal occurs from the peripheral region towards the central one. The last photograph is observed to be very similar to the shape of t=3.2 in Figure 6.5(a). On the whole, it may be justifiable to consider that these photographs indicate, at least, a qualitative agreement with the results obtained by the present numerical model, even if the values of t at which the pictures have been taken could not measured.

Here, it should be noted that there is observed a slight recoiling in the photographs. Really, in the experiments performed using the n-heptane droplet (Chandra & Avedisian [11]), there was no recoiling process on the stainless steel surface at the ambient temperature, while the recoiling process apparently exists in Figure 6.5(a). However, the surface wetted by liquid once cannot be regained to the dried state due to the fact that the no-slip condition is introduced at the liquid/solid interface, as mentioned above. In fact, the diameters of the circular contact lines are seen to be constant after reaching a maximum, as shown in Figure 6.5(a). Here, it should be noted that the maximum diameter of the liquid film is different from that of the circular wetted area.

Figure 6.6 indicates the influence of the impinging velocity on the time history of both the height h and the radius r during the deformation. We find that the height is reduced along the same time history curve up to $t \simeq 1.0$ in the present range of the Re number. Also, the height changes at the same rate in the range of $t<0.5$ regardless of the Re number and the decreasing rate is almost the same as the impinging velocity. After that, the decreasing rate becomes lower, but the droplet height begins to increase slightly at t=1.0, 1.2 and 1.3 for Re=1050, 1300 and 1500, respectively. This suggests that the height of the central part is lower than that of the peripheral zone (see Figure 6.5(a)). As the We number is reduced, the effect of the surface tension becomes more remarkable. Concretely speaking, the attainable radius is reduced and the time required to reach it is decreased with the decrease in the We number.

Next, we will discuss the experimental case where a n-heptane droplet of 1.5 mm in diameter impinges on the stainless steel surface at the ambient temperature of 24 °C. This corresponds to experiments performed by Chandra & Avedisian [11]. A sequence of photographs showing the deformation process of the droplet during and subsequent to the collision with the solid surface is reported in their paper. The first 2.6 ms of impact is shown during which period the droplet assumed the shape of a flattened disc. They states that the liquid continues to further spread after this time, reaching a maximum diameter of 6.04 mm at approximately 20 ms after making contact with the surface. This is four times the initial droplet diameter.

The maximum radius of the n-heptane film is significantly larger than that of the water film shown in the present investigation. Then, the calculation has been made on their experimental condition that We=43, Re=2300 and the impinging velocity $\bar{u}_0=0.93$ m/s. Figure 6.7 indicates the comparison between the experimental and calculated results. Here, solid circles denote their experimental data and solid lines denote the calculated results. Also, d denotes the diameter of the circular wetted area according to Chandra &

a)

b)

c)

d)

e)
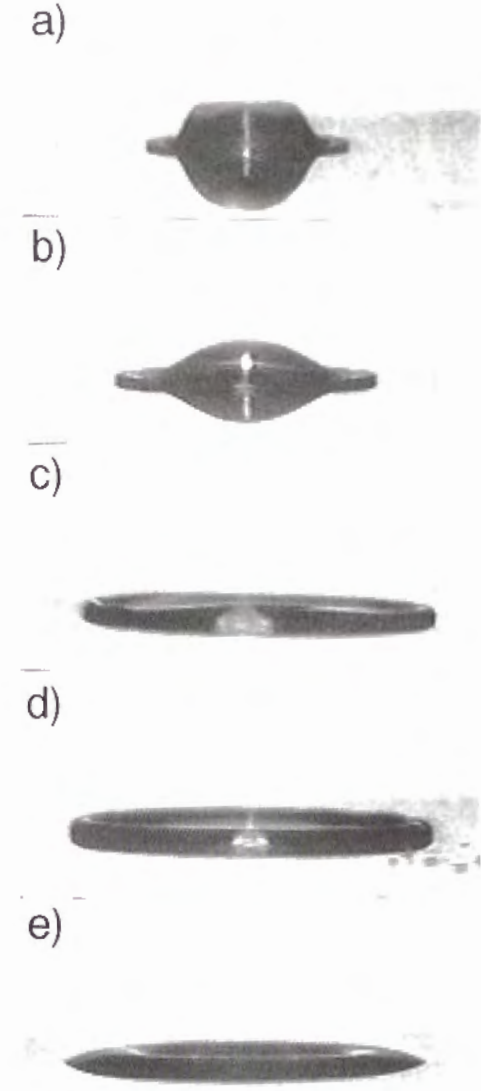
Photograph 6.1 : Deformation process of droplet impinging on a flat plate with $\bar{D}_p=0.5\pm0.02$ mm and $\bar{u}_0=3.0\pm0.02$ m/s.
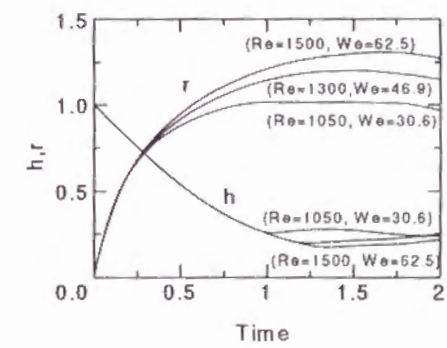
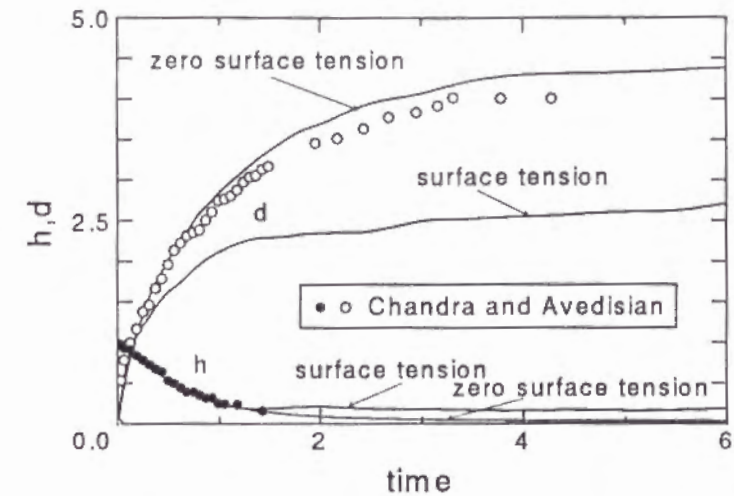Figure 6.6: Time history of numerical droplet height h and radius r impinging on a flat plate for various Re numbers.

Figure 6.7: Comparison between numerical and experimental results with Re=2300 and We=43. Note that solid circles give deformation process of n-heptane droplet observed by Chandra & Avedisian.

Avedisian [11]. The calculations have been made for the both cases where the effect of surface tension is taken into account and neglected. Comparing the two calculated values with the experimental data given by Chandra & Avedisian, the numerical results obtained by neglecting surface tension obviously give better agreement with the experimental data for the time variations of the height and diameter of liquid film during the deformation. In their experiment, the n-heptane film continues to spread monotonically until it reaches a maximum and the recoiling process is not observed. Therefore, we believe that the surface tension effect is very small not only during the early stage of impact, but also during the subsequent one, at least, at the surface temperature of 24 °C. In reality, the advancing liquid-solid contact angle at the contact line has been measured to be 32 deg. at 24 °C. Although the pictures in Photo. 6.1 show an evolution of the droplet very similar to that observed in Chandra & Avedisian's pictures for the case where a n-heptane droplet impinges on a steel plate at room temperature, the contact angle at the contact line of the former case is observed to be relatively large in comparison to that of the latter case. At any rate, the n-heptane liquid seems to be easily wet a stainless steel surface at the ambient temperature.

Figure 6.8 is a sequence of calculated surface configurations and the velocity vector fields showing the impact of a droplet of n-heptane on a stainless steel surface at 24 °C. Although the calculation is made on neglecting the surface tension effect, the surface configurations in this figure are very similar to those observed in Chandra & Avedisian's photographs [11]. The values of the time $\bar{t}$ shown in each figure correspond to those of $\bar{t}$ at which each picture was taken.

Furthermore, Akao et al. [5] showed that the spreading on the surface is basically independent of thermal effect since the maximum diameter correlates well the initial kinetic energy of the falling droplet. They proposed an empirical formula capable of predicting the value of the maximum dimensionless diameter for a case where a liquid

$\bar{t}=0.0$ ms

$\bar{t}=0.4$ ms

$\bar{t}=0.8$ ms

$\bar{t}=1.4$ ms

$\bar{t}=2.0$ ms

$\bar{t}=2.6$ ms

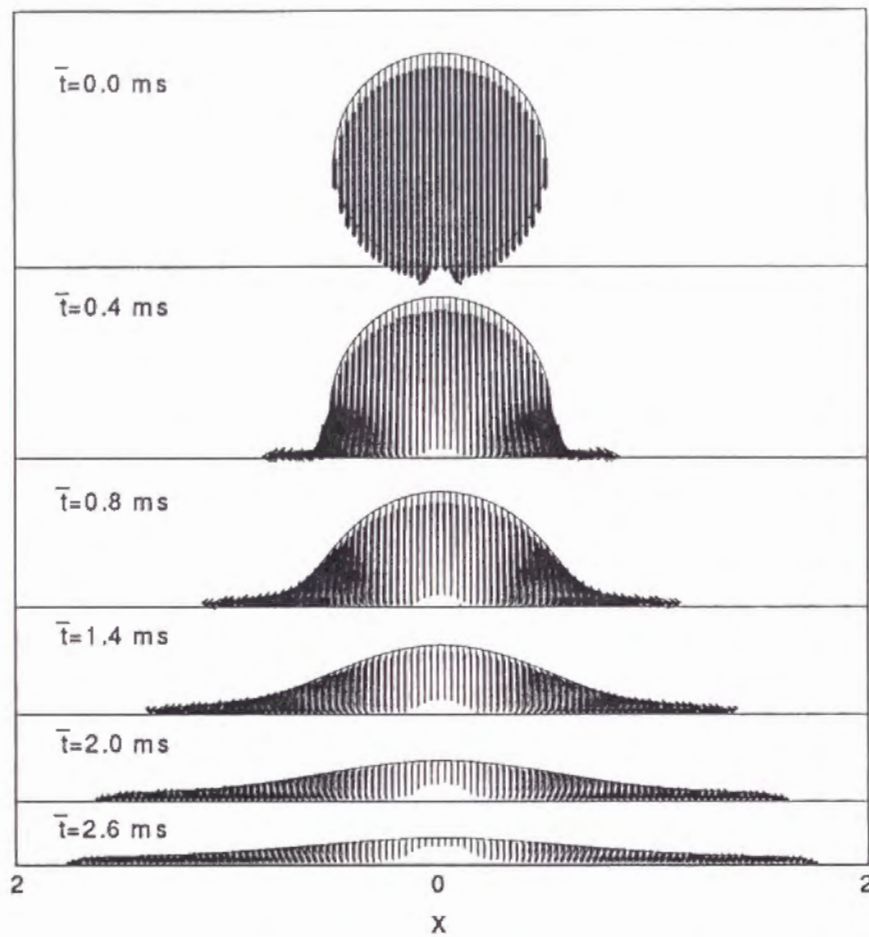2   0   2

X

Figure 6.8: A sequence of calculated surface configurations and velocity vector fields showing the impact of a droplet of n-heptane on a stainless steel surface.

droplet of 0.2 cm to 0.3 cm impinges on a copper surface heated at 400 °C. According to the formula, the value of the maximum dimensionless diameter must be 2.65 for the case where a value of four or more was given in the work made by Chandra & Avedisian. Again, the value must be 3.0 for the case where the result shown in Fig. 6.4(a) is 2.6 or so in the present calculation. In short, the experimental result of d given by Chandra & Avedisian is too large on the basis of this formula and the present results is small by 13 % or so.

As a result, the deformation process of a liquid droplet on a solid surface is considered to depend not only upon the Weber and the Reynolds numbers, but also upon the other parameters such as the initial kinetic energy of a droplet, the interaction of the physical properties of a liquid with those of a solid surface, the affinity at the solid/liquid interface etc..

6.6 Conclusion

The collision dynamics of a water droplet impinging on a rigid surface at room temperature have been described from numerical and experimental points of view. Emphasis is placed upon the analysis of the whole deformation process of a liquid droplet after the collision with the surface. The effects of viscous stresses and surface tension have been taken into consideration and the numerical model capable of predicting the deformation process has been built up. The results obtained by the model have been compared with the experimental data. First, the impingement of a water droplet on a Inconel 625 alloy surface at room temperature has been considered. It is found that the water film formed by a droplet impinging on the surface begins to recoil from the peripheral region towards the center after the radius reaches a maximum. It has been found that the calculated deformation process of the droplet is in agreement with the experimental in the early period of impact, but a significant difference between the calculated and experimental results appears in the subsequent deformation process. It is considered that this is due to the fact that the no-slip condition is adopted at the liquid/solid interface. Also, the impingement of a n-heptane droplet on a stainless steel surface at room temperature has been treated in the work performed by other researchers. It was confirmed experimentally that the n-heptane film formed by the impingement continues to spread monotonically up to an attainable radius and there is no recoiling process. The calculation has been made by the present authors for two cases where the surface tension effect is accounted for and is neglected. The numerical results obtained by neglecting the surface tension effect have been found to give fairly good agreement with the experimental data. The surface configurations have been found to be very similar to the photographs taken during the deformation at each time step.

From various points of view, it may be concluded that the deformation process of a liquid droplet on a solid surface cannot be determined only by the Weber and the Reynolds numbers, but the other parameters have to be considered. The problem concerning such parameters will be treated in the near future.

Finally, we believe that the present investigation represents a contribution to the physical understanding of the collision dynamics of a liquid droplet impinging on a solid

surface as well as dynamics of free surface bodies.

Reference

1. Hatta, N., Ishii, R. and Fujimoto, H., Transaction of ASME J. of Fluids Engg., 114(1992),p.420.

2. Hatta, N., Fujimoto, H. and Takuda, H.,Applied Scientific Research, 50(1993) ,p.129.

3. Wachters, L. H. J. and Westerling, N. A., Chem. Engg. Sci., 21(1966) ,p.1047.

4. Ueda, T., Enomoto, T. and Kanetsuki, M., Bull. of JSME, 22(1979), p.724.

5. Akao, F., Araki, K., Mori, S. and Moriyama, Trans. ISIJ, 20(1980), p.737.

6. Chandra, S. and Avedisian, C. T., Int. J. Heat Mass Transfer, 35-10(1992), p.2377.

7. Pedersen, C. O., Int. Heat Mass Transfeer, 13(1970), p.369.

8. Harlow, F. H. and Shannon J. P., J. Applied Physics, 38(1967), p.3855.

9. Turutani, K., Yao M., Senda J. and Fujimoto H., JSME-B, 55(1989), p.814.

10. Amsden, A. A. and Harlow, F. H., Los Alamos Scientific Report LA-4370,(1970).

11. Chandra, S. and Avedisian, C. T., Proc. R. Soc. Lond. A, 432(1991), p.13.

12. Harlow, F. H. and Welch, J. E., Physics of Fluids, 8(1965), p.2182.

13. Ryskin, G. and Leal L. G., J. of Fluid Mech., 148(1984), p.1.

14. Miyata, H., J. Compu. Physics, 65(1986), p.179.

15. Hatta, N., Fujimoto, H. and Takuda, H., To be published in ASME J. Fluids Engg.

Chapter 7

Deformation and rebounding processes of a water droplet impinging on a flat surface above Leidenfrost temperature

7.1 Introduction

The process of cooling a high temperature surface with a water spray or a mist flow is extensively used in iron and steel-making industries. Specifically, these cooling methods are applied to the secondary cooling zone in a continuous casting process. Then, the numerical analysis of the flow field of subsonic free jets of gas-particle mixtures composed of air and water droplets was performed to predict the cooling zone [1]. Again, the problem of flow structures of the two-phase subsonic free jets impinging on a flat solid surface normal to the flow, corresponding to the mist/spray cooling situation, was solved on the assumption that the droplets are reflected perfectly elastically from the surface [2].

However, there seems to be a conspicuous lack of knowledge concerning the detailed cooling mechanism. To evaluate spray/mist cooling heat transfer, it is indispensable to understand the collision dynamics of liquid droplets on a hot rigid surface systematically. So far, experimental investigations on the deformation behavior of a droplet impinging on a hot surface have been performed by many researchers. It was clarified by some prior studies that the phenomenon to be expected is strongly governed by both the initial kinetic energy of the droplet and the temperature of the surface. When the droplet has low Weber numbers corresponding to a low impact energy, the droplet spreads as a lens-shaped mass on the solid surface above the Leidenfrost temperature and thereafter rebounds as a bowling-pin shaped mass from the surface. While for higher Weber numbers the droplets shatter during the deformation process [3,4]. Also, the detailed deformation process of a liquid droplet on a hot solid surface was studied using a photographic method by Akao et al. [5], Chandra & Avedisian [6] and Xiong & Yuen [7]. On the basis of these photographic observations of the low Weber number case, the liquid film formed by the droplet impinging on the surface spreads radially until it reaches a maximum. After the end of the spreading, the liquid begins to flow backwards from the peripheral

region towards the center and then swelling in the central region becomes more and more remarkable. Finally, the liquid drop rebounds as a bowling-pin shaped mass from the surface.

However, it seems that the deformation process of the droplet as well as the driving force of the rebounding from the surface has not yet been clarified, in detail, from analytical as well as experimental aspects. Hence, we have investigated the effect of surface tension on the driving force of flow reversal from the periphery of the circular liquid film towards the central region, and of rebounding of the liquid drop from the surface from the viewpoint of the numerical analysis. This process of the approach is outlined as follows: The inner pressure in the periphery of the liquid film subject to deformation by the impact energy of the droplet can be considered to be much higher than that in the central region. This is because the radius of curvature is remarkably smaller in the periphery than in the central region. Therefore, the flow reversal is induced owing to the pressure difference. This leads to the recoiling process of the liquid film. Even when the central region of the film commences to swell, the recoiling continues to occur due to the fact that the curvature is still larger at the periphery. Subsequently, the center part of the liquid drop continues to elongate upwards. Finally the preceding liquid at the top of the convexity, which has a large upward velocity component, pulls up the bottom part of the remaining liquid on the surface and then the droplet rebounds from the surface.

The swelling process in the central region, occurring as the result of the recoiling process, has been confirmed to occur also for the case where a droplet impinges on a surface at room temperature, although it is not so remarkable [8]. When the surface temperature is kept above the Leidenfrost point, the swelling phenomenon is considered to be more and more noticeable. This is based upon the following two reasons. First, there is no friction at the liquid/solid interface owing to the formation of vapor film. Second, the viscous effect becomes weak owing to the temperature rise. The effect of the above two phenomena gives a tendency to reduce the energy loss of the liquid after making contact with the hot surface in comparison with the room temperature condition.

In the present investigation, the validity of the foregoing hypothesis has been examined by numerical experiments. In order to inspect whether or otherwise the droplet rebounds from the surface only by the surface tension effect, the numerical analysis of the flow field inside the liquid drop has been performed neglecting the thermal effect such as the vapor pressure, the temperature distribution, etc.. Also, the numerical results obtained by the present numerical model have been compared with the experimental data and discussed from a practical point of view.

7.2 Conservation equations

It is assumed that the flow fields obey the axisymmetric Navier-Stokes equations governing incompressible viscous flows. The equations to be solved are expressed nondimensionally in terms of the following dimensionless variables:

$$
\left.
\begin{array}{ll}
t = \bar{t}/(\bar{D}_p/\bar{u}_0), & x = \bar{x}/\bar{D}_p, \quad y = \bar{y}/\bar{D}_p, \\
u = \bar{u}/\bar{u}_0, & v = \bar{v}/\bar{u}_0, \quad p = \bar{p}/(\bar{\rho}\bar{u}_0^2)
\end{array}
\right\}
\tag{7.1}
$$

in which t is the time; (x,y) denote the coordinates in the radial and axial directions, respectively; (u,v) denote the velocity components in the x- and y-directions, respectively; p is the pressure. $\bar{D}_p$, $\bar{u}_0$ and $\bar{\rho}$ denote the initial droplet diameter, the impinging velocity and the material density of droplet, respectively. Here, overbars denote the dimensional quantities.

Also, the Reynolds number Re, the Weber number We and the Froude number Fr are defined as

$$
\mathrm{Re} = \frac{\bar{u}_0 \bar{D}_p}{\bar{\nu}}, \qquad \mathrm{We} = \frac{\bar{\rho}\bar{u}_0^2 \bar{D}_p}{\bar{\sigma}}, \qquad \mathrm{Fr} = \frac{\bar{u}_0}{\sqrt{\bar{g}\cdot\bar{D}_p}}
\tag{7.2}
$$

Here, $\bar{\nu}$ and $\bar{g}$ denote the kinematic viscosity and the gravitational acceleration, respectively; $\bar{\sigma}$ is the surface tension.

The system of equations governing the droplet deformation is given by

$$
\frac{\partial u}{\partial x} + \frac{\partial v}{\partial y} + \frac{u}{x} = 0
\tag{7.3}
$$

$$
\frac{\partial u}{\partial t} + \frac{\partial u^2}{\partial x} + \frac{\partial uv}{\partial y} + \frac{u^2}{x} = -\frac{\partial p}{\partial x} + \frac{1}{\mathrm{Re}}\left[\frac{\partial^2 u}{\partial x^2} + \frac{\partial^2 u}{\partial y^2} + \frac{\partial}{\partial x}\left(\frac{u}{x}\right)\right]
\tag{7.4}
$$

$$
\frac{\partial v}{\partial t} + \frac{\partial uv}{\partial x} + \frac{\partial v^2}{\partial y} + \frac{uv}{x} = -\frac{\partial p}{\partial y} - \frac{1}{\mathrm{Fr}^2} + \frac{1}{\mathrm{Re}}\left[\frac{\partial^2 v}{\partial x^2} + \frac{\partial^2 v}{\partial y^2} + \frac{1}{x}\frac{\partial v}{\partial x}\right]
\tag{7.5}
$$

Next, the pressure balance condition on the free surface is given by

$$
p_s - p_\infty + \frac{1}{Re}\frac{\partial U_\eta}{\partial \eta} = \frac{1}{\mathrm{We}}\left(\frac{1}{R_1} + \frac{1}{R_2}\right)
\tag{7.6}
$$

in which p_s and p_∞ are the surface pressure and the atmospheric one, respectively. R_1 and R_2 are the principal radii of curvature at a given point on a free surface, respectively. η is the coordinate normal to the surface and U_η is the component of velocity in the η-direction.

7.3 Numerical procedure

The deformation and rebounding processes of a droplet on a heated solid surface are basically solved by the same method as shown in the previous chapter. Namely, the simulation of the deformation and rebounding processes on the hot surface is performed using the MAC-type solution method to solve a finite-differencing approximation of the Navier-Stokes equations governing an axisymmetric incompressible fluid flow. The so-called staggered mesh system is adopted in the present numerical simulation. The second-order accurate upwind scheme, which is commonly known as the donor cell method, is applied to the convection terms and second-order accurate central differencing scheme is applied to the viscous terms. Also, the explicit Euler scheme is adopted for time integrations.

Now, let us describe briefly the calculating procedure of the free surface configuration. It is assumed that the free surface consists of a large number of segments and the two-end points of each segment are located on the underlying lines of the rectangular cell system [9]. The time evolution of the free surface is pursued by the Lagrangian movement of the segments that form the free surface configuration. Here, it is worthy to note that the submesh system, whose mesh size is half of the main system, is introduced in the present calculation. Because the free surface configuration is represented by a succession of line segments, it becomes smoother due to the fact that the number of the intersecting points between the segments and the underlying mesh lines increases to twice that of the main mesh system alone. It should be borne in mind that the calculation of the velocity vector and pressure fields, is performed only on the main mesh system.

Next, the value of pressure on the free surface is calculated, based on Eq.(7.6). However, the third term in the left hand side of Eq.(7.6) is neglected because there are some cases where it is impossible to calculate exactly this term, particularly at a sharply concave/convex region. The radii R_1 and R_2 of curvature on the free surface are calculated by first and second-order differential terms and these are obtained by a second-order accurate central difference approximation, where the calculating point of R_1 and R_2 and the two fourth intersecting points from there on the both sides are taken into account. The reason why not the nearest neighboring points of the calculating point, but the fourth points from there are selected is due to protecting the numerical instability.

The first and second order differential terms are given by

$$\frac{dy}{dx} = \left(\frac{dy}{d\xi}\right) / \left(\frac{dx}{d\xi}\right) \tag{7.7}$$

$$\frac{d^2y}{dx^2} = \left(\frac{dx}{d\xi}\frac{d^2y}{d\xi^2} - \frac{d^2x}{d\xi^2}\frac{dy}{d\xi}\right) / \left(\frac{dx}{d\xi}\right)^3 \tag{7.8}$$

in which we put $x = x(\xi)$ and $y = y(\xi)$. Here, ξ indicates the length from the central axis to a given point along the configuration of free surface. Let us consider the Taylor expansion at the two points $\xi = \xi + \Delta\xi_1$ and $\xi = \xi - \Delta\xi_2$ ($\Delta\xi_1 > 0$ and $\Delta\xi_2 > 0$) on the surface by neglecting the terms after the second order differential one.

$$\begin{aligned}
x(\xi + \Delta\xi_1) &= x(\xi) + \Delta\xi_1 x'(\xi) + \frac{\Delta\xi_1{}^2}{2}x''(\xi) \\
x(\xi - \Delta\xi_2) &= x(\xi) - \Delta\xi_2 x'(\xi) + \frac{\Delta\xi_2{}^2}{2}x''(\xi) \\
y(\xi + \Delta\xi_1) &= y(\xi) + \Delta\xi_1 y'(\xi) + \frac{\Delta\xi_1{}^2}{2}y''(\xi) \\
y(\xi - \Delta\xi_2) &= y(\xi) - \Delta\xi_2 y'(\xi) + \frac{\Delta\xi_2{}^2}{2}y''(\xi)
\end{aligned} \tag{7.9}$$

Then, we have

$$\begin{aligned}
x'(\xi) &= \frac{\Delta\xi_2{}^2 x(\xi+\Delta\xi_1)-(\Delta\xi_2{}^2-\Delta\xi_1{}^2)x(\xi)-\Delta\xi_1{}^2 x(\xi-\Delta\xi_2)}{\Delta\xi_1\Delta\xi_2(\Delta\xi_1+\Delta\xi_2)} \\
x''(\xi) &= \frac{\Delta\xi_2 x(\xi+\Delta\xi_1)-(\Delta\xi_1+\Delta\xi_2)x(\xi)+\Delta\xi_1 x(\xi-\Delta\xi_2)}{\frac{1}{2}\Delta\xi_1\Delta\xi_2(\Delta\xi_1+\Delta\xi_2)} \\
y'(\xi) &= \frac{\Delta\xi_2{}^2 y(\xi+\Delta\xi_1)-(\Delta\xi_2{}^2-\Delta\xi_1{}^2)y(\xi)-\Delta\xi_1{}^2 y(\xi-\Delta\xi_2)}{\Delta\xi_1\Delta\xi_2(\Delta\xi_1+\Delta\xi_2)} \\
y''(\xi) &= \frac{\Delta\xi_2 y(\xi+\Delta\xi_1)-(\Delta\xi_1+\Delta\xi_2)y(\xi)+\Delta\xi_1 y(\xi-\Delta\xi_2)}{\frac{1}{2}\Delta\xi_1\Delta\xi_2(\Delta\xi_1+\Delta\xi_2)}
\end{aligned} \tag{7.10}$$

for the central differential approximations. Also, the one-sided differential approximation is adopted in the neighborhood of contact line. Let us consider the Taylor expansion at the two points $\xi = \xi - \Delta\xi_1$ and $\xi = \xi - \Delta\xi_2$ ($\Delta\xi_1 > 0$ and $\Delta\xi_2 > 0$)

$$\begin{aligned}
x(\xi + \Delta\xi_1) &= x(\xi) - \Delta\xi_1 x'(\xi) + \frac{\Delta\xi_1{}^2}{2}x''(\xi) \\
x(\xi - \Delta\xi_2) &= x(\xi) - \Delta\xi_2 x'(\xi) + \frac{\Delta\xi_2{}^2}{2}x''(\xi) \\
y(\xi + \Delta\xi_1) &= y(\xi) - \Delta\xi_1 y'(\xi) + \frac{\Delta\xi_1{}^2}{2}y''(\xi) \\
y(\xi - \Delta\xi_2) &= y(\xi) - \Delta\xi_2 y'(\xi) + \frac{\Delta\xi_2{}^2}{2}y''(\xi)
\end{aligned} \tag{7.11}$$

Then, we have

$$\begin{aligned}
x'(\xi) &= \frac{\Delta\xi_2{}^2 x(\xi-\Delta\xi_1)-(\Delta\xi_2{}^2-\Delta\xi_1{}^2)x(\xi)-\Delta\xi_1{}^2 x(\xi-\Delta\xi_2)}{\Delta\xi_1\Delta\xi_2(\Delta\xi_1-\Delta\xi_2)} \\
x''(\xi) &= \frac{\Delta\xi_2 x(\xi-\Delta\xi_1)-(\Delta\xi_2-\Delta\xi_1)x(\xi)-\Delta\xi_1 x(\xi-\Delta\xi_2)}{\frac{1}{2}\Delta\xi_1\Delta\xi_2(\Delta\xi_1-\Delta\xi_2)} \\
y'(\xi) &= \frac{\Delta\xi_2{}^2 y(\xi-\Delta\xi_1)-(\Delta\xi_2{}^2-\Delta\xi_1{}^2)y(\xi)-\Delta\xi_1{}^2 y(\xi-\Delta\xi_2)}{\Delta\xi_1\Delta\xi_2(\Delta\xi_1-\Delta\xi_2)} \\
y''(\xi) &= \frac{\Delta\xi_2 y(\xi-\Delta\xi_1)-(\Delta\xi_2-\Delta\xi_1)y(\xi)-\Delta\xi_1 y(\xi-\Delta\xi_2)}{\frac{1}{2}\Delta\xi_1\Delta\xi_2(\Delta\xi_1-\Delta\xi_2)}
\end{aligned} \tag{7.12}$$

for the one-sided differential approximations.

A droplet impinging on a surface above the Leidenfrost temperature makes instantaneously direct contact with it and the temperature inside the drop abruptly rises through heat transfer from the surface. The film boiling occurs at the liquid/solid interface and the liquid drop is insulated with the surface through a vapor film. This process is introduced into the numerical model by changing the velocity boundary condition at the liquid/solid interface and the numerical procedure of the free surface in the neighborhood of the contact line (see Figure 7.1). Let us denote the time required from the moment of collision of a droplet with the surface up to the formation of a vapor film between the liquid drop and the surface by t_c.

In the time range of $t < t_c$, the no-slip condition was adopted ($u = v = 0$ at the wall) and the pressure condition at the liquid/solid interface is given by:

$$p' = p_{1/2} - \frac{1}{2}v_1|v_1| + \frac{\Delta y}{Fr^2} - \frac{2v_1}{Re\cdot\Delta y} \tag{7.13}$$

in which p' and $p_{1/2}$ denote the pressure at the external and the interior cells contacting the wall respectively and v_1 is the velocity component normal to the wall. Δy is the mesh size in the y-direction. The curvature required to estimate the surface pressure in the neighborhood of the contact line is calculated using the one-sided difference approximation, because it is impossible to apply the central difference approximation to the calculation of the free surface curvature, as shown in Figure 7.1(a).

In the time range of $t \geq t_c$, the free-slip condition ($v = 0, u' = u$; u'=velocity component at the external cell of the solid wall) is adopted at the liquid/solid interface, because there is no friction owing to the formation of a vapor film. In addition, the pressure on the solid surface is given by

$$p' = p_{1/2} + \frac{\Delta y}{Fr^2} \tag{7.14}$$

a) $t < t_C$

free surface line

○ surface point

fluid side

No slip condition (u=v=0)

Solid surface

b) $t \geq t_C$

free surface line

fluid side

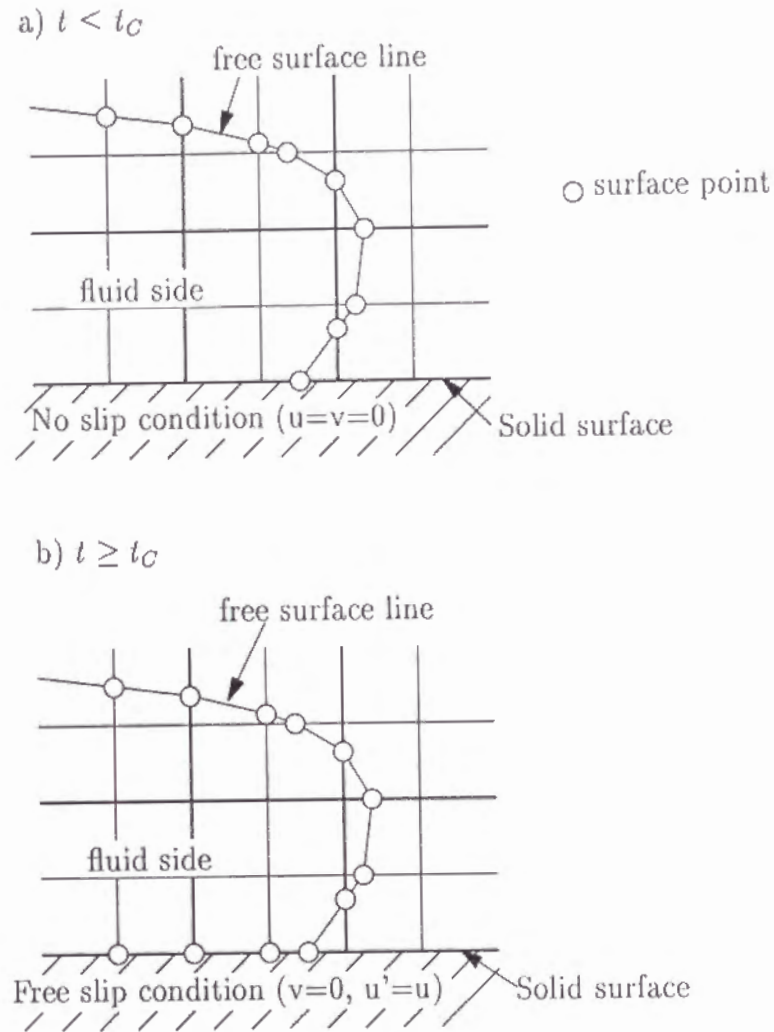Free slip condition (v=0, u'=u)

Solid surface

Figure 7.1: Indication of boundary conditions for droplet contacting solid surface(a) and for droplet being separated from surface by a vapor film(b)

on the free slip condition. Furthermore, it may be justifiable to assume that the liquid drop is insulated with the hot solid surface through a thin vapor film and that the diameter of the circular area contacting the vapor film is always smaller than the maximum diameter of the liquid film/drop. Therefore, the free surface near the periphery of the area contacting the vapor film can be regarded as the region with a very large curvature. By so doing, the principal radii of curvature near the periphery of the liquid film are calculated by setting the mesh points representing the free surface at the vapor/solid interface (see Figure 7.1(a)). The calculation is performed by not the one-sided, but the central difference approximation. Thereby, the peripheral zone with a large curvature plays an important role of the driving force to make the liquid drop rebound from the surface.

Here, the assumptions that the droplet reaches the saturation temperature at the moment of impact and the droplet volume remains unchangeable are introduced into the present numerical simulation. The calculation starts at the moment of impact of a droplet with a hot surface ($t=0$). The mesh size is selected to be $\Delta x (= \Delta y)=1/100$ according to the previous chapter. Also, the computational time interval Δt is determined by the CFL (Courant-Friedrichs-Lewy) condition and CFL number f is set at $f=0.05$ according to the previous chapter.

7.4 Experimental apparatus

Figure 7.2 shows a schematic diagram of the experimental apparatus by which the deformation process of a droplet impinging on a heated rigid surface beyond the Leidenfrost temperature can be measured. The water stored in a gastight tank is introduced to a needle and the droplet is formed through the needle. The water is pressurized statically by a high pressure air to ensure repeatability of droplet formation and release at the needle tip. The needle is flat tipped and set vertically. A needle oscillator using speaker coil, which vibrates at a particular frequency, is attached to the needle tip. Thereby, a uniformly spaced stream of droplets is generated with an almost equal diameter and velocity at the needle tip. Also, the adjustment of the spacing of droplets can be made in accordance with the vibration frequency of a needle oscillator. A disk of 200 mm in diameter rotates horizontally between the needle exit and the heated surface. Only one droplet per revolution can pass through the slit hole of the rotating disk and reach the horizontal heated surface. The droplet size as well as the impinging velocity is easily changeable by the water pressure, the vibration frequency of the needle oscillator and the inner diameter of the needle. But, it is impossible to change only the droplet diameter on the condition of keeping the impinging velocity constant and the inverse is also impossible. By this experimental apparatus, droplets of 300 μm to 700 μm can be generated in the impinging velocity range between 1.2 m/s and 6.0 m/s.

The droplet falls vertically onto a 6 mm thick by 28 mm diameter Inconel alloy 625 test surface. The test surface temperature is measured by the chromel-alumel thermocouples and adjusted by the thermocontroller unit (Omron, E5A2). Throughout the present chapter, the surface temperature is fixed at 500 °C. But, it should be noted that the temperature change during the experiments is confirmed to be within $\pm 20°C$. The deformation process of a droplet is recorded by using a video camera which is equipped with a macro lens. The droplet images are exposed by the back light method using two micro flash units (Sugawara MP230), which can be operated at a constant time interval. The first flash is adjusted to catch the droplet just before the collision with the surface. The flash timing is met by using both an optical sensor perceiving the slit position on the disk and a delay timer. In the present experiments, the droplet is photographed in the range of the time interval from 100 μs to 1600 μs. The time interval of the two flash units can be set by a flash controller. The lightening period of the flash units is kept below 2 μs. The droplet image can be exposed only during flashing.

The time variation of the droplet height and radius during the deformation is recorded by many double exposure video images on the basis of the statistical procedure. The droplet diameter before reaching the heated surface can be directly measured from the video image. Also, the impinging velocity can easily be estimated from both the moving

air
Pressure valve
Air tank
Water tank
Needle tip
Slit hole
Signal generator
Amplifier
φ 200
Needle oscillator
(Speaker coil)
Optical sensor
Motor
Delay timer
Rotating disk
Flash controller
Thermocouples
Flash units
Test piece
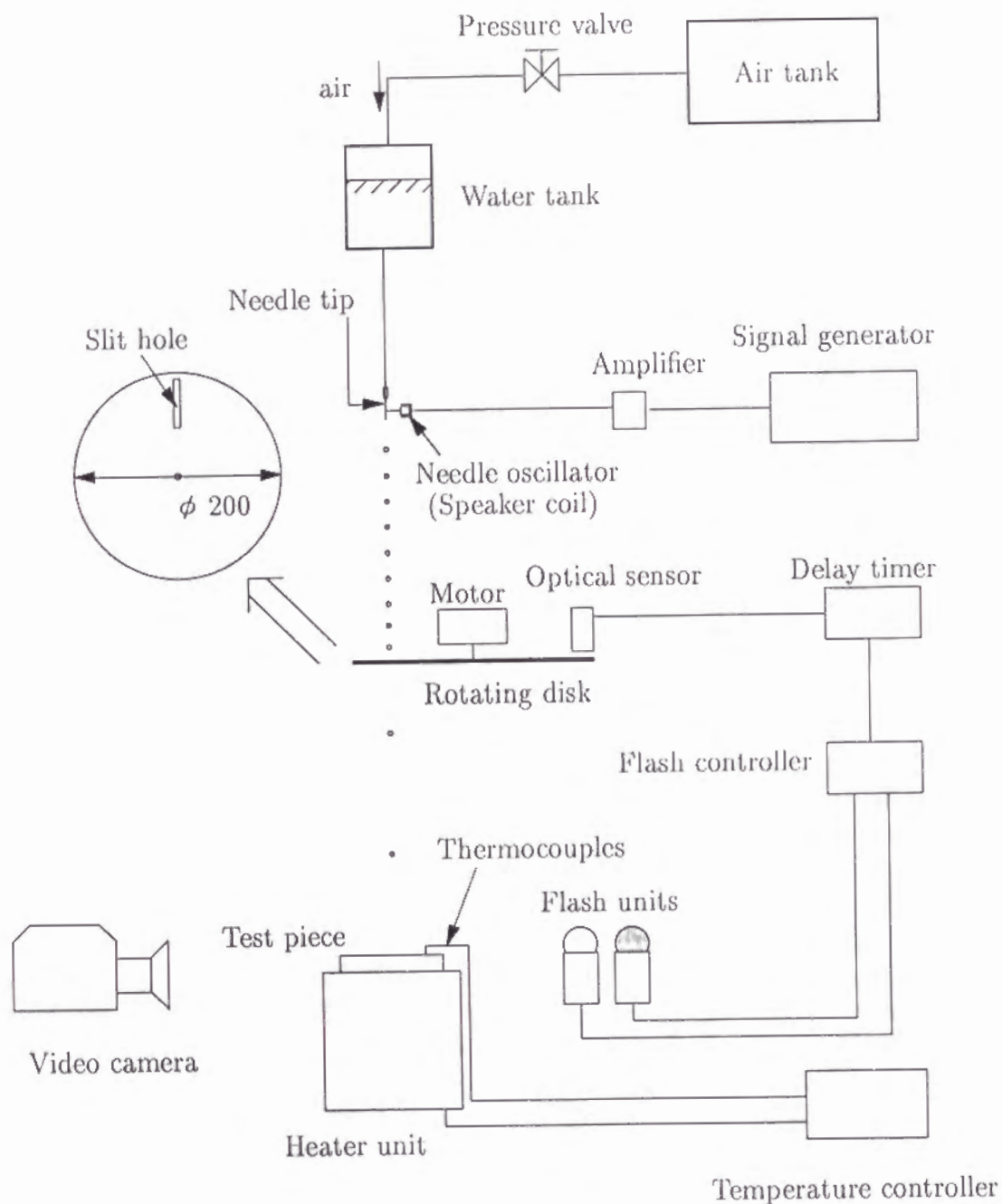Video camera
Heater unit
Temperature controller

Figure 7.2: Experimental apparatus

distance of the droplet and the time interval of the two flashes. When the impinging velocity is measured, the both images of the same droplet photographed by the first and second flashes are required to be before the collision with the surface, and the time interval of two flashes is assigned below 200 μs.

The residence time of the droplet during the deformation on the hot surface after making contact with it can be evaluated from the distance between the droplet and the surface in the first exposed image, the impinging velocity and the time interval of two flashes. Thereby, the height and the radius of the droplet on the surface can be measured directly from the second exposed image. The droplet deformation process is pursued by a lot of droplet images. Again, the measurement accuracy determined by the resolution of the video image is within ± 6 μm in the present measurement unit.

7.5 Results and discussion

It is well-known that on lower We numbers condition a droplet strikes and spreads and eventually rebounds as a bowling pin-shaped mass from a hot surface, while for a high We number the droplet shatters during the deformation process [3,4]. The critical Weber number We_c, which specifies the boundary between rebounding and disintegrating, was proposed by some researchers. Ueda et al. [4] gave $We_c=70$ on the basis of the empirical results obtained on condition that the droplets of 1 mm to 3 mm in diameter fell on the flat stainless steel and copper surface heated to 300°C. Again, Shoji et al.,[10] proposed $We_c = 80 \sim 90$ on condition that the droplets of 0.3 mm to 3.5 mm impinged on the flat nickel surface heated in the temperature range from 300 °C to 800 °C. Hence, we also investigated the deformation and rebounding phenomena of the droplet after making contact with an Inconel 625 alloy surface heated to 500 °C under the experimental condition that the droplet size $\bar{D}_p = 330 \mu m$ to $600 \mu m$ in diameter and the impact velocity $\bar{u}_0 = 1.7$ m/s to 5.7 m/s. As a result, $We_c \simeq 50$ was obtained in Chapter 5 and this value was found to be relatively small in comparison with the above mentioned two results. We consider that the rebounding condition is influenced not only by the We number, but also by other parameters such as the surface temperature, the surface roughness, the affinity at the liquid/solid interface, etc.. Then, the water droplets of $We \leq 50$ are treated in the present investigation.

First, in order to identify the time t_c required from the moment of impact up to the formation of a vapor film, we inspected numerically the effect of t_c on the deformation behavior using various values of t_c. Figure 7.3 gives the time evolution of the height h and radius r of the droplet on condition that $\bar{D}_p = 0.44$ [mm] and $\bar{u}_0 = 2.00$ [m/s] (Re=2960 and We=28.7). We note that h and r are normalized by the initial droplet diameter; $h \equiv \bar{h}(\bar{t})/\bar{D}_p$ and $r \equiv \bar{r}(\bar{t})/\bar{D}_p$ (see Figure 7.4). The solid and empty circles in Figure 7.3 denote the experimental data of h and r, respectively. In the present calculation, three cases are considered where $t_c=0$, 1.0 and 1.2. $t_c = 0$ corresponds to the case where h and r are calculated on the free-slip condition from the start ($t=0$). Comparing the three kinds of calculated results with each other, the three calculated time histories agree well with each other in the spreading process ($t < 1.2$) and no significant difference among them can be found also in the recoiling process. Although one can image that the spreading
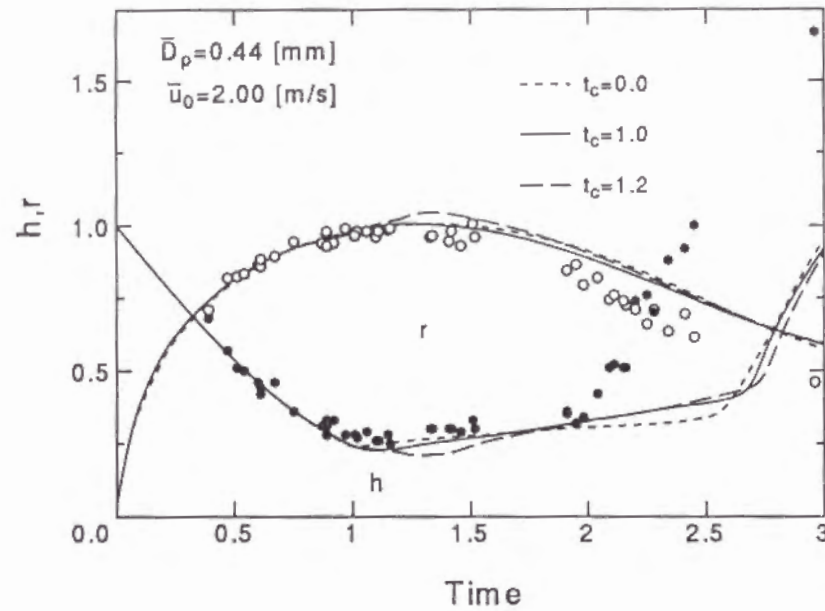
Figure 7.3: Time evolution of the droplet hight h and radius r on condition that $\bar{D}_p = 0.44$ [mm] and $\bar{u}_0 = 2.00$ [m/s] (Re=2960 and We=28.7) for various t_c. Note that the experimental uncertainties in both the droplet radius r and height h are kept within ± 0.023 on a nondimensional scale.

rate calculated on $t_c = 0$ is larger than that of other cases where the no-slip condition is introduced, these are the facts of the case. Let us consider the process. First, the adoption of the free-slip condition corresponds to the case where the liquid drop is isolated with the solid surface through a vapor film. Namely, the bottom side of the liquid drop can be treated as a part of free surface. Therefore, the curvature can be regarded as being very large at the periphery of the liquid drop and the inner pressure rises there. As a result, the spreading rate is considered to be constricted even for the case where $t_c = 0$.

Next, comparing the calculated results with the experimental data, the two are seen to be in good agreement with each other in the spreading process ($t < 1.2$). However, the difference between the two widens in the recoiling process. The recoiling rate calculated by the present numerical model is appreciably slower than the experimental. We find that the experimental height h abruptly grows at $t \simeq 1.9$, but a similar process occurs in the numerical simulation after an appreciable time elapsed. The difference between the calculated and experimental results may be due to the fact that the effect of phase transition from liquid to vapor is neglected in the numerical model.

As mentioned above, no significant difference in the historical curves of h and r could be found regardless of the value of t_c. There is little to choose among them, but $t_c = 1$ is, if anything, a shade better. Therefore, this value is adopted in the later numerical experiments.
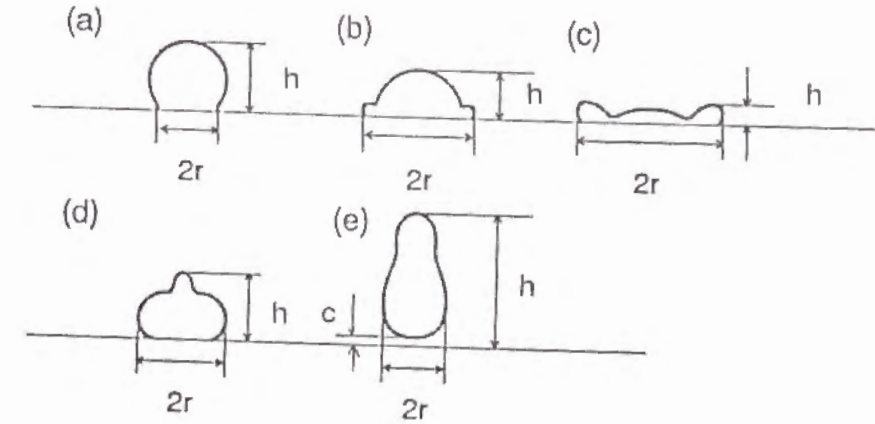

Figure 7.4: Definition of droplet height h, radius r and distance between droplet and plate surface c.

Figure 7.5 gives the comparison between the calculated and experimental time histories of h and r on condition that $\bar{D}_p = 0.60$ [mm] and $\bar{u}_0 = 1.72$ [m/s] (Re=3470 and We=28.9). The calculated results give a good agreement with the experimental in the spreading process, as shown in the previous case. But, an abruptly increasing point of h in the numerical simulation is seen to be later than that in the experiment.

Figure 7.6(a) indicates the comparison between the calculated and experimental time evolutions for the droplet height h, the radius r and the distance c from the solid surface to the bottom of droplet after the rebounding on condition that $\bar{D}_p = 0.38$ [mm] and $\bar{u}_o = 2.05$ [m/s] (Re=2620 and We=26.0). The abruptly increasing point of h obtained by the numerical model is also seen to be delayed in comparison with the experimental. The period when $c = 0$ corresponds to the residence time of the droplet on the surface, because the distance c can be measured just after the rebounding of droplet from the surface (see Figure 7.4). The calculated residence time also is longer than the experimental.

Comparing the calculated time evolutions with the experimental ones, shown in Figures 7.3, 7.5 and 7.6, a good agreement between the calculated and experimental results was obtained in the spreading process, but an appreciable difference was found between the two in the retracting process. Considering all the above-mentioned results, particularly, the calculated value of the time at which the height h begins to increase is later by $0.7 \sim 1.0$ on the non-dimensional time scale than the experimental value. However, we believe that the calculated results give, at least, a qualitative agreement with the measured ones, except the delay of an abruptly increasing point of h is seen to occur.

Figure 7.6(b) gives the time evolutions of the velocity vector and pressure fields obtained by the present numerical model on the same condition as in Figure 7.6(a). It is noted that the pressure contours in the left side of each figure are plotted by $p = p_\infty \pm 0.1k$ ($k = 1, 2, \cdots$) and the length of arrows showing the magnitude of the velocity vector is not comparable at every time stage. It is observed from this figure that the droplet impinging on a hot surface spreads in the shape of a flattened disc in the time range of $t < 1.2$. The edge part of the radially spreading liquid film is observed to be roundish owing to the surface tension effect. Therefore, the inner pressure in the roundish edge part is higher than the atmospheric pressure and the edge part expands with time. The spreading liquid
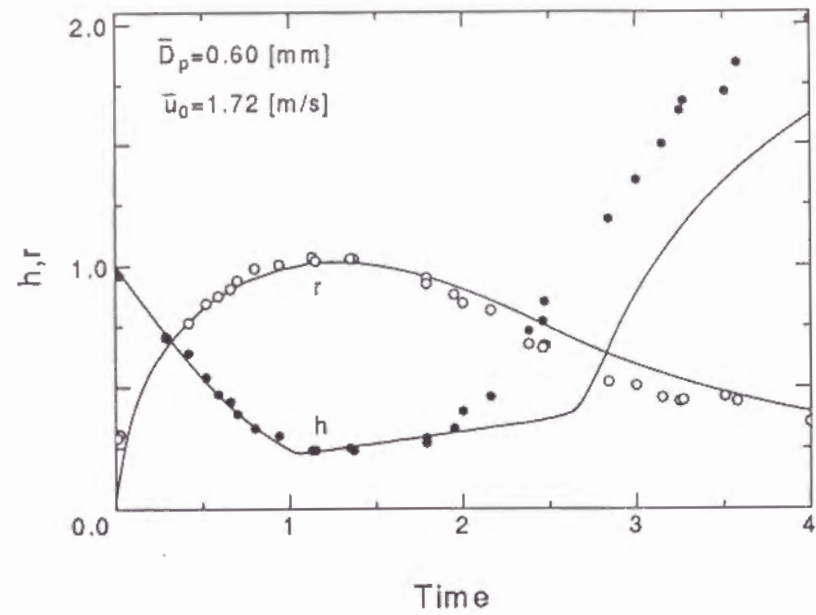
Figure 7.5: The comparison of the numerical droplet hight h and radius r with experimental values on condition that $\bar{D}_p = 0.60$ [mm] and $\bar{u}_0 = 1.72$ [m/s] (Re=3470 and We=28.9). Note that the experimental uncertainties in both the droplet radius r and height h are kept within ± 0.018 on a nondimensional scale.

film may be divided into two regions. One of which is the part of the convex lens-like shape located in the central region. The other is the part of the doughnut-like shape in the peripheral region. There can be seen a trough between the above mentioned two parts. The free surface of the trough is sharply concave and its inner pressure must be remarkably lower than the atmospheric pressure. After the liquid film diameter reaches a maximum value at $t \simeq 1.2$, the high pressure liquid at the periphery begins to flow backwards towards the trough whose inner pressure is relatively low. At the same time, the liquid in the central region continues to flow outwardly toward the trough with an appreciably low speed. As a result, the flow backwards from the peripheral region comes into collision with another flow from the center, at the concave region. Finally, the collision of the flows keeps the position of the trough moving towards the center and thereby the roundish edge zone grows in both thickness and width. This may be due to the fact that the flow induced by the surface tension effect is superior to the flow from the center. At $t \simeq 2.4$ the concavity is seen at the center. Subsequently, the liquid flowing from the periphery is concentrated at the center and the rising flow is formed there at $t \simeq 2.8$. The top part of the liquid pulls upwardly the lower part and then the liquid droplet is elongated longitudiually at $t \simeq 2.8 \sim 4.0$. As a result, both the upward velocity component and pressure of the top part of the liquid decrease with time. Figures 7.7(a) and 7.7(b) indicate the time evolutions for the velocity and pressure distributions along the central axis (y-axis) with time as a parameter, on the same condition as in Figure 7.6(a).

Next, as the flat surface of the bottom part of liquid droplet near the solid surface is reduced, a ring vortical structure is formed at the bottom of the elongated droplet and induces the rotative motion there in such a way as to form the rising flow. Finally, the
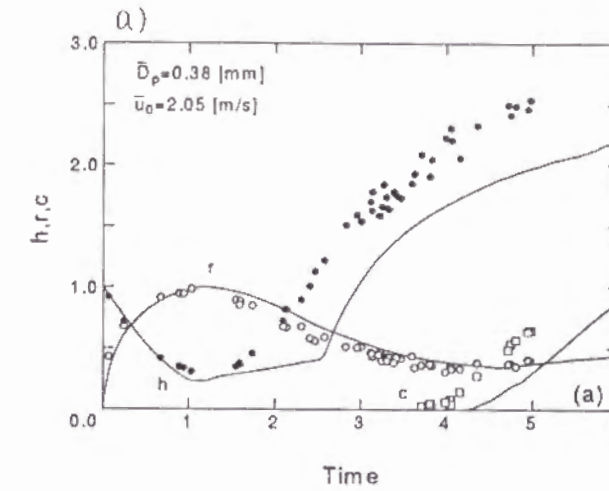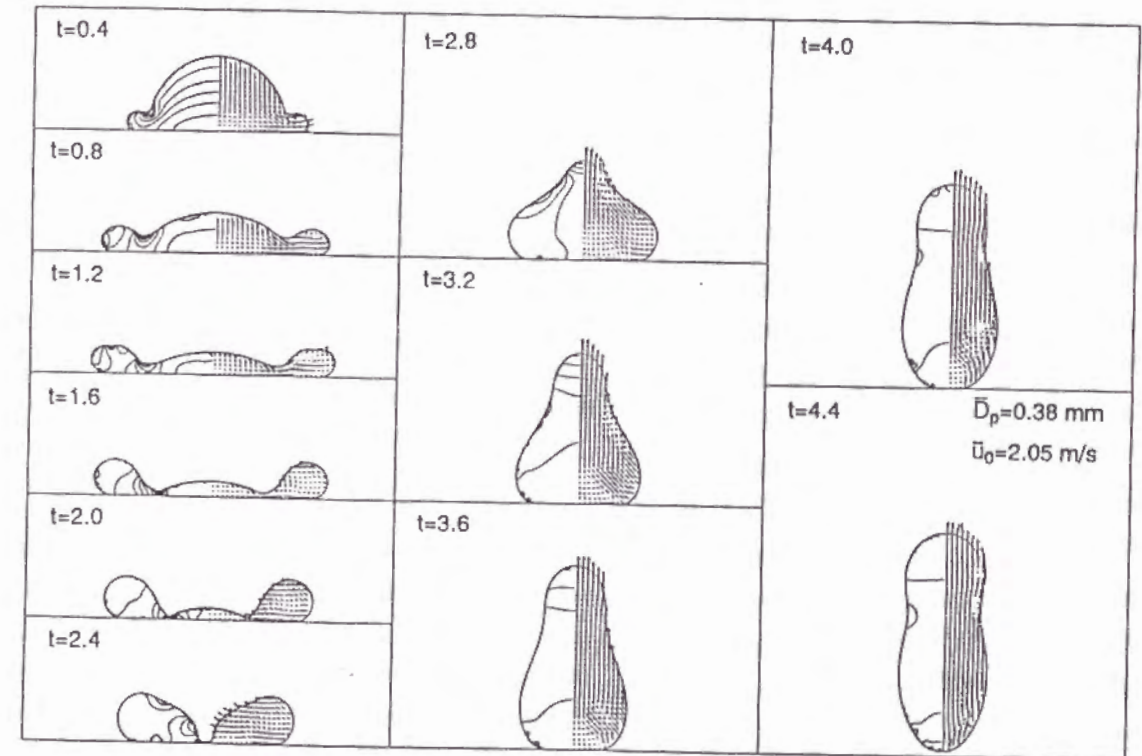

Figure 7.6: Comparison of numerical time histories of droplet height h, radius r and the distance between the droplet and a plate c with experimental values (a) and time history of numerical velocity vector fields and pressure contours of droplet (b) for $\bar{D}_p = 0.38$ [mm] and $\bar{u}_0 = 2.05$ [m/s] (Re=2620 and We=26.0). Note that the experimental uncertainties in r,h and c are kept ± 0.026 on nondimensional scale.
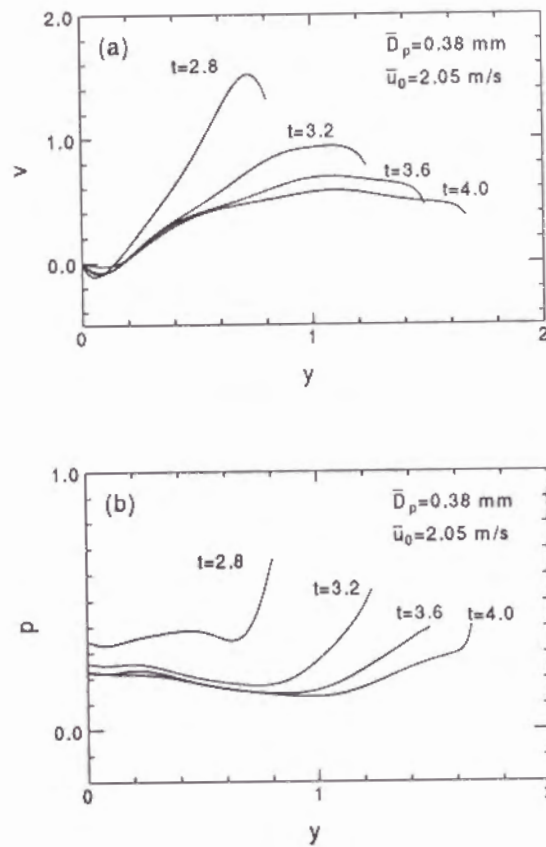
Figure 7.7: Time evolutions for velocity (a) and pressure (b) distributions along the central axis with time as a parameter on the same condition as shown in Figure 7.6.

droplet rebounds as a bowling pin-shaped mass from the surface at $t \simeq 4.4$. Details of the formation process of the vortical structure are shown in Figure 7.8.

As mentioned above, it has been clarified that the rebounding phenomena occur with the surface tension effect as the driving force and the present numerical model is capable of simulating the whole process of spreading, retracting on the hot surface and rebounding from it.

Photo. 7.1 shows the deformation and rebounding behavior on the same condition as in Figure 7.6(a). As mentioned already, the time variation of the droplet height and radius during the deformation was recorded by a number of double exposure video images on the basis of the statistical procedure. All the photographs shown here were obtained by double exposure video images. Namely, the spherical droplet before reaching the heated surface was photographed at the first flash and the configuration during the deformation after impact on the surface was reflected at the second flash. It is noted that the time interval of two flashes is not common at each picture. The time in every photograph corresponds to the time elapsed after impact at which each picture was taken at the second flash. Comparing the calculated droplet configuration with the experimental, there can be seen a correspondence between the two even in the retracting process, although a time lag appears. The calculated droplet configurations at $t = 3.2$ and $t = 3.6$ give good fit to the photographic ones at $t = 2.3$ and $t = 3.0$, respectively.

Akao et al. [5] inspected the rebounding phenomena of the liquid droplet for the case where a droplet of 0.2cm to 0.3 cm in diameter impinges on a copper surface heated to 400 °C. Also, they photographed the deformation behavior of an impinging droplet on the experimental condition that $\bar{D}_p = 2.9$[mm] and $\bar{u}_0 = 0.86$ [m/s] (Re=8397 and We=35.0). Figure 7.9 indicates the velocity vector and pressure fields calculated by the present numerical model on the same condition as shown above. Comparing the calculated droplet configurations with the ones photographed by them, a good correspondence can be found between the two. But, a time lag also appears in the present simulation. In the experiment made by them, the droplet rebounds at approximately 14.7 ms after making contact with the surface, while the rebounding occurs approximately at 17.5 ms in the calculation.

Furthermore, comparing this numerical result with the one shown in Figure 7.6(b), the droplet configuration on the rebounding shows a tendency to be elongated longitudinally with the increase in We. In fact, the droplet configuration on the rebounding shown in Figure 7.9 is seen to be longer than that in Figure 7.6(b). Also, the neck of the bowling pin-like shaped drop in Figure 7.9 is narrow and located in the remarkably upper position, in comparison with the case shown in Figure 7.6(b). This may be due to the fact that the magnitude of the upward velocity component near the central axis is maintained by the momentum of the liquid flowing from the periphery towards the center, when We is increased. Again, according to Wachters & Westerling [3], it is reported that the droplet reflected from the surface is disintegrated into two drops at the neck in air on the condition of $We > 30$. The disintegration does not occur in the present simulation. But, we can easily image that the neck becomes narrower and then the droplet is disintegrated into two drops as We is enlarged further.
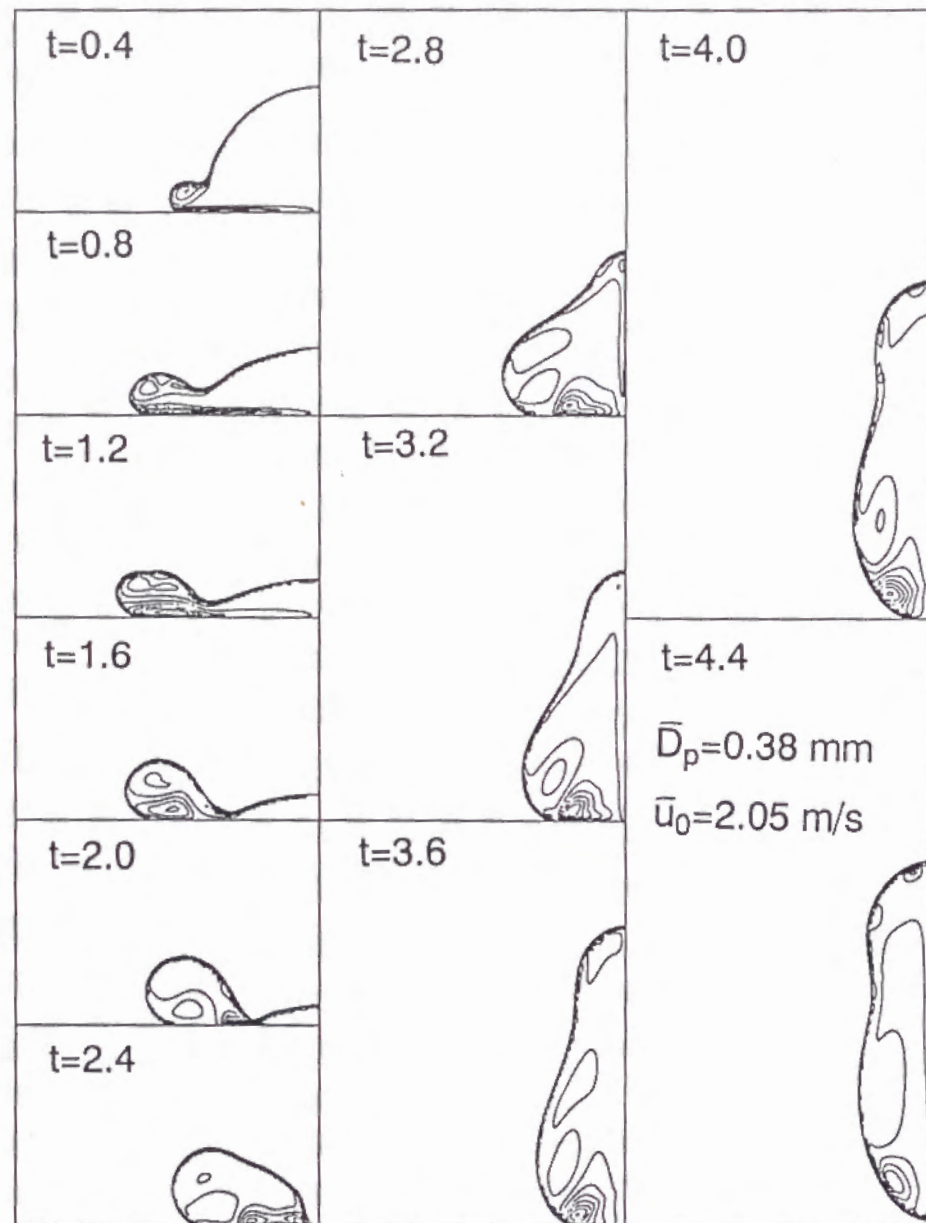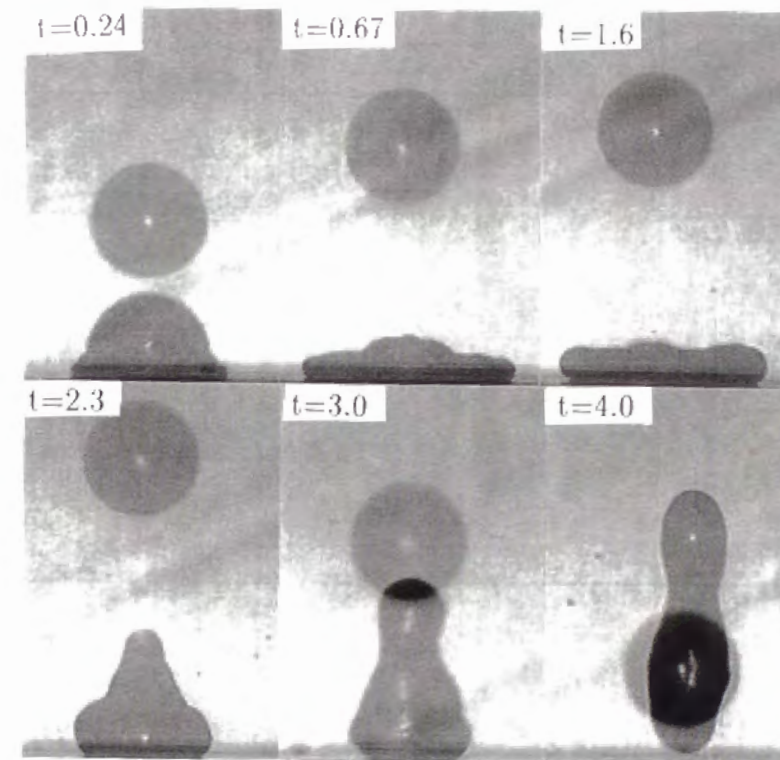
Figure 7.8: Time history of vorticity contour on the same condition as shown in Figure 7.6.

Photograph 7.1: Deformation process of droplet impinging on a flat plate with $\bar{D}_p=0.38\pm0.01$ [mm] and $\bar{u}_0=2.05\pm0.01$ [m/s].
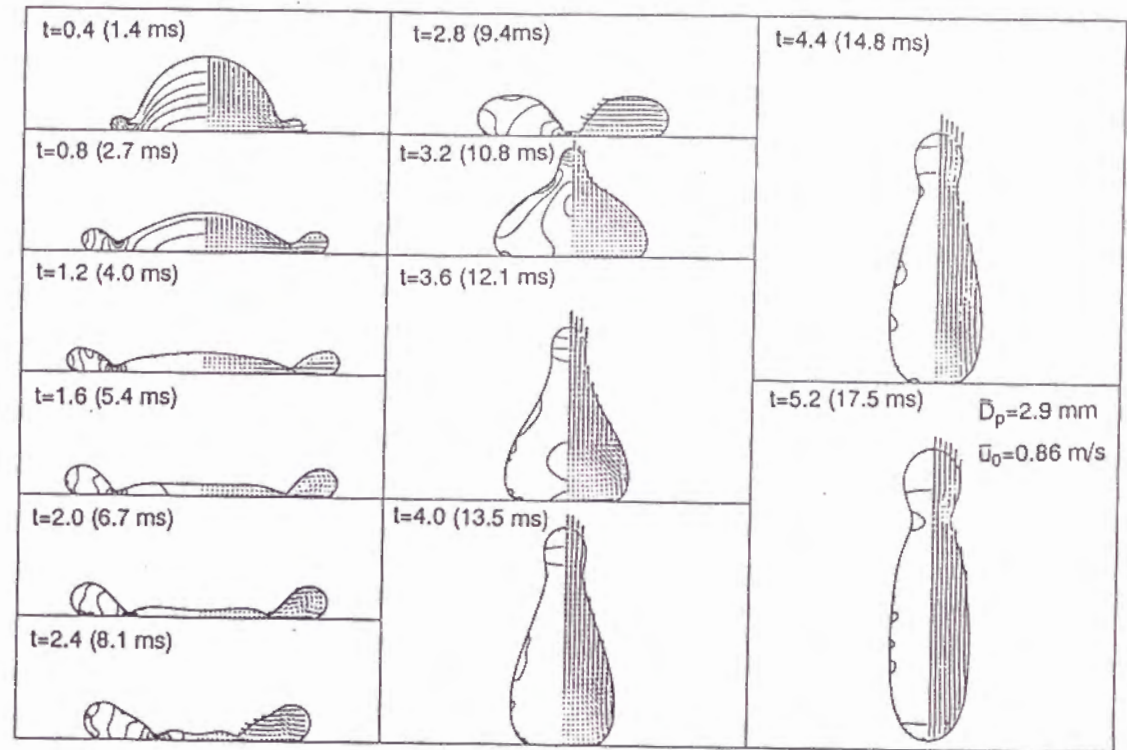
Figure 7.9: Numerical free surface configuration and velocity vector field of a droplet impinging on a flat plate and pressure distribution along the surface with $\bar{D}_p = 2.9$ [mm] and $\bar{u}_0 = 0.86$ [m/s] (Re=8397 and We=35.0).

7.6　Conclusion

The collision dynamics of a water droplet impinging on a flat surface above the Leidenfrost temperature, have been investigated from numerical and experimental points of view. Emphasis was placed upon the analysis of the deformation and rebounding processes of a droplet after the collision with the surface. The effect of viscous stresses and surface tension have been taken into consideration and a numerical model capable of predicting the deformation process has been built up. The results obtained by the model have been compared with the experimental data.

The droplet impinging on the hot surface spreads in the shape of a flattened disk during the early stage of impact. In a very short time after impact the liquid drop is completely separated from the solid surface by a vapor layer. The free surface near the periphery of the area contacting the vapor film can be regarded as the region with a very large curvature. Therefore, the inner pressure there is considered to much higher than the atmospheric pressure and the edge part expands with time. The spreading liquid film can basically be divided into the following two parts. One is the convex-lens shaped part located in the central region. The other is the doughnut-like shaped part in the peripheral region. A trough whose configuration is sharply concave exists between the above two parts and inner pressure in the concave zone must be appreciably lower than the atmospheric one. As a result, the flow backwards from the peripheral region comes into collision with another flow from the center at the concave region. The collision of the flows keeps the position of the trough moving toward the center and then the concavity is formed at the center. Subsequently, the liquid is concentrated at the center and begins to elongate upwards. Finally, a ring vortical structure appearing at the bottom of the elongated droplet induces the rotative motion in such a way as to form the rising flow and the droplet rebounds from the surface.

The numerical results obtained by the present numerical model can well explain both the deformation process of droplet on the surface after impact and the rebounding process from it. However, the calculated value of the time required from the moment of impact to the rebounding has been found to be a little long in comparison with the experimental value.

Finally, we believe that the present investigation represents a contribution to the physical understanding of the dynamics of free surface bodies.

Reference

1. Hatta, N., Ishii, R. and Fujimoto, H., Trans. ASME J. Fluids Engg., 114(1992), p.420.

2. Hatta, N., Fujimoto, H. and Takuda, H., Applied Scientific Research, 50(1993), p.129.

3. Wachters, L. H. J. and Westerling, N. A., Chem. Engg. Sci., 21(1966) .p.1047.

4. Ueda, T., Enomoto, T. and Kanetsuki, M., Bull. of the JSME, 22(1979), p.724.

5. Akao, F., Araki, K., Mori, S. and Moriyama, A., Trans. ISIJ, 20(1980),p.737.

6. Chandra, S. and Avedisian, C. T., Proc. of the Royal Society Lond. A, 432(1991), p.13.

7. Xiong, T. Y. and Yuen, M. C., Int. J. of Heat and Mass Transfer, 34(1991), p.1881.

8. Hatta, N., Fujimoto, H. and Takuda, H., To be published in Trans. ASME Journal of Fluids Engineering(1994).

9. Miyata, H., J. Comput. Phys., 65(1986), p.179.

10. Shoji, M., Wakunaga, T. and Kodama, K., JEME-B, 50(1984), p.716.

11. Fujimoto, H. and Hatta, N., To be submitted in Trans. ASME J. Fluids Engg.

Chapter 8

Concluding remarks

In this thesis, first, the flow field of gas-water droplet two-phase mixtures in a nozzle, accounting for a continuous distribution of particle size, has been investigated from a numerical point of view. Next, the numerical simulation of gas-particle two-phase free jets exhausted from a round nozzle has been performed as a perturbation from the results of nozzle flow. Moreover, the flow field of gas-droplet two-phase mixture jets impinging on a flat solid surface normal to the flow, corresponding to the mist/spray cooling situation, has been solved numerically on assumption that the droplets are perfectly elastically reflected from the surface. However, it seems to be doubtful whether or otherwise the reflection condition gives fit to the realistic phenomenon. In this regard, in order to clarify the particle behavior of the during and subsequent to the collision with the hot surface above the Leidenfrost temperature, the deformation and rebounding processes of impacting droplet on the hot surface have been investigated experimentally by using a video camera recorder with a macro lens. Also, because it is almost impossible to measure the inner flow field of a droplet during and subsequent to the collision, the analysis on the flow field inside the droplet has been performed by numerical simulations. That is to say, the deformation process of the droplet impinging on the solid surface at room temperature has been analysed taking into account the viscous stresses and surface tension effects. Subsequently, the deformation and rebounding processes of the droplet on a hot surface above the Leidenfrost temperature have been treated from a practical point of view. The results obtained in this thesis are summarized as follows.

The analytical procedure to simulate the flow field of gas-particle two-phase mixtures in a nozzle has been established for both the specified area method and the specified pressure method. The nozzle flows of gas-particle two-phase mixtures have been calculated by the specified area method according to a given nozzle geometry with a parallel region. Then, it has been found that the flow properties exhibit a tendency to change even in a parallel region for two-phase mixture flows, while for a gas-only flow, the flow properties do not vary in this region. Also, it has been demonstrated that the nozzle configuration can be designed according to a given pressure profile along the nozzle axis by using the specified pressure method.

The mathematical model, accounting for thermal coupling through heat transfer from gas-phase to particle-phase as well as momentum coupling through aerodynamic drag

responsible for particle motion, has been constructed to analyse the gas-particle two-phase free jets. It has been found from numerical simulations that, regardless of whether it is single phase or two-phase flow, the vortical structures occurring at the jet boundary of the nozzle exit are convected downstream along the boundary, and that perfectly steady solution can not be reached even at $t \to \infty$. The particle behavior in a gas flow is explicitly characterized by the Stokes number defined as the ratio of the aerodynamic response time to the characteristic time of the flow field. The case has been tested where the Stokes number γ_τ is 0.08, 2.0 and 75, respectively. The flow structure of two-phase mixtures for $\gamma_\tau \ll 1$ is approximately in velocity and thermal equilibrium state. For $\gamma_\tau \gg 1$, the particles will not have sufficient time to respond the gas flow and will move in nearly rectilinear path. Again, the experiment has been done to verify the results obtained by the present numerical model. The numerical results have been found to give agreement with the experimental data quantitatively.

The flow fields of gas-particle two-phase jets impinging on a flat plate exhausted from a round nozzle have been calculated for the case where the Stokes number γ_τ is 0.34, 8.7 and 35.6, respectively. For $\gamma_\tau < 1$, the particles travel very closely to the surface along the radial direction after the impingement of two-phase jet on the surface, while for $\gamma_\tau \gg 1$, the greater part of reflected particles are dispersed from the surface in the stagnant ambient region outside the core flow owing to larger velocity component normal to the plate surface. Also, the usage of a low-velocity annular gas-only flow which surrounds a round nozzle co-axially has been considered to push back particles in the stagnant region to the surface again from a viewpoint of the improvement of the cooling effect. As a result, it has been found to be roughly possible to put together the particles to the surface again.

The criterion whether a droplet breaks up on a hot surface after impact or rebounds from the surface has been tested on the experimental condition that the particle diameter ranges from 300 μm to 600μm and the surface temperature is fixed at 500 °C. It has been found that the critical Weber number is approximately 50. The effects of the We number and the Re number on the maximum spreading diameter of the droplet on the surface have been examined. Then, no significant effect of the Re number could be found and the empirical formula capable of predicting the spreading diameter has been proposed as a function of the We number only. Also, the experimental formula capable of evaluating the coefficient of restitution of droplets has been presented as a function of the We number.

The analytical model, accounting for the effects of viscous stresses and surface tension, has been constructed to estimate the deformation process of a droplet impinging on a solid surface at room temperature. The numerical results of deformation process of the water droplet have been found to be in good agreement with experimental values in an early period. On the other hand, for the case of a n-heptane droplet, the numerical results obtained with no surface tension effect have been confirmed to be fairly in agreement with experimental data. It may be concluded that the deformation process of a liquid droplet on a surface can be determined not only by the We number and the Re number, but also by the other parameters such as the initial kinetic energy of a droplet, the affinity at the solid/liquid interface etc..

Finally, the numerical model capable of predicting the deformation and rebounding processes of a water droplet impinging on the hot surface above the Leidenfrost temperature has been built up. The numerical results can well explain both the deformation process of the droplet on the surface after impact and the rebounding process from the surface, although the calculated value of the time required from the moment of impact to the rebounding from the surface has been found to be a little long in comparison with the experimental value.

The final purpose of this study is to estimate quantitatively the heat transfer between the mist/spray flow and the heated surface. The approach needs essentially to be performed from the points of hydrodynamics as well as heat transfer. The investigations in this thesis have been prompted from a hydrodynamical point of view, focusing upon the flow field of mist/spray in a nozzle and in a free jet region, and upon the deformation or/and the rebounding process of impacting droplet on a surface. In this regard, the author believes that the desired end has been reached.

Hereafter, the author wishes to continue this study from the point of view of heat transfer between the mist/spray flow and the hot surface. However, a few difficult problems must be solved. For example, the effects of the phase transition of a droplet from liquid phase to vapor phase and droplet-droplet interaction near the hot surface on the thermal field need quantitatively to be estimated and introduced to the analytical procedure. Also, the effect of the physical properties of cooled surface, such as the surface roughness and the thickness of oxide layer, on the cooling process must be estimated quantitatively. The author intends to challenge such complicated problems.

Acknowledgement